Theses and Dissertations

12-2018

Morphological Features of Dysplastic Progression in Epithelium: Quantification of Cytological, Microendoscopic, and Second Harmonic Generation Images

Sandra Patricia Gordon
University of Arkansas, Fayetteville

Morphological Features of Dysplastic Progression in Epithelium: Quantification of Cytological, Microendoscopic, and Second Harmonic Generation Images

A dissertation submitted in partial fulfillment
of the requirements for the degree of
Doctor of Philosophy in Engineering with a concentration in Biomedical Engineering

by

Sandra Patricia Gordon
Andrews University
Bachelor of Science in Engineering with an Emphasis in Electrical and Computer Science, 2011

December 2018
University of Arkansas

This dissertation is approved for recommendation to the Graduate Council.

_____
Timothy J. Muldoon, M.D., Ph.D.
Dissertation Director

_____   _____
Kyle P. Quinn, Ph.D.   Yuchun Du, Ph.D.
Committee Member   Committee Member

_____
David A. Zaharoff, Ph.D.
Committee Member

Abstract

Advances in imaging technology have led to a variety of available clinical and investigational systems. In this collection of studies, we tested the relevance of morphological image feature quantification on several imaging systems and epithelial tissues. Quantification carries the benefit of creating numerical baselines and thresholds of healthy and abnormal tissues, to potentially aid clinicians in determining a diagnosis, as well as providing researchers with standardized, unbiased results for future dissemination and comparison.

Morphological image features in proflavine stained oral cells were compared qualitatively to traditional Giemsa stained cells, and then we quantified the nuclear to cytoplasm ratio. We determined that quantification of proflavine stained cells matched our hypothesis, as the nuclei in oral carcinoma cells were significantly larger than healthy oral cells.

Proflavine has been used in conjunction with translational fluorescence microendoscopy of the gastrointestinal tract, and we demonstrated the ability of our custom algorithm to accurately (up to 85% sensitivity) extract colorectal crypt area and circularity data, which could minimize the burden of training on clinicians. In addition, we proposed fluorescein as an alternative fluorescent dye, providing comparable crypt area and circularity information.

In order to investigate the morphological changes of crypts via the supporting collagen structures, we adapted our quantification algorithm to analyze crypt area, circularity, and an additional shape parameter in second harmonic generation images of label-free freshly resected murine epithelium. Murine models of colorectal cancer (CRC) were imaged at early and late stages of tumor progression, and we noted significant differences between the Control groups and the late cancer stages, with some differences between early and late stages of CRC progression.

Table of Contents

List of Published Papers

S. P. Prieto, A. J. Powless, J. W. Boice, S. G. Sharma and T. J. Muldoon, "Proflavine Hemisulfate as a Fluorescent Contrast Agent for Point-of-Care Cytology," *PloS One*, vol. 10, *(5)*, pp. e0125598, 2015.

ChS. P. Prieto, K. K. Lai, J. A. Laryea, J. S. Mizell and T. J. Muldoon, "Quantitative analysis of ex vivo colorectal epithelium using an automated feature extraction algorithm for microendoscopy image data," *Journal of Medical Imaging*, vol. 3, *(2)*, pp. 024502, 2016.

S. P. Prieto, K. K. Lai, J. A. Laryea, J. S. Mizell, W. C. Mustain and T. J. Muldoon, "Fluorescein as a topical fluorescent contrast agent for quantitative microendoscopic inspection of colorectal epithelium," *Biomedical Optics Express*, vol. 8, *(4)*, pp. 2324-2338, 2017.

S. P. Prieto, C. L. Reed, H. M. James, K. P. Quinn and T. J. Muldoon. "Differences in colonic crypt morphology of spontaneous and colitis-associated murine models via second harmonic generation imaging to quantify colon cancer development." Manuscript under review. *BMC Cancer*, 2018.

Chapter I: Introduction

1. Background

1.1 Clinical imaging and diagnosis of oral and colonic epithelial cancer

Cavities in the gastrointestinal tract, from mouth to rectum, are lined in a layer of epithelial cells [1]. The epithelium, the layer of epithelial cells, forms a barrier between outside substances and the rest of the body's organs and bloodstream, as well as often facilitating the transfer of necessary solutes and solvents from ingested substances [1]. The mucosa consists of the epithelium and an underlying layer of nerves, vessels, and a thin layer of smooth muscle [1]. In the mouth, while there are various types of oral mucosa including masticatory mucosa (tongue, palate, gums), lining mucosa (cheeks, mouth floor, inside of lips), and specialized mucosa (taste buds), the epithelial layer largely consists of squamous epithelial cells [2]. In the gut, the mucosal surfaces vary and can include either squamous epithelium (esophagus) or columnar epithelium (stomach, intestines) [2]. Figure 1 compares the different types of epithelium, including squamous epithelium, which consists of flat cells, and columnar epithelium, which consists of tall narrow cells [2].
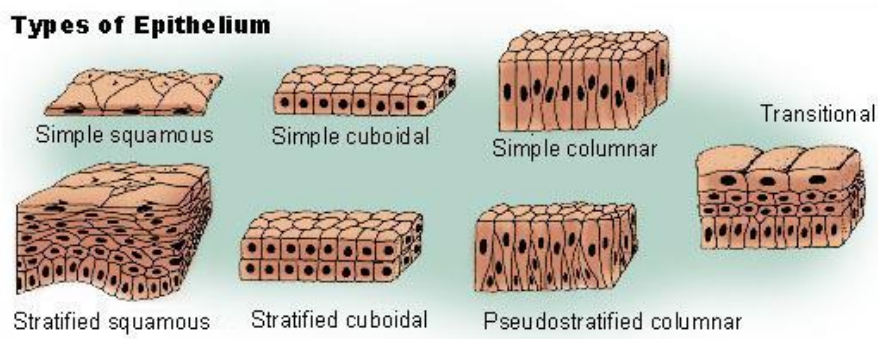
Figure 1. Types of epithelium. Image sourced from seer.cancer.gov webpage [3].

Diagnosis of epithelial dysplasia (abnormal cellular behavior) and cancer is achieved by histopathological analysis of a biopsy or resected tissue. White-light wide-field microscopes are

a clinical standard for imaging and pathological diagnosis of sectioned tissue (such as from biopsies) or fluid samples (such as blood or fecal smears) [4]. Contrast agents are of vital importance in most pathology applications, as the tissues being imaged typically do not exhibit inherent differences in color. Tissue sections are commonly stained with hematoxylin and eosin (H&E) in order to differentiate the nuclei (dark purple) from the surrounding tissue (pink) [4]. Pathologists are trained to detect abnormalities in H&E stained cells by analyzing nuclei (purple) shape and distribution, and cellular (pink) morphology and organization. Examples of oral (Fig. 2) and colonic (Fig. 3b) H&E stained epithelium are shown below [5, 6].
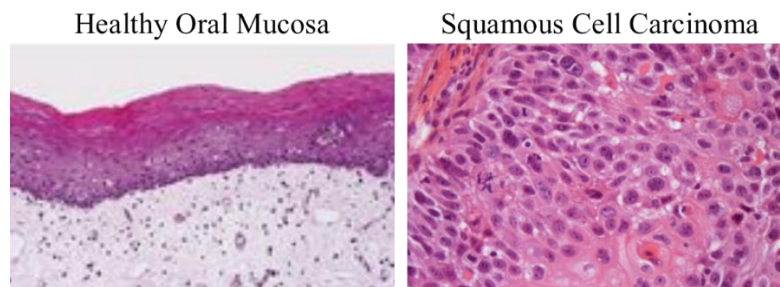
Figure 2. H&E images of healthy oral mucosa and oral squamous cell carcinoma. Images modified; left acquired at x100 magnification, right acquired at x400 magnification [5, 7].

Healthy oral epithelium (Fig. 2a) has a stratified squamous arrangement of cells, with layers of squamous cells (non-proliferating flat cells) laid over basal cells (proliferating cells). Healthy colonic epithelium (Fig. 3a-c) has a columnar arrangement, with cells forming tubular structures called crypts, which have a collagen sheath that provides structure and different types of epithelial cells lining the sheath [8]. *En face* views of healthy crypts display roughly circular crypt openings of homogenous size (Fig. 3c). Basal cells lie at the base of crypts, with differentiated non-proliferating epithelial cells migrating toward the top of the crypt, and are eventually exfoliated into the colonic cavity.

Precursor lesions for oral cancer can take an average of two and a half years to progress to cancer [9]. Patients who regularly smoke and/or drink alcohol are at increased risk since tobacco and alcohol are the two major etiologic agents in oral cancer [9]. Histological findings for white (leukoplakia) or red (erythroplakia) oral lesions can vary, and therefore these lesions are simply flagged for further testing, not used as a final diagnosis [9]. There are various morphological changes that are used in diagnosing oral squamous cell carcinoma (Fig. 2b), including increased nuclear to cytoplasmic ratio, increased number or abnormal mitotic figures, cellular and nuclear pleomorphism (heterogeneity of size/shape), and irregular epithelial stratification [9].

Adenomatous polyps, small benign growths, can sometimes progress into colorectal cancer (CRC) [10]. While most CRC originate from these polyps, they can take years to develop into CRC, with approximately 74% of cases documented in patients over the age of 60 [10]. Early stages of CRC, before the development of grossly visible polyps, will typically include regions of abnormal cellular organization, for example, aberrant crypt foci (ACF) which are enlarged or non-tubular (branching) crypts, and/or multiple layers of cells lining a crypt (Fig. 3d) [11, 12].
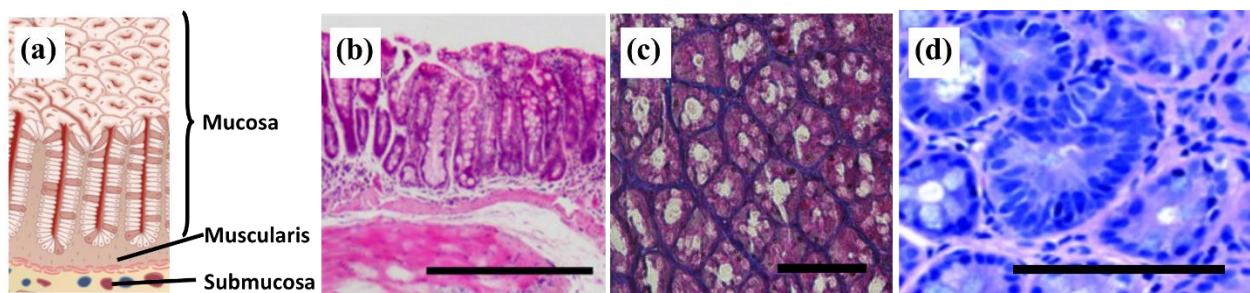
Figure 3. Examples of colon crypt morphology. (a) Representation of crypts in the epithelium; modified figure [13]. (b)Transverse section of colonic murine epithelium; scale bar is 500 µm. (c) *En face* view of epithelial layer; scale bar is 100 µm. (c) *En face* view of an ACF: center crypt is larger and has a higher number of elongated nuclei compressed around the crypt; scale bar is approximately 100 µm. Modified figure [14].

Cytology, which specifically studies cellular image features, is a branch of pathology that has been clinically applied to diagnosis of cells in cervical, anal, and urine smears, and aspirated and exfoliated cells [15-19]. Oral cell cytology, specifically, uses colorimetric stains such as H&E and Papanicolaou for white-light wide-field microscope image acquisition [19]. Another clinical application of white-light wide-field microscopes are endoscopic systems, e.g. colonoscopes. Endoscopic imaging systems usually consist flexible probes that can be inserted into the body to inspect organs, such as the esophagus, stomach, and colon. Colonoscopy systems, used to screen for abnormalities such as discoloration or polyps, consist of a long flexible probe that transmits light from a white-light source to illuminate the colorectal tract as well as transmitting an image back into the external system for acquisition with a wide-field camera. The images are displayed to the clinician in real-time and can be used to guide acquisition of biopsies as needed. While ubiquitous, white-light wide-field imaging systems are not the only imaging modalities used in clinical settings; various additional optical imaging modalities are described below.

1.2 Optical imaging modalities

Microscopes – and microscopy – fall under the category of optical imaging, which according to the NIH is an imaging technique that uses wavelengths in the range of visible light [20]. Other common clinical imaging modalities include MRI (magnetic resonance imaging), X-ray, and CT (computed tomography) systems, but these are not optical imaging modalities. Contrast in MRI is created by a magnetic field, and relies on the differences in radio frequency signals to distinguish between soft tissues (Fig. 2) [21]. Contrast in the X-rays are due to differences in tissue density; dark regions in the black and white image represent low-density regions where the x-ray emissions passed through, and brighter regions represent high-density

regions where calcification (teeth, bone) block the signals from reaching the sensors [22]. CT imaging also uses x-ray, but the sensors are set at many different angles around the patient and the signals are then computationally restructured into multiple images and/or a 3-dimensional model [23].

Advantages of using optical imaging include reduction of patient exposure to radiation, image acquisition of specific or targeted molecules, as well as the option to utilize various colors/wavelengths to probe various properties simultaneously [24]. For example, common dental x-ray imaging systems produce sufficient x-ray radiation to be regulated and considered cause for concern, with CT producing higher doses of radiation [25-27]. While occasional use is not considered to be of high risk, it poses an increased risk to patients undergoing continuous screening/treatment [25, 27]. While optical imaging could cause local damage within tissue if the optical power is high and/or continuous, low level laser therapy has been used clinically and optical power dosage guidelines have been published to prevent adverse effects [28]. High optical power even has been used in combination with experimental drug delivery carriers, which are activated by targeted pulses of high optical power in order to obtain an accurate and controlled increase temperature in a region of interest [29, 30]. Another advantage of optical imaging is the ability to stain or immunolabel different molecules with different colorimetric markers and simultaneously or sequentially acquire images of various molecules in the same sample [31, 32]. An example of this are composite fluorescent images of cells that display blue nuclei and red actin fibers [33].

MRI does not carry the risk of radiation, but is also is limited to probing for differences in density in soft tissues, whereas optical imaging systems, such as H&E staining of tissue sections or multiphoton microscopy, can acquire functional information such as nuclear and cellular

morphology [34, 35]. The greatest disadvantage of optical imaging is the scale, or field of view and depth, that can be acquired using the visible light spectrum. Wide-field microscopes require thin sections of tissue, typically in the range of 5μm-10μm, or equally thin smears of fluid samples. Microendoscopes are limited to investigating the topmost layers that the imaging probe comes into contact with. Multiphoton imaging is the most capable of imaging deeper into tissue, up to several hundred microns into tissue depending on the type of tissue [36].

Fluorescence and fluorescence microscopy

Due to the central role of cellular morphology in clinical diagnosis, optical imaging alternatives to tissue removal and subsequent H&E staining have been widely investigated. Sources of contrast in imaging of epithelium range from colorimetric stains, to fluorescence and autofluorescence. Colorimetric stains, such as the previously described H&E (Fig. 2), Giemsa, and others, display visibly distinguishable colors when viewed with a white light source [4, 37]. Fluorescence, in broad terms, is the result of electrons in susceptible molecules absorbing energy when targeted with light (excitation), becoming energized and entering a higher energy state, and releasing a reduced amount of the energy (emission) when returning to their original state (Fig. 4a). As can be seen in Figure 4b, the blue extinction curve displays the efficiency of various excitation wavelengths (intensity of the fluorescence when excited at a given wavelength) and the orange emission curve represents the intensity of different emitted wavelengths when excited with 400nm light. Fluorescent contrast agents can be applied to add contrast to cellular structures, or highly sensitive imaging systems can be used to acquire fluorescent signals from endogenous fluorophores present in cells [34, 35].
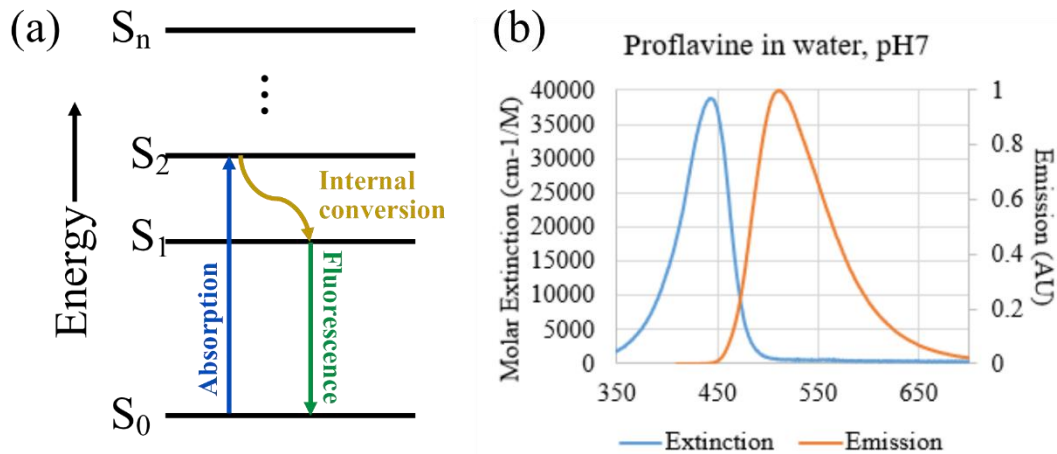
Figure 4. Example of fluorescent excitation and emission. (a) Jablonski diagram showing an electron being excited by a photon into a higher energy state, then relaxing and releasing fluorescent light. (b) Extinction/emission curves for proflavine; adapted from PhotochemCAD 2 data [38].

Cells have some measure of endogenous fluorescent molecules, but these fluorescent emissions are too dim to image using wide-field microscopy. Confocal imaging systems are sensitive enough to capture this endogenous fluorescence, though sometimes confocal systems will still be used in conjunction with fluorescent contrast agents. Confocal laser systems rely on a small pinhole to eliminate out-of-focus light, and this pinpoint of light is scanned across the field of view, acquiring an image pixel by pixel using highly sensitive detectors (photomultiplier tubes). Fluorescence imaging, including confocal microscopy systems, have a light source of higher-energy/shorter-wavelength which is used to stimulate the emission of lower-energy/longer-wavelength signals.

Multiphoton fluorescence microscopy: two photon excitation

In contrast to confocal systems, multiphoton microscopy takes advantage of a phenomenon in which two (or more) photons of light excite a molecule at virtually the same time and place (a cross section of 10^{-50} cm^4 s) and the electron absorbs the energy of both and therefore releases light of longer wavelength than the combined energy, but shorter than the

original light source (Fig. 5) [39]. Practically, this means that a pulsed high-frequency red light

can be used to excite molecules that typically require blue light excitation. Due to the reduced

Rayleigh scattering of longer wavelengths, multiphoton microscopy allows for imaging deeper

into tissue sample, as well as virtually eliminating any shorter wavelength excitation outside of

the focal plane [39]. This reduction of out-of-focus fluorescence means that multiphoton imaging

is ideal for label-free imaging of endogenous fluorophores present in tissue.
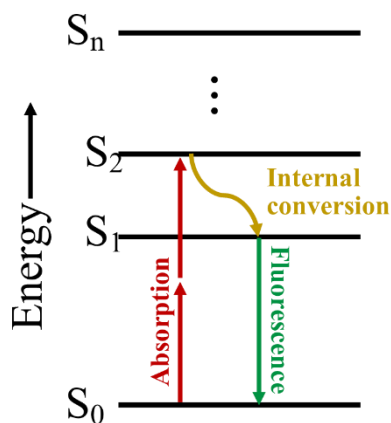
Figure 5. Example of two-photon fluorescence. Jablonski diagram showing an electron being excited by a combination of two photons into a higher energy state, then relaxing and releasing fluorescent light.

Second harmonic generation imaging

Multiphoton imaging systems have also been used for acquiring second harmonic

generation (SHG) signals. SHG is a nonlinear optical process in which two equal-energy photons

interact with a nonlinear medium and produce, without absorption nor energy loss, a single

photon of half the original wavelength of the excitation [40, 41]. A linear optical process is when

two waves (sound, light, etc.) combine constructively, where components combine into a single

wave of greater amplitude, or destructively, where positive and negative components cancel out

into a lesser amplitude or completely zero [40, 41]. A nonlinear optical process is when two light

waves do not combine to produce a greater amplitude, but combine to produce a wavelength of equal amplitude but higher frequency [40, 41]. SHG requires a nonlinear medium to mediate this production of higher-frequency photons. The refractive index of a nonlinear medium changes with light intensity, thereby changing speed/frequency [40, 41]. This process usually occurs at high frequencies, such as in pulsed photons emitted by a femtosecond laser (commonly used in multiphoton microscopy), and depends on the degree of the polarization of a nonlinear medium [40, 41]. This nonlinearity, including the polarization of the medium, leads to the generation of a wave at twice the original frequency. This means that certain nonlinear endogenous molecules, most relevant for this manuscript being collagen, can be imaged using multiphoton microscopy.

The following sections describe different optical imaging modalities, contrast agents, and techniques that were applied to investigation of morphological image features in oral and colorectal epithelial cancer cells.

2. Proflavine as a contrast agent for oral cell cytology

2.1 Oral squamous cell carcinoma

Oral and pharyngeal cancer is the sixth most common cancer worldwide, with two thirds of cases arising in developing countries [42]. In countries with the highest incidence rates, for example Sri Lanka and India, oral cancer is the most common cancer in men, contributing up to 25% of all new cancer cases [42]. Oral squamous cell carcinoma (OSCC), one subtype of oral cancer, is the most common malignant tumor of the head and neck [43]. For many populations, including Asia, tongue and buccal (cheek) mucosa are the most common incident sites of oral cancer [44]. Oral epithelial dysplasia (OED) is the histological marker of premalignancy, and carries an increased risk for developing OSCC [45]. Typical histological markers to diagnose OED include, but are not limited to, loss of cellular organization, enlargement of nuclei, basilar

9

hyperplasia, mitosis above the basal cell layer, and skip areas of dysplasia [46]. In 16% of cases, OSCC developed within 6.5 years after an OED diagnosis [46].

OSCC is diagnosed either during a routine inspection of the oral cavity by a dentist or physician, or due to a patient presenting discomfort or suspicion [47]. In a low-resource location in Bangladesh, 85%-95% of cases in a clinical study had a history of irregular (less than yearly) dental visits, reducing the likelihood of early detection of OSCC [48]. In order to address this lack of medical surveillance in low-resource settings, there have been various attempts made to conduct screening initiatives, such as sending health workers and volunteers to rural areas in order to conduct routine inspections, specifically looking for white or pink lesions, or visible growths [49]. A study by Wesley *et.al.* compared results from two cancer detection camps versus youth volunteers sent to visit households in the area and reported more favorable results from the cancer detection camps [50]. Studies reported compliance (accepted invitation for follow-up at a clinic) percentages for industrialized countries as high as 100%, while most studies conducted in the Indian sub-continent hovered around 50% [50]. While screening initiatives have provided many with the opportunity for earlier detection of OSCC, there is still a need for point-of-care diagnosis that can more easily reach these high-risk populations.

In order to increase early diagnosis, and therefore increase survival rates, multiple screening tools for oral cancer have been developed to diagnose lesions early, expedite treatment, and do not necessitate high levels of training. Alternative oral screening procedures are designed to collect exfoliated cells, such as oral rinses and oral brushes to more stringently exfoliate cells of a suspicious region, for subsequent histopathological examination [51]. Kujan *et. al.* discussed the difficulty of using cervical cytobrushes for their oral study, due to "their size and shape", since at the time there was no commercially available cytobrush [52]. Currently, the

most commercially accepted clinical on-the-market oral screening tool is the OralCDx brush, which is marketed for scrubbing of suspicious regions, then sending the brush and exfoliated cells to their laboratory for diagnosis [53, 54]. Investigational cytological studies included similar procedures, and stained the exfoliated cells with a variety of contrast agents [51].

2.2 Cytological contrast agents

Once oral cells have been exfoliated, one of many contrast agents are applied in order to highlight the morphological image features used to determine a diagnosis [55]. The most common cytological contrast agents in oral cytology are Feulgen, acridine orange, propidium iodine, Giemsa, May-Grünwald-Giemsa, and ethidium bromide [55]. These contrast agents fall into either the category of a colorimetric contrast agent that requires white light and a color camera, or a fluorescent contrast agent that requires a small range of excitation wavelengths (e.g. an LED or laser) and a filter set. While colorimetric stains (e.g. Feulgen, Giemsa) are current contrast agents used for oral cytology, fluorescent dyes (e.g. acridine orange, propidium iodine, ethidium bromide), depending on the stain and the application, have benefits that include higher signal to background during imaging, rapid staining, little or no need for fixation, low cost, and minimal need for lab tools. Qualitatively, fluorescent imaging is comparable to colorimetric methods when considering morphological features, specifically nuclei size and distribution.

Propidium iodine and ethidium bromide are commonly used in live/dead cell assays, and therefore the majority of the studies where they were used as contrast agents, they were used to stain the nuclei of dead or fixed cells, or were shown incapable of staining any of the nuclei in the live cells of the study [55]. An alternative in the acridine derivative family is acridine orange, which is used in many applications requiring different colorimetric features to differentiate cells with varying cellular content, such as the acidic vesicles [56, 57]. However, the fluorescence

emissions of acridine orange are dependent on concentration, pH and incubation time and it requires strict control. For applications where colorimetric-based differentiation between multiple cell types is not necessary and morphological features would suffice, proflavine would be a more suitable contrast agent for oral cytology.

Proflavine is a fluorescent DNA-intercalating dye, of the aminoacridine derivative family, with amphipathic properties that allow for rapid absorption into the cell cytoplasm and nuclei [58]. Proflavine has been used clinically since 1917 [59], but its use as a cytological tool is not widespread despite its potential advantages, though there has been renewed interest in its use for point-of-care diagnostic applications in low-resource settings due to its physical and chemical stability in solution [60]. Proflavine is very stable in solution, up to 12 months if refrigerated [60]. Proflavine is useful in applications that require minimal preparation and staining steps, as well as high signal to background, as a fluorescent dye that can rapidly stain live cells, unlike the previously described contrast agents, and is not pH dependent, unlike other dyes in the aminoacridine family.

2.3 Objective

Rapid identification of oral cells with large nuclei to cytoplasm ratios using low-cost fluorescence imaging systems could serve in further development of point-of-care OSCC screening tools. Proflavine, a DNA-intercalating vital dye, could serve as an alternative contrast agent for oral cytology screening systems in regions where clinical pathology services are not readily available.

3. Image feature quantification and alternative contrast agent for a translational microendoscopy system

3.1 Colorectal cancer

Colorectal cancer (CRC) causes approximately 50,000 deaths per year in the United States, with 14.5 deaths per 100,000 men and women [61]. When diagnosed early, the 5 year survival rate can be over 90%, but unfortunately over 20% of cases are diagnosed at a late stage when the survival rate drops below 14% [61]. There are various types of CRC, including familial, familial adenomatous polyposis (FAP), hereditary nonpolyposis (HNPCC), ulcerative colitis/Crohn's disease related, rare syndromes such as Lynch and hamartomatous polyposis syndromes, and – the most prevalent – spontaneous adenocarcinoma [62, 63]. Spontaneous adenocarcinomas, accounting for 65-85% of CRC cases, commonly arise from adenomatous polyps, some of which may progress into invasive adenocarcinomas over time (Fig. 6) [62, 64]. This progression is thought often take years (up to a decade) and be dependent on the size and histology of the polyp [65]. Routine screening can lead to early detection and removal of polyps, which can reduce the number of CRC deaths.
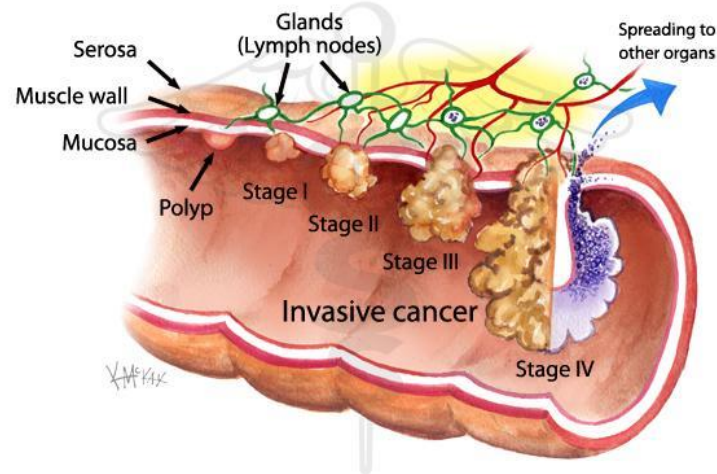
Figure 6. Stages of colorectal cancer. Image sourced from www.shsg.com.au.

Routine screening of CRC depends on traditional colonoscopy, which utilizes long flexible probes attached to a white light illumination source and a wide-field color camera, which is then inserted into the colon to screen for any grossly visible polyps [6]. The physician inspects for any visible growths or suspicious lesions, such as discolored or inflamed epithelium [2]. Small polyps can be removed immediately during the colonoscopy [66], and are sent to the pathologist to determine if it was a benign growth or if it requires additional removal of surrounding tissue. Any suspicious lesions are biopsied, the recommended number being four-quadrant biopsies every 10 cm [67]. Due to the increased number of people undergoing routine screening, yearly CRC cases for those over 50 years of age have decreased 32% between 2000 and 2014 [68]. Despite this decrease, CRC remains the second leading cause of death in the US, and third leading cause worldwide [61].

3.2 Recurrence and endoscopic imaging of colorectal cancer

Once a polyp has progressed into CRC, the curative standard for CRC is excision of the tumor, often followed by surveillance for recurrence [69, 70]. Chemotherapy and radiotherapy are common treatments designed to reduce the size of the tumor before resection, and/or prevent metastasis of cancer cells from the tumor [69, 70]. Despite therapeutic treatment, recurrence is a common outcome after resection of the primary tumor. In one randomized study, cancer recurred in 44% of patients, leading to further surgery [70]. The majority of these recurrence-related surgeries were performed within the first two years following the initial resection [70].

There are a number of tools that have been developed to determine recurrence during surveillance of patients, including detection of a range of salivary protein markers [71]. An alternative technique is the investigation of endoscopic imaging modalities, since operating rooms and clinicians are already equipped for these imaging systems due to the widespread use

of endoscopic probes, such as during colonoscopies or robotic surgery [72]. Examples of imaging modalities that have been developed and tested in colorectal epithelium include chromoendoscopy, indigo carmine staining in conjunction with traditional colonoscopy, and microendoscopy. There are a variety of sources of contrast used in endoscopic imaging of colorectal epithelium, such as colorimetric stains in chromoendoscopy, hemoglobin absorption in narrow-band imaging, fluorescence in microendoscopic imaging, and autofluorescence in confocal and multiphoton imaging systems. Chromoendoscopy typically uses a colorimetric contrast agent, such as indigo carmine, to enhance dysplastic regions under traditional white light colonoscopy [73]. Narrow band imaging has been described as label-free chromoendoscopy, as optical filters only allow imaging of a small range of wavelengths, which enhance blood vessels and contrast in capillary patterns without the need for indigo carmine or another contrast agent [74, 75]. Laser endomicroscopy allows for imaging of cellular and subcellular structures, providing more detailed imaging of features that relate more closely to histopathological features [76].

One robust imaging modality, fluorescence microendoscopy, combines the untargeted staining method of chromoendoscopy with the microstructural detail of microendoscopy. Microendocopy is an imaging system that has been investigated due to its robust and relatively inexpensive build, and its ability to provide a detailed look at cellular structures that are not visible during routine wide-field endoscopy [77-79]. Microendoscopy imaging techniques that have been developed to provide complementary information for the clinician during a colonoscopy include autofluorescence endoscopy with image processing, narrow band reflectance imaging, and combined multimodal methods [66, 80, 81]. Microendoscopic imaging using proflavine (the previously described DNA-intercalating fluorescent contrast agent) has

15

been investigated in clinical settings, in conjunction with manual quantification of image features [79, 82-86]. Limitations of fluorescence microendoscopic imaging include limited imaging depth and small field of view. Advantages of microendoscopic imaging using proflavine include rapid staining times, no need for rinsing, high signal to background ratios, and high-resolution of cellular structures. Qualitative analysis of morphological structures (such as glandular shape, epithelial thickness, and nuclear organization) in images acquired with fluorescence microendoscopy by trained observers has been shown to be highly sensitive and specific (over 90% for both) [86]. Since the use of proflavine has been limited to investigative studies, we have also explored the use of fluorescein as an alternative contrast agent to proflavine, due to its FDA-approved intravenous use for alternate applications [87].

3.3 Manual and automated quantification of morphological image features

An additional tool that we investigated was the automated quantification of image features, specifically the size and shape of crypt structures. Image feature quantification could be defined as numerical measurement of an object or multiple objects in an image, as opposed to coming to a conclusion or diagnosis based on observation alone. Counting polyps in the colorectal tract during routine colonoscopies is a basic example of image quantification; a diagnosis of familial adenomatous polyposis "is made when at least 100 colonic adenomas are identified" [88]. This example highlights how thresholds, such as the numerical value of 100 polyps, can be determined based on clinical studies, and can be used as a suggested value for diagnosis.

Manual quantification exists in varying degrees in cancer research and clinical workflow, such as the aforementioned examples of polyp counting during a colonoscopy. Manual quantification retains the advantages of observer-based analysis and image quantification by

using trained clinicians to accurately select important image features (such as distinguishing polyps from surrounding tissue), and adds the advantage of numerical results that can be replicated and used to create thresholds and ranges of normalcy (such as selecting 100 polyps as a numerical threshold). When comparing diagnoses of dysplasia – presence of abnormal cellular morphology and/or organization that are a precursor to cancer – in colorectal microendoscopy images by experienced clinicians, inter-observer variability among trained observers was 96% [89]. While manual quantification retains the high accuracy feature analysis when using trained clinicians, it also retains the disadvantage of requiring an experienced observer, as well as the burden of spending increasingly longer periods of time spent analyzing the data especially as modern imaging systems increase their capability of acquiring large image data sets.

Automated quantification uses trained algorithms to select, segment, and quantify image features independent of the user. Automation is targeted at the reduction of the burden of time on trained clinicians, as well as reducing user-bias and error of minimally trained clinicians or researchers. Minimally trained users are more likely to include false positives or a false negative. An example of a false positive would be determining that a certain cell is dysplastic when it is healthy, while a false negative would be determining that a certain cell is healthy when it is dysplastic [89, 90]. A few of the studies that utilize automated quantification include automated image segmentation of cells to measure cellular metabolic rates [91], segmentation of renal sections to calculate fibrosis [92], and 3-dimensional fiber orientation [93].

3.4 Objective

Automated quantitative analysis of morphological features in microendoscopic images can provide an objective method of distinguishing between normal and neoplastic regions. Complementary microendoscopic-level information can be included into traditional colonoscopy

workflow, as demonstrated by various studies, and can increase detection of neoplastic lesions at an early stage, with automated quantification minimizing user effort and bias. The use of fluorescein, currently approved for intravenous use in certain clinical applications, in conjunction with these microendoscopic systems could provide investigators an alternative contrast agent with similar quantitative results for translation into *in vivo* study.

4. Second harmonic generation imaging of murine epithelium for crypt morphology image feature analysis of spontaneous and colitis-associated colorectal tumors

4.1 Ulcerative colitis and colorectal cancer

Ulcerative colitis (UC) and Crohn's disease are the two major forms of inflammatory bowel disease (IBD), which is characterized by chronic inflammation of the gastrointestinal tract [94]. UC is characterized by severe inflammation and extensive ulcers on the epithelial surface of the gastrointestinal tract [95]. Crohn's disease is characterized by lesions over Peyer's patches (lymphatic tissue found in the ileum region), and the inflammation is non-continuous in location as well as spanning the entire depth of the intestinal wall [95-97]. There has been progress in discovering possible genes that contribute to disease susceptibility, as well as a rise in IBD patients in previously low-risk countries showing the likely correlation between environmental factors and IBD, but despite these studies there is still much of the pathogenesis of IBD that is yet to be understood [95].

While there is no individual endoscopic or histological result that is specific for UC or Crohn's disease, an important distinction is the distribution pattern of the inflammation. UC is diagnosed when examination shows continuous inflammation of the colon beginning at the rectum, whereas a diagnosis of Crohn's disease is determined when there are lesions over Peyer's patches [95-97]. Patients with UC have long been considered at increased risk for

colorectal cancer (CRC), though there are less conclusive studies on the risk of CRC in patients

with Crohn's disease [98-102]. While both types of IBD are associated with inflammation, in UC

pro-inflammatory cytokines are believed to directly influence cancer progression [103], and

patients are commonly provided with anti-inflammatory therapy, such as 5-aminosalicylic acid

[62]. Unfortunately, even this therapy is only able to achieve remission in 1 of 6 patients [104].

4.2 Spontaneous and colitis-associated tumor development in ulcerative colitis patients

Due to the high risk of UC patients developing CRC over time, if malignant lesions are

discovered the standard of care is curative colectomy (complete removal of the colon) [62, 105].

Within 10 years of diagnosis, approximately 29% of UC patients develop CRC compared to

2.9% of patients with Crohn's disease [99, 101, 106, 107]. UC patients are more often considered

candidates for curative colectomy, since they have continuous inflammation of the colon [108].

The gold standard for detection and diagnosis of malignant lesions and/or tumors in IBD patients

is routine surveillance colonoscopy and subsequent endoscopic biopsy. Surveillance procedures

are designed to detect early dysplasia and neoplasia (pre-cancerous abnormalities), in order to

prevent CRC progression. Two types of lesions detected during colonoscopy, associated with

intraepithelial neoplasia, are dysplasia-associated lesion/masses (DALM) and adenoma-like

masses (ALM) [74, 105]. A DALM is classified when a lesion is flat or raised but does not have

a sharp contrast against surrounding healthy epithelium, and this type of lesion is frequently

associated with malignancy [74]. Endoscopically, an ALM lesion has features similar to

spontaneous protruding adenomas that are observed in non-IBD patients [74].

In non-IBD patients, for example those with spontaneous polyp (non-cancerous) growth,

the standard procedure is a polypectomy which completely resects the mass [74, 105]. Recent

studies have suggested that polypectomy of an ALM mass in IBD patients is highly successful,

and could postpone the need for curative colectomy [74, 105]. In contrast, a retrospective study

showed that a higher proportion of unresectable lesions harbored cancer [109]. The

histopathological differences between ALMs and DALMs are subtle and varied, and an accurate

diagnosis determines if the patient will undergo endoscopic polypectomy or surgical colectomy

[74]. The diagnosis must also take into account additional factors such as patient age, duration of

disease, and if the lesion is within the region affected by colitis [62]. The recommendation of an

international consensus in 2005 was to perform four-quadrant biopsies every 10cm, with a

minimum total of 32 biopsies during surveillance [67]. Despite surveillance, between 50% and

80% of DALM lesions are not visible during traditional endoscopy [110].

4.3 Endoscopic imaging of UC patients

In order to improve detection of easily missed lesion, various endoscopic imaging

modalities have emerged to provide additional information during the surveillance of IBD

patients, including chromoendoscopy, narrow band imaging, and laser endomicroscopy [73]. The

first study of chromoendoscopy in IBD patients was published in 2003, in which the colonic

epithelium was sprayed with 0.1% indigo carmine (a colorimetric contrast agent), and the results

showed that three times as many neoplastic lesions were detected via chromoendoscopy than

with traditional colonoscopy [73]. Magnification chromoendoscopy detection of intraepithelial

neoplasia was four times as high as traditional colonoscopy [111]. Narrow band imaging, as

previously described, can image blood vessels and capillary patterns without the need for indigo

carmine or another contrast agent [74, 75]. While these imaging modalities have increased

detection of lesions, they cannot distinguish between ALMs and DALMs, as the image features

are similar [74]. Laser endomicroscopy allows for imaging of cellular and subcellular structures,

providing more detailed imaging of features that relate more closely to histopathological features

[76]. A combined study of chromoendoscopy and endomicroscopy showed a 4.75-fold increase in detection of lesions, as well as a 50% reduction in the number of required biopsies [73].

Laser endomicroscopy could describe either confocal or multiphoton laser endomicroscopy systems, both of which can provide high-resolution depth-sectioned information on changes in cellular and even subcellular structures. Confocal laser endomicroscopy systems in studies were dependent on contrast agents, such as the contrast provided by intravenous fluorescein (a fluorescent contrast agent), and therefore provided images of structure and morphology based on blood flow patterns [76]. Neoplastic regions predicted by the system were compared to histopathology and found to be highly accurate (97% sensitivity, 99% specificity) [76]. In patients with UC, a study showed that the combination of chromoendoscopy and endomicroscopy increased the discovery of neoplastic regions 4.75-fold [76]. An in vivo case studied a DALM lesion and adjacent colorectal epithelium, using the Cellvizio ® Endomicroscopy System (Mauna Kea Technologies, Paris, France), a 2.5mm catheter imaging probe inserted into an existing working channel during colonoscopy, and 5mL of 10% sodium fluorescein injected intravenously [112]. Acquired confocal images showed enlarged crypts, increased irregularity in the distribution of crypts, increased space between crypts, as well as crypt destruction or fusion [112]. They also showed the transition from inflamed mucosa (due to ulcerative colitis) to dysplastic mucosa [112]. Inflammation was characterized by enlarged crypt openings, with leaking of fluorescein into the crypt lumen that appeared as bright regions in the crypt center, while low-grade dysplastic regions were characterized by dark centers with irregular structural patterns [112].

Previously mentioned imaging methods, such as chromoendoscopy and confocal imaging with intravenous fluorescein, require a contrast agent which can have various disadvantages.

Chromoendoscopy requires topical application of the contrast agent, followed by rinsing, and there are reports of the contrast agent not homogenously covering all the epithelial surfaces of interest in addition to the amount of time each of these application and rinse cycles can take (after applying the contrast agent, there is a 5 minute wait before rinsing) [73]. In addition, these contrast agents are not targeted to a specific protein or molecule, therefore the images provide important information on vasculature patterns and morphological structure, but do not provide more specific cellular information. Narrowband imaging does not require an external contrast agent, but it also predominately images vasculature patterns. Multiphoton microscopy is capable of acquiring label-free images of bulk tissue without need for fixation, and rapid 3-dimensional image acquisition up to several hundred microns [40]. Contrast for fluorescence imaging using multiphoton microscopy comes from the endogenous fluorescence of cellular molecules such as NADH and FAD, which have been investigated as providing insight into metabolic information [34, 35]. Miniaturization of multiphoton laser microscopy systems allows for *in vivo* imaging, utilizing the advantages of multiphoton acquisition of functional data without need for a contrast agent, in combination with using near infrared wavelengths to image tissue at increased depth [113, 114].

4.4 Second harmonic generation imaging applications

Second harmonic generation (SHG) imaging is an alternative imaging method accessible when using multiphoton microscopy. The first biological application of SHG imaging was in 1986, investigating the polarity of collagen fibers in rat tail tendons [115]. Collagen type I makes up much of extracellular matrix (ECM) and connective tissue, and has a history of being investigated via SHG imaging [113, 116]. Collagen fibers are a nonlinear medium due to their non-centrosymmetric nature (their crystal structure cannot be inverted without change since it

22

does not have a point of symmetry), and the polarization of the fibers can be studied using SHG imaging [117]. SHG imaging in healthy colorectal epithelium highlights crypt shape, as the collagen fibers provide structure surrounding the cellular arrangement [118, 119]. Miniaturized multiphoton microendoscopes have been shown to be capable of SHG imaging of bulk tissue. Miniaturized multiphoton label-free fluorescence imaging of intact rat tissue has been reported as early as 2001 [120], with endogenous fluorescence and SHG images of fixed murine tail tendons acquired in 2009 [121], and in 2011 a 3mm-diameter multiphoton endoscopic probe was shown to acquire both endogenous fluorescence and SHG images of ex vivo murine tissue (tail, lung, and colon) [114]. The addition of a SHG imaging channel to multiphoton microendoscopes would provide supplemental structural information about connective tissue, such as collagen, tendon, and muscle without the need for contrast agents [122]. Preliminary work on SHG imaging in a murine CRC model has shown SHG imaging of epithelium as providing data on collagen structural changes that could be used as early indicators of disease [123].

4.5 Objective

Increasing the ability to distinguish between spontaneous (ALM) and colitis-associated (DALM) tumors in UC patients could guide clinicians in appropriate treatment. Emergence of multiphoton endoscopic systems allow for combination of functional and structural data to improve detection and diagnosis of ALM and DALM regions in UC patients, and a quantitative study of structural/morphological SHG data in these tumor models had not been documented. SHG image features could serve as complementary data during multiphoton microendoscopic imaging, and provide insight on collagen changes during crypt deformation, which could serve a translatable measure towards detection and distinction of lesions in UC patients.

5. Specific Aims

Introduction

Early detection of oral and gastrointestinal cancer is crucial in decreasing the risk of morbidity; if detected early, the 5-year survival rate for oral cancer and colorectal cancer is on average 82% and 92% respectively [61]. For oral cancer, cellular morphological markers of cancerous cells include large nuclei and large nucleus to cytoplasm ratio [46]. For colorectal cancer, there are known changes in morphological structure of crypts – cells organized into cylindrical structures – such as enlarged crypts and loss of cylindricity [11, 12, 124]. Analysis of morphological markers, such as nuclear size and crypt cylindricity, is typically performed via histopathology [9, 12]. Since histopathology requires tissue biopsy or resection, often followed by sectioning, then staining, one area of investigation has been rapid or *in vivo* imaging of morphological markers.

Optical imaging of cellular structures makes use of wavelengths of visible light, distinct from magnetic resonance (MRI) or high frequency wavelengths (x-ray, CT) [21-23]. Optical imaging modalities range from inexpensive portable devices to expensive investigational systems. Many of these systems, both expensive and inexpensive, are being adapted for integration into existing clinical workflow. Low-cost fluorescent systems can be used to analyze cell morphology in conjunction with fluorescent contrast agents, while expensive devices are capable of acquiring contrast from endogenous optical signals in unstained tissue. Analysis of cellular morphology has the potential of detecting abnormal changes in tissue, such as dysplasia or cancer, before they are grossly visible. The following aims were designed to address the investigation and optimization of morphological imaging of epithelial cancers, specifically oral and colon cancer, for early detection.

Specific Aim 1: **Proflavine as a Contrast Agent for Oral Cell Cytology**[1]

Background: Oral and pharyngeal cancer is the sixth most common cancer worldwide, with two thirds of cases arising in developing countries [42]. While oral squamous cell carcinoma (OSCC) is commonly detected during regular physician or dentist visits, as high as 95% of populations in low-resource settings declare a history of irregular dental visits, increasing the risk for OSCC to develop to late stages without detection [48].Conventional clinical cytology requires biopsies, fixing, and staining, and investigators have designed alternative protocols, such as oral rinses and brushes, which can collect exfoliated oral cells for cytological analysis. For both conventional and investigational oral cytology, morphological image features guide diagnosis of epithelial cells, where healthy cells are relatively large with small nuclei while oral cancer cells have a large nucleus to cytoplasm ratio [46].

Low-cost translational devices for cell cytology have used a variety of contrast agents in order to analyze morphological markers, including fluorescent contrast agents that have advantages that include high signal to background, rapid staining, and low cost. The use of proflavine, a rapid fluorescent vital dye, in cytology of OSCC has not been studied. Proflavine could serve as an alternative contrast agent for future translational cytological devices.

Objective: Rapid identification of oral cells with large nuclei to cytoplasm ratios using low-cost fluorescence imaging systems could serve in further development of point-of-care OSCC screening tools. Proflavine, a DNA-intercalating vital dye, could serve as an alternative contrast agent for oral cytology screening systems in regions where traditional pathology services are not readily available.

---

[1] Full manuscript available as Chapter II

Aim 1: Determine the viability of proflavine as an alternative contrast agent for oral cytology.

Our study qualitatively and quantitatively investigated the utility of proflavine solution in imaging of exfoliated oral cells for OSCC screening. We examined the potential of proflavine as a contrast agent for oral cell cytology, using a portable (POC capable) microscope in order to qualitatively distinguish differences between healthy and cancerous cells, and quantitatively distinguish morphological differences (specifically nuclear to cytoplasm ratio).

Results: Images of proflavine-stained cells show morphological detail similar to traditional staining, with bright distinguishable nuclei and granulation (keratohyalin). Quantification of nuclear to cytoplasmic ratio in the images showed significantly ($p < 0.001$) larger ratios in OSCC cells compared to normal cells, where OSCC cell ratios averaged above 0.8 compared to normal cell ratios averaging below 0.1.

Significance: Our comparison of nuclear to cytoplasmic ratios could help guide future POC imaging system design for low-resource oral cytology screening. Quantitative analysis of image features in oral cell cytology using proflavine had not been investigated. Future studies could use one-step proflavine staining to qualitatively inspect cells, or computer-aided image segmentation could be implemented to measure nuclear size and create rapid analysis of exfoliated oral cells.

Specific Aim 2: Image feature quantification and alternative contrast agent for a translational microendoscopy system[2]

Background: Colorectal cancer (CRC) is the second leading cause of cancer death in the United -States [61]. After resection of the primary tumor, recurrence remains a common outcome; cancer recurred in 44% of patients, requiring further surgery [70]. Increased screening using traditional white-light wide-field colonoscopy has led to a decrease in morbidity in the past few

---

[2] Full manuscripts available as Chapters III and IV

decades, but it is not an ideal imaging modality for detection of sessile or flat lesions [77-79]. Various techniques have been investigated for surveillance of at-risk patients, including salivary protein markers, but endoscopic imaging systems have several advantages [71]. Endoscopic imaging systems analyze cellular and crypt morphology, which pathologists are trained in identifying. In addition, conventional colonoscopy already has clinical protocols and physical tools in place for endoscopic imaging, thereby facilitating translation of these imaging systems into *in vivo* clinical settings [72].

Microendoscopic imaging systems have been studied in CRC patients and quantitative analysis of a clinical fluorescence microendoscopy images using proflavine as a contrast agent has shown up to 98% specificity in diagnosis of neoplastic polyps [86]. *In vivo* clinical diagnosis was made on morphological image features based on crypt morphology, including nuclear organization and epithelial thickness [86]. Viability of automated quantification of these image features, specifically crypt size and circularity, in microendoscopic images has not been studied.

Objective: Automated quantitative analysis of morphological features in microendoscopic images can provide an objective method of distinguishing between normal and neoplastic regions. Complementary microendoscopic-level information can be included into traditional colonoscopy workflow, as demonstrated by various studies, and can increase detection of neoplastic lesions at an early stage, with automated quantification minimizing user effort and bias. The use of fluorescein, currently approved for intravenous use in certain clinical applications, in conjunction with these microendoscopic systems could provide investigators an alternative contrast agent with similar quantitative results for translation into in vivo study.

Aim 2: Quantification of microendoscopy images toward computer-aided analysis of crypt morphology in colorectal cancer. Our study investigated the potential of automated

quantification of crypt size and circularity in microendoscopic images using a custom algorithm. We tested the algorithm's ability to quantify images of normal and abnormal colorectal epithelium, using both proflavine and fluorescein as contrast agents.

Sub-aim 1: Development of a custom algorithm for automated analysis of microendoscopic image features. Acquired images of *ex vivo* porcine colorectal epithelium stained with proflavine, a contrast agent used in clinical studies, for development of a custom algorithm for automated image segmentation and quantification of crypt size and circularity. Quantitatively compared preliminary data from freshly resected clinical colorectal tissue.

Sub-aim 2: Determine the viability of fluorescein as an alternative contrast agent for microendoscopic imaging. We tested our previously developed algorithm on images of fluorescein-stained *ex vivo* human and animal epithelium, to determine the feasibility of using fluorescein as an alternative contrast agent in microendoscopic imaging. We compared crypt detection sensitivity of the automated algorithm in proflavine versus fluorescein stained normal and abnormal colonic epithelium.

Results: Our custom algorithm showed above 80% crypt detection sensitivity using images of proflavine-stained freshly resected porcine and human epithelium. Preliminary comparison of normal and adenomatous diagnoses in human epithelium showed increased crypt area and circularity in adenoma-adjacent regions. The custom algorithm yielded better crypt detection sensitivity (>90%) using fluorescein, an alternative contrast agent for microendoscopic imaging. Preliminary results using fluorescein in *ex vivo* clinical specimens showed a decrease in average crypt size in regions of adenocarcinoma when compared to normal regions.

Significance: Microendoscopic imaging has been qualitatively investigated as a potential intraoperative aid during surveillance colonoscopy, but quantitative analysis of crypt

28

morphology as biomarkers of carcinoma had not been documented for this system. Our results could guide implementation of automated quantification in microendoscopic system design, including image features such as area and circularity which resulted in significant differences between normal and cancerous regions. The use of *in vivo* automated quantification could be further studied for future translation into clinical settings during CRC surveillance. In addition, the use of intravenous fluorescein as an alternative contrast agent for confocal endomicroscopy imaging systems has been studied, but our results show that topical application is a viable alternative for microendoscopic imaging [112, 124].

<u>Specific Aim 3:</u> Second harmonic generation imaging of murine epithelium for crypt morphology image feature analysis of spontaneous and colitis-associated colorectal tumors[3]

Background: Spontaneous polyp, and subsequent tumor, formation accounts for a majority of CRC cases, with polypectomy (local resection of polyps) a standard treatment [74, 105]. A smaller percentage of CRC cases have a history of ulcerative colitis (UC), one of two major types of inflammatory bowel disease, which is linked to increased risk for CRC [94, 98]. Often, the end-treatment for UC patients is curative colectomy, yet this treatment is deferred until deemed necessary due to the presence of malignancy [62, 105]. Studies have shown that in UC patients there is still a distinction between spontaneous tumors, which can be resected via polypectomy with limited risk of recurrence, and colitis-associated tumors require curative colectomy [74, 105].

Various translational imaging modalities have been applied to the task of distinguishing between spontaneous tumors (adenoma-like mass or ALM) and colitis-associated tumors (dysplasia-associated lesion/mass or DALM) [74]. Endoscopic systems capable of *in vivo*

---

[3] Full manuscript available as Chapter V

imaging of colorectal epithelium include miniaturized confocal systems, such as the Cellvizio ®

Endomicroscopy System [112], and investigational multiphoton systems. Benefits of

multiphoton imaging, miniaturized for endoscopic applications, include label-free imaging (no

need for contrast agents) and the ability of acquiring data of both functional (autofluorescence)

and structural (second harmonic generation) biomarkers [113, 114]. As previously described, in

early cancer development, crypt structures become non-homogenous in size and shape, but the

use of second harmonic generation (SHG) imaging of crypt morphology, via collagen structures,

has not been quantitatively investigated.

Objective: Increasing the ability to distinguish between spontaneous (ALM) and colitis-

associated (DALM) tumors in UC patients could guide clinicians in appropriate treatment.

Emergence of multiphoton endoscopic systems allow for combination of functional and

structural data to improve detection and diagnosis of ALM and DALM regions in UC patients,

and a quantitative study of structural/morphological SHG data in these tumor models had not

been documented. SHG image features could serve as complementary data during multiphoton

microendoscopic imaging, and provide insight on collagen changes during crypt deformation,

which could serve a translatable measure towards detection and distinction of lesions in UC

patients.

Aim 3: Determine utility of SHG imaging in investigation of morphological changes in murine

colonic crypt structure in spontaneous and colitis-associated tumor progression. We used SHG

imaging in murine CRC models to analyze data on structural changes in cryptal collagen that

could be used as indicators of disease.

Sub-aim 1: Quantitative comparison of morphological image features in ALM and DALM

murine models. We used SHG imaging to acquire and quantify data on crypt size, shape, and

distribution in ALM and DALM murine models, to determine feasibility of using SHG imaging as a complementary source of data using miniaturized multiphoton systems. We sought to determine which image features held the most potential for distinguishing between ALM and DALM regions.

Sub-aim 2: Quantitative comparison of morphological image features in early and late time points of tumor development. We compared SHG image features in early and late time points in both ALM and DALM murine tumor development, to determine the potential of SHG imaging in assisting early detection of CRC.

Results: Our results showed that mean and variance of nearest neighbor (distance between crypts) and circularity were potential image features for SHG modalities in distinguishing between Control, ALM, and DALM regions in murine models. Control crypts had smaller average distance to the nearest neighbor compared to late-stage ALM and early-stage DALM development, as well as more homogeneous distances between crypts (variance). Preliminary results showed promise in the nearest neighbor image feature (mean and variance) serving as a morphological marker for distinguishing between early and late-stage DALM time points in our murine tumor models. Images of late-stage DALM crypts had lower average nearest neighbors compared to early-stage DALM.

Significance: Miniaturized multiphoton imaging systems have been used to qualitatively and quantitatively study functional data acquired via fluorescence channels (e.g. redox ratios and cellular metabolic response), and studies on collagen fiber density and pattern using SHG channels in various cancers have been documented [113, 114, 123]. Our quantified SHG image features, specifically nearest neighbor, showed differences in crypt distribution in ALM and DALM murine models. This could guide future multiphoton studies of these murine models, such as *in vivo* studies to acquire both autofluorescence and SHG data to more thoroughly

understand crypt morphological changes in spontaneous versus colitis-associated tumors.

Automated quantification of SHG image features, as a complementary modality during

endoscopic multiphoton imaging, could potentially contribute to more accurate screening and

diagnosis of suspicious lesions and polyps during surveillance of high-risk UC patients.

References

[1] D. H. Alpers, A. N. Kalloo, N. Kaplowitz, C. Owyang and D. W. Powell, *Textbook of Gastroenterology.* John Wiley & Sons, 2011.

[2] S. Noble, *Clinical Textbook of Dental Hygiene and Therapy.* John Wiley & Sons, 2012.

[3] U. S. National Institutes of Health, National Cancer Institute. "SEER Training Modules, *Epithelial Tissue*," 09/30/2018. https://training.seer.cancer.gov/anatomy/cells_tissues_membranes/tissues/epithelial.html.

[4] World Health Organization, *Manual of Basic Techniques for a Health Laboratory.* World Health Organization, 2003.

[5] H. Ida-Yonemochi, S. Maruyama, T. Kobayashi, M. Yamazaki, J. Cheng and T. Saku, "Loss of keratin 13 in oral carcinoma in situ: a comparative study of protein and gene expression levels using paraffin sections," *Modern Pathology,* vol. 25, *(6),* pp. 784, 2012.

[6] H. Yokota, A. Tsuzuki, Y. Shimada, A. Imai, D. Utsumi, T. Tsukahara, M. Matsumoto, K. Amagase, K. Iwata, A. Nakamura, C. Yabe-Nishimura and S. Kato, "NOX1/NADPH Oxidase Expressed in Colonic Macrophages Contributes to the Pathogenesis of Colonic Inflammation in Trinitrobenzene Sulfonic Acid-Induced Murine Colitis," *J. Pharmacol. Exp. Ther.,* vol. 360, *(1),* pp. 192-200, Jan, 2017.

[7] Audrey Rousseau and Cécile Badoual. "Head and Neck: Squamous cell carcinoma: an overview," October/2018. http://atlasgeneticsoncology.org/Tumors/HeadNeckSCCID5078.html.

[8] R. R. Pascal, G. I. Kaye and N. Lane, "Colonic pericryptal fibroblast sheath: replication, migration, and cytodifferentiation of a mesenchymal cell system in adult tissue: I. Autoradiographic studies of normal rabbit colon," *Gastroenterology,* vol. 54, *(5),* pp. 835-851, 1968.

[9] J. W. Werning, *Oral Cancer: Diagnosis, Management, and Rehabilitation.* Thieme Medical Publishers New York, 2007.

[10] National Collaborating Centre for Cancer (UK), Nov, 2011.

[11] C. Kozlowski, S. Jeet, J. Beyer, S. Guerrero, J. Lesch, X. Wang, J. Devoss and L. Diehl, "An entirely automated method to score DSS-induced colitis in mice by digital image analysis of pathology slides," Dis. Model. Mech., vol. 6, (3), pp. 855-865, May, 2013.

[12] T. Takayama, S. Katsuki, Y. Takahashi, M. Ohi, S. Nojiri, S. Sakamaki, J. Kato, K. Kogawa, H. Miyake and Y. Niitsu, "Aberrant crypt foci of the colon as precursors of adenoma and cancer," N. Engl. J. Med., vol. 339, (18), pp. 1277-1284, 1998.

[13] The Editors of Encyclopaedia Britannica. "Anus," https://www.britannica.com/science/anus.

[14] P. R. Nambiar, M. Nakanishi, R. Gupta, E. Cheung, A. Firouzi, X. J. Ma, C. Flynn, M. Dong, K. Guda, J. Levine, R. Raja, L. Achenie and D. W. Rosenberg, "Genetic signatures of high- and low-risk aberrant crypt foci in a mouse model of sporadic colon cancer," Cancer Res., vol. 64, (18), pp. 6394-6401, Sep 15, 2004.

[15] D. Solomon, D. Davey, R. Kurman, A. Moriarty, D. O'connor, M. Prey, S. Raab, M. Sherman, D. Wilbur and T. Wright Jr, "The 2001 Bethesda System: terminology for reporting results of cervical cytology," Jama, vol. 287, (16), pp. 2114-2119, 2002.

[16] T. M. Darragh, N. Jay, B. A. Tupkelewicz, C. J. Hogeboom, E. A. Holly and J. M. Palefsky, "Comparison of conventional cytologic smears and ThinPrep preparations from the anal canal," Acta Cytol., vol. 41, (4), pp. 1167-1170, Jul-Aug, 1997.

[17] F. M. Brown, "Urine cytology: is it still the gold standard for screening?" Urol. Clin. North Am., vol. 27, (1), pp. 25-37, 2000.

[18] J. Yang, V. Schnadig, R. Logrono and P. G. Wasserman, "Fine-needle aspiration of thyroid nodules: a study of 4703 patients with histologic and clinical correlations," Cancer Cytopathology, vol. 111, (5), pp. 306-315, 2007.

[19] R. Mehrotra, "The role of cytology in oral lesions: a review of recent improvements," Diagn. Cytopathol., vol. 40, (1), pp. 73-83, 2012.

[20] National Institute of Health. "NIH Glossary of Terms," https://www.nibib.nih.gov/science-education/glossary#g-43131.

[21] W. Fong, "Handbook of MRI pulse sequences," Med. Phys., vol. 32, (5), pp. 1452-1452, 2005.

[22] E. Whaites and N. Drage, Essentials of Dental Radiography and Radiology. Elsevier Health Sciences, 2013.

[23] M. Hoheisel, "Review of medical imaging with emphasis on X-ray detectors," Nuclear Instruments and Methods in Physics Research Section A: Accelerators, Spectrometers, Detectors and Associated Equipment, vol. 563, (1), pp. 215-224, 2006.

[24] J. C. Hebden, S. R. Arridge and D. T. Delpy, "Optical imaging in medicine: I. Experimental techniques," Physics in Medicine & Biology, vol. 42, (5), pp. 825, 1997.

[25] D. Hart and B. Wall, Radiation Exposure of the UK Population from Medical and Dental X-Ray Examinations. NRPB Chilton, UK, 2002.

[26] W. Bogdanich and J. McGinty, "Radiation worries for children in dentists' chairs," The New York Times, vol. 22, 2010.

[27] F. A. Mettler Jr, B. R. Thomadsen, M. Bhargavan, D. B. Gilley, J. E. Gray, J. A. Lipoti, J. McCrohan, T. T. Yoshizumi and M. Mahesh, "Medical radiation exposure in the U.S. in 2006: preliminary results," Health Phys., vol. 95, (5), pp. 502-507, Nov, 2008.

[28] J. Gallo and Y. Wijting, "Low Level Laser Therapy: Clinical Mentoring Series," Gulf Breeze: FL: CIAO Publishing, 2006.

[29] S. Sershen, S. Westcott, N. Halas and J. West, "Temperature-sensitive polymer–nanoshell composites for photothermally modulated drug delivery," Journal of Biomedical Materials Research Part A, vol. 51, (3), pp. 293-298, 2000.

[30] T. M. Allen and P. R. Cullis, "Drug delivery systems: entering the mainstream," Science, vol. 303, (5665), pp. 1818-1822, Mar 19, 2004.

[31] S. Eichmüller, P. A. Stevenson and R. Paus, "A new method for double immunolabelling with primary antibodies from identical species," J. Immunol. Methods, vol. 190, (2), pp. 255-265, 1996.

[32] D. Y. Mason, K. Micklem and M. Jones, "Double immunofluorescence labelling of routinely processed paraffin sections," J. Pathol., vol. 191, (4), pp. 452-461, 2000.

[33] X. Mo, T. Wu, B. Sun and H. EI-Hamshary, "Nanofiber composites in tendon tissue engineering," in Nanofiber Composites for Biomedical ApplicationsAnonymous Elsevier, 2017, pp. 345-367.

[34] Y. Hoshi, "Functional near-infrared optical imaging: Utility and limitations in human brain mapping," Psychophysiology, vol. 40, (4), pp. 511-520, 2003.

[35] R. Sepehr, K. Staniszewski, S. Maleki, M. Ranji, E. R. Jacobs and S. Audi, "Optical imaging of tissue mitochondrial redox state in intact rat lungs in two models of pulmonary oxidative stress," J. Biomed. Opt., vol. 17, (4), pp. 046010, 2012.

[36] F. Helmchen and W. Denk, "Deep tissue two-photon microscopy," Nature Methods, vol. 2, (12), pp. 932, 2005.

[37] J. J. Barcia, "The Giemsa stain: its history and applications," International Journal of Surgical Pathology, vol. 15, (3), pp. 292-296, 2007.

[38] J. M. Dixon, M. Taniguchi and J. S. Lindsey, "PhotochemCAD 2: a refined program with accompanying spectral databases for photochemical calculations," Photochem. Photobiol., vol. 81, (1), pp. 212-213, 2005.

[39] P. T. So, C. Y. Dong, B. R. Masters and K. M. Berland, "Two-photon excitation fluorescence microscopy," Annu. Rev. Biomed. Eng., vol. 2, (1), pp. 399-429, 2000.

[40] P. Campagnola, "Second harmonic generation imaging microscopy: applications to diseases diagnostics," ACS Publications, 2011.

[41] P. Friedl, K. Wolf, G. Harms and U. H. von Andrian, "Biological second and third harmonic generation microscopy," Current Protocols in Cell Biology, vol. 34, (1), pp. 4.15. 1-4.15. 21, 2007.

[42] S. Warnakulasuriya, "Global epidemiology of oral and oropharyngeal cancer," Oral Oncol., vol. 45, (4-5), pp. 309-316, 2009.

[43] J. V. Bagan and C. Scully, "Recent advances in Oral Oncology 2007: epidemiology, aetiopathogenesis, diagnosis and prognostication," Oral Oncol., vol. 44, (2), pp. 103-108, 2008.

[44] S. V. K. Rao, G. Mejia, K. Roberts-Thomson and R. Logan, "Epidemiology of oral cancer in Asia in the past decade-an update (2000-2012)," Asian Pacific Journal of Cancer Prevention, vol. 14, (10), pp. 5567-5577, 2013.

[45] A. Wright and M. Shear, "Epithelial dysplasia immediately adjacent to oral squamous cell carcinomas," Journal of Oral Pathology & Medicine, vol. 14, (7), pp. 559-564, 1985.

[46] H. Lumerman, P. Freedman and S. Kerpel, "Oral epithelial dysplasia and the development of invasive squamous cell carcinoma," Oral Surgery, Oral Medicine, Oral Pathology, Oral Radiology and Endodontics, vol. 79, (3), pp. 321-329, 1995.

[47] B. W. Neville and T. A. Day, "Oral cancer and precancerous lesions," CA: A Cancer Journal for Clinicians, vol. 52, (4), pp. 195-215, 2002.

[48] R. Akhter, N. M. M. Hassan, J. Aida, S. Takinami and M. Morita, "Relationship between betel quid additives and established periodontitis among Bangladeshi subjects," J. Clin. Periodontol., vol. 35, (1), pp. 9-15, 2008.

[49] M. C. Downer, D. R. Moles, S. Palmer and P. M. Speight, "A systematic review of measures of effectiveness in screening for oral cancer and precancer," Oral Oncol., vol. 42, (6), pp. 551-560, 2006.

[50] R. S. Wesley, V. R. Kutty, B. Matthew, R. Sankaranarayanan and M. K. Nair, "Economic comparison of two strategies of oral cancer screening," Health Policy Plan., vol. 7, (3), pp. 284-289, 1992.

[51] B. Majer, B. Laky, S. Knasmüller and F. Kassie, "Use of the micronucleus assay with exfoliated epithelial cells as a biomarker for monitoring individuals at elevated risk of genetic damage and in chemoprevention trials," Mutation Research/Reviews in Mutation Research, vol. 489, (2), pp. 147-172, 2001.

[52] O. Kujan, M. Desai, A. Sargent, A. Bailey, A. Turner and P. Sloan, "Potential applications of oral brush cytology with liquid-based technology: results from a cohort of normal oral mucosa," Oral Oncol., vol. 42, (8), pp. 810-818, 2006.

[53] J. J. Sciubba and US Collaborative OralCDx Study Group, "Improving detection of precancerous and cancerous oral lesions: computer-assisted analysis of the oral brush biopsy," J. Am. Dent. Assoc., vol. 130, (10), pp. 1445-1457, 1999.

[54] D. C. Christian, "Computer-assisted analysis of oral brush biopsies at an oral cancer screening program," J. Am. Dent. Assoc., vol. 133, (3), pp. 357-362, 2002.

[55] A. Nersesyan, M. Kundi, K. Atefie, R. Schulte-Hermann and S. Knasmuller, "Effect of staining procedures on the results of micronucleus assays with exfoliated oral mucosa cells," Cancer Epidemiol. Biomarkers Prev., vol. 15, (10), pp. 1835-1840, Oct, 2006.

[56] F. Traganos and Z. Darzynkiewicz, "Lysosomal proton pump activity: supravital cell staining with acridine orange differentiates leukocyte subpopulations," Methods Cell Biol., vol. 41, pp. 185-195, 1994.

[57] A. Pliss, A. N. Kuzmin, A. V. Kachynski and P. N. Prasad, "Biophotonic probing of macromolecular transformations during apoptosis," Proc. Natl. Acad. Sci. U. S. A., vol. 107, (29), pp. 12771-12776, Jul 20, 2010.

[58] S. P. Reddy, P. Ramani and P. Nainani, "Confocal microscopy and exfoliative cytology," J. Oral Maxillofac. Pathol., vol. 17, (2), pp. 217-221, May, 2013.

[59] M. Wainwright, "Acridine—a neglected antibacterial chromophore," J. Antimicrob. Chemother., vol. 47, (1), pp. 1-13, 2001.

[60] J. D. Kawedia, Y. Zhang, A. L. Myers, R. R. Richards-Kortum, M. A. Kramer, A. M. Gillenwater and K. S. Culotta, "Physical and chemical stability of proflavine contrast agent solutions for early detection of oral cancer," Journal of Oncology Pharmacy Practice, vol. 22, (1), pp. 21-25, 2016.

[61] A. Noone, N. Howlader, M. Krapcho, D. Miller, A. Brest, M. Yu, J. Ruhl, Z. Tatalovich, A. Mariotto and D. Lewis, SEER Cancer Statistics Review, 1975-2015, National Cancer Institute.Bethesda, MD, 2018.

[62] P. Munkholm, "The incidence and prevalence of colorectal cancer in inflammatory bowel disease," Aliment. Pharmacol. Ther., vol. 18, (s2), pp. 1-5, 2003.

[63] F. Kastrinos and S. Syngal, "Inherited colorectal cancer syndromes," Cancer J., vol. 17, (6), pp. 405-415, Nov-Dec, 2011.

[64] L. Bujanda, A. Cosme, I. Gil and J. I. Arenas-Mirave, "Malignant colorectal polyps," World J. Gastroenterol., vol. 16, (25), pp. 3103-3111, Jul 7, 2010.

[65] S. Kudo and H. Kashida, "Flat and depressed lesions of the colorectum," Clinical Gastroenterology and Hepatology, vol. 3, (7), pp. S33-S36, 2005.

[66] M. Fleming, S. Ravula, S. F. Tatishchev and H. L. Wang, "Colorectal carcinoma: Pathologic aspects," Journal of Gastrointestinal Oncology, vol. 3, (3), pp. 153, 2012.

[67] S. H. Itzkowitz and D. H. Present, "Consensus conference: colorectal cancer screening and surveillance in inflammatory bowel disease," Inflamm. Bowel Dis., vol. 11, (3), pp. 314-321, 2005.

[68] R. L. Siegel, K. D. Miller, S. A. Fedewa, D. J. Ahnen, R. G. Meester, A. Barzi and A. Jemal, "Colorectal cancer statistics, 2017," CA: A Cancer Journal for Clinicians, vol. 67, (3), pp. 177-193, 2017.

[69] P. J. Guillou, P. Quirke, H. Thorpe, J. Walker, D. G. Jayne, A. M. Smith, R. M. Heath, J. M. Brown and MRC CLASICC trial group, "Short-term endpoints of conventional versus laparoscopic-assisted surgery in patients with colorectal cancer (MRC CLASICC trial): multicentre, randomised controlled trial," The Lancet, vol. 365, (9472), pp. 1718-1726, 2005.

[70] R. M. Goldberg, T. R. Fleming, C. M. Tangen, C. G. Moertel, J. S. Macdonald, D. G. Haller and J. A. Laurie, "Surgery for recurrent colon cancer: strategies for identifying resectable recurrence and success rates after resection," Ann. Intern. Med., vol. 129, (1), pp. 27-35, 1998.

[71] Y. L. Cheng, T. Rees and J. Wright, "A review of research on salivary biomarkers for oral cancer detection," Clinical and Translational Medicine, vol. 3, (1), pp. 3, 2014.

[72] K. W. Smith, J. A. Kortenbach, C. R. Slater, A. I. Mazzeo, T. C. Slack Jr and T. O. Bales, "Endoscopic robotic surgical tools and methods
,", 1997.

[73] R. Kiesslich, M. Goetz, K. Lammersdorf, C. Schneider, J. Burg, M. Stolte, M. Vieth, B. Nafe, P. R. Galle and M. F. Neurath, "Chromoscopy-guided endomicroscopy increases the diagnostic yield of intraepithelial neoplasia in ulcerative colitis," Gastroenterology, vol. 132, (3), pp. 874-882, 2007.

[74] H. Neumann, M. Vieth, C. Langner, M. F. Neurath and J. Mudter, "Cancer risk in IBD: how to diagnose and how to manage DALM and ALM," World J. Gastroenterol., vol. 17, (27), pp. 3184-3191, Jul 21, 2011.

[75] H. Neumann, L. Fry, M. Bellutti, P. Malfertheiner and K. Mönkemüller, "Double-balloon enteroscopy-assisted virtual chromoendoscopy for small-bowel disorders–a case series," Endoscopy, vol. 41, (05), pp. 468-471, 2009.

[76] H. Neumann, R. Kiesslich, M. B. Wallace and M. F. Neurath, "Confocal laser endomicroscopy: technical advances and clinical applications," Gastroenterology, vol. 139, (2), pp. 388-92, 392.e1-2, Aug, 2010.

[77] A. Ishijima, S. Mondrik, R. A. Schwarz, N. Vigneswaran, A. M. Gillenwater and R. Richards-Kortum, "Automated frame selection process for analyzing high resolution microendoscope images," in SPIE Translational Biophotonics, 2014, pp. 91551M-91551M-4.

[78] P. M. Lane, S. Lam, A. McWilliams, M. W. Anderson and C. E. MacAulay, "Confocal fluorescence microendoscopy of bronchial epithelium," J. Biomed. Opt., vol. 14, (2), pp. 024008-024008-10, 2009.

[79] P. M. Vila, C. W. Park, M. C. Pierce, G. H. Goldstein, L. Levy, V. V. Gurudutt, A. D. Polydorides, J. H. Godbold, M. S. Teng and E. M. Genden, "Discrimination of benign and neoplastic mucosa with a high-resolution microendoscope (HRME) in head and neck cancer," Annals of Surgical Oncology, vol. 19, (11), pp. 3534-3539, 2012.

[80] M. Kobayashi, H. Tajiri, E. Seike, M. Shitaya, S. Tounou, M. Mine and K. Oba, "Detection of early gastric cancer by a real-time autofluorescence imaging system," Cancer Lett., vol. 165, (2), pp. 155-159, 2001.

[81] H. Machida, Y. Sano, Y. Hamamoto, M. Muto, T. Kozu, H. Tajiri and S. Yoshida, "Narrow-band imaging in the diagnosis of colorectal mucosal lesions: a pilot study," Endoscopy, vol. 36, (12), pp. 1094-1098, Dec, 2004.

[82] M. Pierce, D. Yu and R. Richards-Kortum, "High-resolution fiber-optic microendoscopy for in situ cellular imaging," J. Vis. Exp., vol. (47). pii: 2306. doi, (47), pp. 10.3791/2306, Jan 11, 2011.

[83] H. Shin, M. C. Pierce, D. Lee, H. Ra, O. Solgaard and R. Richards-Kortum, "Fiber-optic confocal microscope using a MEMS scanner and miniature objective lens," Optics Express, vol. 15, (15), pp. 9113-9122, 2007.

[84] T. J. Muldoon, N. Thekkek, D. Roblyer, D. Maru, N. Harpaz, J. Potack, S. Anandasabapathy and R. Richards-Kortum, "Evaluation of quantitative image analysis criteria for the high-resolution microendoscopic detection of neoplasia in Barrett's esophagus," J. Biomed. Opt., vol. 15, (2), pp. 026027-026027-7, 2010.

[85] T. J. Muldoon, D. Roblyer, M. D. Williams, V. M. Stepanek, R. Richards–Kortum and A. M. Gillenwater, "Noninvasive imaging of oral neoplasia with a high-resolution fiber-optic microendoscope," Head Neck, vol. 34, (3), pp. 305-312, 2012.

[86] N. D. Parikh, D. Perl, M. H. Lee, B. Shah, Y. Young, S. S. Chang, R. Shukla, A. D. Polydorides, E. Moshier and J. Godbold, "In vivo diagnostic accuracy of high-resolution microendoscopy in differentiating neoplastic from non-neoplastic colorectal polyps: a prospective study," Am. J. Gastroenterol., vol. 109, (1), pp. 68-75, 2014.

[87] S. P. Prieto, K. K. Lai, J. A. Laryea, J. S. Mizell, W. C. Mustain and T. J. Muldoon, "Fluorescein as a topical fluorescent contrast agent for quantitative microendoscopic inspection of colorectal epithelium," Biomedical Optics Express, vol. 8, (4), pp. 2324-2338, 2017.

[88] K. W. Jasperson, T. M. Tuohy, D. W. Neklason and R. W. Burt, "Hereditary and familial colon cancer," Gastroenterology, vol. 138, (6), pp. 2044-2058, 2010.

[89] N. D. Parikh, D. Perl, M. H. Lee, S. S. Chang, A. D. Polydorides, E. Moshier, J. Godbold, E. Zhou, J. Mitcham and R. Richards-Kortum, "In vivo classification of colorectal neoplasia using high-resolution microendoscopy: Improvement with experience," J. Gastroenterol. Hepatol., vol. 30, (7), pp. 1155-1160, 2015.

[90] J. A. Swets, "Measuring the accuracy of diagnostic systems," Science, vol. 240, (4857), pp. 1285-1293, Jun 3, 1988.

[91] A. J. Walsh and M. C. Skala, "An automated image processing routine for segmentation of cell cytoplasms in high-resolution autofluorescence images," in Multiphoton Microscopy in the Biomedical Sciences XIV, 2014, pp. 89481M.

[92] J. M. Street, A. C. P. Souza, A. Alvarez-Prats, T. Horino, X. Hu, P. S. Yuen and R. A. Star, "Automated quantification of renal fibrosis with Sirius Red and polarization contrast microscopy," Physiological Reports, vol. 2, (7), 2014.

[93] Z. Liu, D. Pouli, D. Sood, A. Sundarakrishnan, C. K. H. Mingalone, L. M. Arendt, C. Alonzo, K. P. Quinn, C. Kuperwasser and L. Zeng, "Automated quantification of three-dimensional organization of fiber-like structures in biological tissues," Biomaterials, vol. 116, pp. 34-47, 2017.

[94] N. A. Molodecky, I. S. Soon, D. M. Rabi, W. A. Ghali, M. Ferris, G. Chernoff, E. I. Benchimol, R. Panaccione, S. Ghosh, H. W. Barkema and G. G. Kaplan, "Increasing incidence and prevalence of the inflammatory bowel diseases with time, based on systematic review," Gastroenterology, vol. 142, (1), pp. 46-54, Jan, 2012.

[95] D. K. Podolsky, "Inflammatory bowel disease," N. Engl. J. Med., vol. 325, (13), pp. 928-937, 1991.

[96] W. J. Hogan, G. T. Hensley and J. E. Geenen, "Endoscopic evaluation of inflammatory bowel disease," Med. Clin. North Am., vol. 64, (6), pp. 1083-1102, Nov, 1980.

[97] H. Goldman, "Significance and detection of dysplasia in chronic colitis," Cancer: Interdisciplinary International Journal of the American Cancer Society, vol. 78, (11), pp. 2261-2263, 1996.

[98] S. N. Gyde, P. Prior, R. N. Allan, A. Stevens, D. P. Jewell, S. C. Truelove, R. Lofberg, O. Brostrom and G. Hellers, "Colorectal cancer in ulcerative colitis: a cohort study of primary referrals from three centres," Gut, vol. 29, (2), pp. 206-217, Feb, 1988.

[99] A. Ekbom, C. Helmick, M. Zack and H. Adami, "Ulcerative colitis and colorectal cancer: a population-based study," N. Engl. J. Med., vol. 323, (18), pp. 1228-1233, 1990.

[100] C. D. Gillen, R. S. Walmsley, P. Prior, H. A. Andrews and R. N. Allan, "Ulcerative colitis and Crohn's disease: a comparison of the colorectal cancer risk in extensive colitis," Gut, vol. 35, (11), pp. 1590-1592, Nov, 1994.

[101] A. J. Greenstein, D. B. Sachar, H. Smith, H. D. Janowitz and A. H. Aufses Jr, "A comparison of cancer risk in Crohn's disease and ulcerative colitis," Cancer, vol. 48, (12), pp. 2742-2745, 1981.

[102] C. Canavan, K. Abrams and J. Mayberry, "Meta-analysis: colorectal and small bowel cancer risk in patients with Crohn's disease," Aliment. Pharmacol. Ther., vol. 23, (8), pp. 1097-1104, 2006.

[103] I. Atreya, R. Atreya and M. Neurath, "NF-κB in inflammatory bowel disease," J. Intern. Med., vol. 263, (6), pp. 591-596, 2008.

[104] A. C. Ford, J. Achkar, K. J. Khan, S. V. Kane, N. J. Talley, J. K. Marshall and P. Moayyedi, "Efficacy of 5-aminosalicylates in ulcerative colitis: systematic review and meta-analysis," Am. J. Gastroenterol., vol. 106, (4), pp. 601, 2011.

[105] T. Ullman, R. Odze and F. A. Farraye, "Diagnosis and management of dysplasia in patients with ulcerative colitis and Crohn's disease of the colon," Inflamm. Bowel Dis., vol. 15, (4), pp. 630-638, 2008.

[106] D. C. Rubin, A. Shaker and M. S. Levin, "Chronic intestinal inflammation: inflammatory bowel disease and colitis-associated colon cancer," Frontiers in Immunology, vol. 3, pp. 107, 2012.

[107] C. J. Karvellas, R. N. Fedorak, J. Hanson and C. K. Wong, "Increased risk of colorectal cancer in ulcerative colitis patients diagnosed after 40 years of age," Canadian Journal of Gastroenterology and Hepatology, vol. 21, (7), pp. 443-446, 2007.

[108] B. Kim, J. L. Barnett, C. G. Kleer and H. D. Appelman, "Endoscopic and histological patchiness in treated ulcerative colitis," Am. J. Gastroenterol., vol. 94, (11), pp. 3258-3262, 1999.

[109] M. D. Rutter, B. P. Saunders, K. H. Wilkinson, M. A. Kamm, C. B. Williams and A. Forbes, "Most dysplasia in ulcerative colitis is visible at colonoscopy," Gastrointest. Endosc., vol. 60, (3), pp. 334-339, 2004.

[110] F. Shanahan, W. Weinstein and C. Bernstein, "Are we telling patients the truth about surveillance colonoscopy in ulcerative colitis?" The Lancet, vol. 343, (8889), pp. 71-74, 1994.

[111] D. P. Hurlstone, S. S. Cross, I. Adam, A. J. Shorthouse, S. Brown, D. S. Sanders and A. J. Lobo, "A prospective clinicopathological and endoscopic evaluation of flat and depressed colorectal lesions in the United Kingdom," Am. J. Gastroenterol., vol. 98, (11), pp. 2543-2549, 2003.

[112] G. D. De Palma, S. Staibano, S. Siciliano, F. Maione, M. Siano, D. Esposito and G. Persico, "In-vivo characterization of DALM in ulcerative colitis with high-resolution probe-based confocal laser endomicroscopy," World J. Gastroenterol., vol. 17, (5), pp. 677-680, Feb 7, 2011.

[113] Y. Zhang, M. L. Akins, K. Murari, J. Xi, M. J. Li, K. Luby-Phelps, M. Mahendroo and X. Li, "A compact fiber-optic SHG scanning endomicroscope and its application to visualize cervical remodeling during pregnancy," Proc. Natl. Acad. Sci. U. S. A., vol. 109, (32), pp. 12878-12883, Aug 7, 2012.

[114] D. R. Rivera, C. M. Brown, D. G. Ouzounov, I. Pavlova, D. Kobat, W. W. Webb and C. Xu, "Compact and flexible raster scanning multiphoton endoscope capable of imaging unstained tissue," Proc. Natl. Acad. Sci. U. S. A., vol. 108, (43), pp. 17598-17603, Oct 25, 2011.

[115] I. Freund, M. Deutsch and A. Sprecher, "Connective tissue polarity. Optical second-harmonic microscopy, crossed-beam summation, and small-angle scattering in rat-tail tendon," Biophys. J., vol. 50, (4), pp. 693-712, Oct, 1986.

[116] J. S. Bredfeldt, Y. Liu, C. A. Pehlke, M. W. Conklin, J. M. Szulczewski, D. R. Inman, P. J. Keely, R. D. Nowak, T. R. Mackie and K. W. Eliceiri, "Computational segmentation of collagen fibers from second-harmonic generation images of breast cancer," J. Biomed. Opt., vol. 19, (1), pp. 016007, 2014.

[117] L. Pauling and R. B. Corey, "The structure of fibrous proteins of the collagen-gelatin group," Proc. Natl. Acad. Sci. U. S. A., vol. 37, (5), pp. 272-281, May, 1951.

[118] S. Zhuo, J. Chen, G. Wu, S. Xie, L. Zheng, X. Jiang and X. Zhu, "Quantitatively linking collagen alteration and epithelial tumor progression by second harmonic generation microscopy," Appl. Phys. Lett., vol. 96, (21), pp. 213704, 2010.

[119] S. Wang, J. Chen, Y. Yang, W. Jiang, C. Feng, G. Guan, S. Zhuo and Z. Chen, "Assessment of tumor invasion depth in colorectal carcinoma using multiphoton microscopy," IEEE Photonics Journal, vol. 7, (2), pp. 1-8, 2015.

[120] F. Helmchen, M. S. Fee, D. W. Tank and W. Denk, "A miniature head-mounted two-photon microscope: high-resolution brain imaging in freely moving animals," Neuron, vol. 31, (6), pp. 903-912, 2001.

[121] Y. Wu, J. Xi, M. J. Cobb and X. Li, "Scanning fiber-optic nonlinear endomicroscopy with miniature aspherical compound lens and multimode fiber collector," Opt. Lett., vol. 34, (7), pp. 953-955, 2009.

[122] H. Bao, A. Boussioutas, R. Jeremy, S. Russell and M. Gu, "Second harmonic generation imaging via nonlinear endomicroscopy," Optics Express, vol. 18, (2), pp. 1255-1260, 2010.

[123] M. Bianchi, J. Adur, S. Ruff, M. Izaguirre, H. Carvalho, C. Cesar and V. Casco, "Analysis of the orientation of collagen fibers as a tool for the early detection of colorectal cancer," in VI Latin American Congress on Biomedical Engineering CLAIB 2014, Paraná, Argentina 29, 30 & 31 October 2014, 2015, pp. 365-368.

[124] G. D. De Palma, "Confocal laser endomicroscopy in the "in vivo" histological diagnosis of the gastrointestinal tract," World J. Gastroenterol., vol. 15, (46), pp. 5770-5775, Dec 14, 2009.

Chapter II: Proflavine Hemisulfate as a Fluorescent Contrast Agent for Point-of-Care Cytology [1]

1. Introduction

Cytology is defined as the study of cells on a microscopic scale with a focus on morphology and structural distinctions [2]. Considering the many cytological procedures that depend on visual diagnosis, and distinguishing of structural features such as nuclear size, nuclear to cytoplasmic ratios, and cytoplasmic features, the field depends significantly on contrast-enhancing agents. Clinical cytology is typically performed by sample collection, fixation, staining, and visual inspection by a trained pathologist. Cytology specimens may include peripheral blood smears, fine needle aspirations (FNA), bronchial alveolar lavages (BAL), and oral as well as vaginal/cervical exfoliated cells. Clinical cytology provides complementary information to more conventional histopathology examination of thin tissue sections made from solid tissue, particularly when screening for cellular atypia and dysplasia [3].

Common contrast agents used for cytology include conventional hematoxylin and eosin (H&E), Giemsa, and Papanicolaou (PAP) staining [4, 5]. Fluorescent dyes are also popular contrast agents due to their high signal-to-background ratios, as well as offering the option for varying levels of specificity in targeting of molecules and/or structures. Fluorescent contrast agents do not necessarily need to be as target-specific as immunofluorescent staining. Common untargeted exogenous fluorescent stains include ethidium bromide, acridine orange, propidium iodide, and acriflavine hydrochloride / proflavine hemisulfate. Popular stains such as the fluorescent dye acridine orange are widely used in flow cytometry and cytochemistry applications which do not require the selectivity of immunofluorescence, such as the lysosome staining of living blood cells, and in distinguishing between different types of lung cells [6].

Nucleic acid probes, which do not fall under the category of target-specific dyes, despite their preferential binding to nucleic acids, are used routinely to determine the ploidy or phase of a cell, but usually require fixation and permeabilization [7-9]. A common benefit of untargeted fluorescent stains is the simplicity of the staining process, compared to the hybridization time and environmental factors, such as temperature and media, required for immunolabeling. Proflavine, an aminoacridine-derived dye similar to acridine orange, non-specifically stains cellular structures, as well as preferentially stains cell nuclei. It exhibits fluorescence with a peak excitation around 460nm and emission around 515nm, with a quantum efficiency of 0.5 [10, 11]. Proflavine can be used to rapidly stain fresh cells due to its small molecular size and amphipathic chemistry, enabling the molecule to easily pass through the lipid bilayer of the cell and nuclear membrane [12]. It has been shown to intercalate double stranded DNA, providing strong nuclear contrast [13, 14]. In addition, proflavine exhibits less prominent staining of cytoplasmic structures, which can be beneficial for cell classification, allowing for applications in cytological analysis.

Proflavine has been used clinically since 1917 [15], but its use as a cytological tool isn't widespread despite its numerous advantages. Its ability to intercalate DNA has provided many applications including anti-cancer, anti-bacterial, and anti-viral drugs [16-18]. Common research applications include endoscopy and microendoscopy imaging, modalities that benefit from contrast agents that allow for rapid topical staining of intact epithelium, where proflavine is used as a topical contrast agent for histological analysis [15, 19, 20]. There has also recently been renewed interest in proflavine for point-of-care diagnostic applications in low-resource settings due to its physical and chemical stability in solution, lasting at least 12 months under refrigeration [21].

In this paper we will demonstrate the benefits of proflavine staining in cytological samples, including rapid and preferential staining of nucleic structures such as cytosol, membrane, granules and nuclei. Proflavine's rapid staining eliminates time-consuming procedures while retaining the benefits of fluorescence imaging. We have demonstrated proflavine staining in a variety of cell types, including normal exfoliated oral squamous cells, an in vitro cultured oral squamous carcinoma cell line (Cal 27), and normal human leukocytes from whole blood. All proflavine fluorescence images were acquired using a custom-built, cost-effective and portable fluorescence microscopy platform. Automated image analysis tools were used to demonstrate the feasibility of using computer aided diagnostic approaches on proflavine-stained cytology specimens.

2. Materials and Methods

Mammalian Cell Culture

CAL 27, a squamous cell carcinoma cell line (ATCC CRL-2095, ATCC, Manassas, VA), was cultured in Dulbecco's Modified Eagle Medium (DMEM) media supplemented with 10% fetal bovine serum (ATCC, Manassas, VA) and 1% Penicillin-Streptomycin (Life Technologies, Grand Island, NY) and incubated at 37°C in 5% CO2. The cells were utilized up to passage number four. Before staining, the cells were trypsinized with 0.25% Trypsin-EDTA (Life Technologies, Grand Island, NY).

Human Cell Collection

All human cells used in this study were collected following written informed consent from healthy volunteers as part of a protocol (IRB#13-06-759) approved by the University of Arkansas Institutional Review Board.

Exfoliated oral epithelial cells were collected through an oral rinse consisting of a 30 sec rinse to remove food particles and bacteria that were discarded followed by a 90 sec collected rinse. The cell suspension was filtered through a 100μm cell strainer (Falcon, Bedford, MA) to remove mucus and washed three times by centrifuging at 200g for 5 min, decanting the supernatant, and resuspending in phosphate buffered saline (1x PBS, Sigma-Aldrich, St. Louis, MO). Whole blood was collected using a fingerstick lancet (30 Gauge Ultra-Thin Lancets, ReliOn, Bentonville, AR). The first drop was discarded [22], and approximately 20μl of blood was collected using a micropipette.

Papanicolaou Staining of Oral Epithelial Cells

A cotton swab was used to transfer exfoliated oral epithelial cells from the oral cavity to a clean slide, where it was left to dry completely. Following a conventional Papanicolaou staining procedure [23], the cells were fixed with 95% ethanol, chromatin stained using Gill Hematoxylin #1 (Millipore, Billerica, MA), blued with Scott's tap water substitute (Millipore, Billerica, MA), cytoplasmic counterstained using Modified OG-6 and Modified EA (Millipore, Billerica, MA), and cleaned with Xylene. After mounting a no.1 coverslip, the slides were imaged in brightfield using a Nikon Eclipse Ci microscope (Nikon Instruments Inc., Melville, NY) and a 60x Nikon Plan Apo VC oil immersion objective (N.A. = 1.40, Nikon Instruments Inc., Melville, NY).

Papanicolaou Staining of CAL 27 Cells

After passaging the CAL 27 cells, the cell suspension, ranging from 600,000–800,000 cells, was centrifuged at 200g for 5 min and the media removed. The cells were resuspended in 1X PBS and washed once by centrifuging at 200g for 5 min, decanting the supernatant, and resuspending in PBS. A glass slide was prepared by pipetting 10μl of the cell suspension and using the pipette tip to spread the droplet into a monolayer. The slide was dried completely and

stained following the same modified Papanicolaou staining procedure described previously. The slide was imaged in brightfield using the same Nikon microscope and 60x oil immersion objective.

Giemsa Staining of Blood Smears

A peripheral blood smear was Giemsa stained following standard methods [22]. The smear was allowed to completely dry before being fixed with methanol for a few seconds. The slide was then stained with a 10% Giemsa (Alfa Aesar, Ward Hill, MA) solution for 5–10 min. The slide was rinsed with clean water and allowed to dry before mounting a coverslip. The slides were imaged with a brightfield microscope (Nikon Eclipse Ci, Nikon Instruments Inc., Melville, NY) using a 60x oil immersion objective (60x Nikon Plan Apo VC, Nikon Instruments Inc., Melville, NY).

Proflavine Staining of Oral Epithelial Cells

The samples of exfoliated cells were washed in PBS three times and incubated in 1% albumin from bovine serum (BSA, Sigma-Aldrich, St. Louis, MO) for 5 min. The BSA was removed and the cells were stained with a solution of 0.01% (w/v) proflavine in PBS. Additionally, to collect immature oral epithelial cells, a cotton swab was used to collect normal oral cells from a volunteer. The swab was mixed in a 0.01% (w/v) proflavine solution to suspend and stain the cells. A 10μl sample of stained cells from each collection method was added to a slide and (no.1) coverslipped. The slide was imaged with our epi-illuminated fluorescence system using a 40x Nikon Plan Achromat air objective (N.A. = 0.65, Nikon Instruments Inc., Melville, NY).

Proflavine Staining of CAL 27

Passaged CAL 27 cells (up to passage number four) were centrifuged at 200g for 5 min and the media removed. The cells were washed once with PBS by centrifuging at 200g for 5 min, decanting the supernatant, and resuspending in 1% BSA for 5 min. The BSA was removed and the cells were stained with the 0.01% (w/v) proflavine solution. The slide preparation and imaging was conducted the same as previously described.

Proflavine Staining of Leukocytes

The samples of whole blood were stained at a final concentration of 0.01% (w/v) proflavine solution. The slide preparation and imaging was conducted the same as previously described.

Custom Fluorescence Imaging System

Image acquisition was also performed using a custom epi-fluorescence microscope (see Fig 1) based on a microendoscopy platform previously demonstrated [24]. This system comprises an LED illumination source at a center wavelength of 455nm (Philips, San Jose, California) providing approximately 8mW at the sample, a 475nm dichroic filter set (Chroma Technologies, Bellows Falls, VT) and a 525/40nm bandpass emission filter. The imaging system used a 40x Nikon Plan Achromat air objective (N.A. = 0.65, Nikon Instruments Inc., Melville, NY) and a 150mm achromatic doublet tube lens (Thorlabs, Newton, NJ). A Flea 3 USB camera (Point Grey Research, BC, CA) was used for imaging. The samples were placed on a set of linear translation stages (Thorlabs, Newton, NJ) for x and y axis translation. This system performs comparably to any conventional epi-fluorescence microscope equipped with a fluorescein or green fluorescent protein (GFP) filter set and monochrome camera. Images were taken with no gain, and with exposure times in the range of 100 to 150 msec. Fluorescence images were

normalized to ensure equal pixel intensity maxima in all images, in order to compensate for photobleaching and other uneven illumination artefacts. The histograms were stretched, assigning the highest pixel value to be at maximum intensity (255 for an 8-bit image) and the other pixel values were scaled accordingly to conserve the ratios.
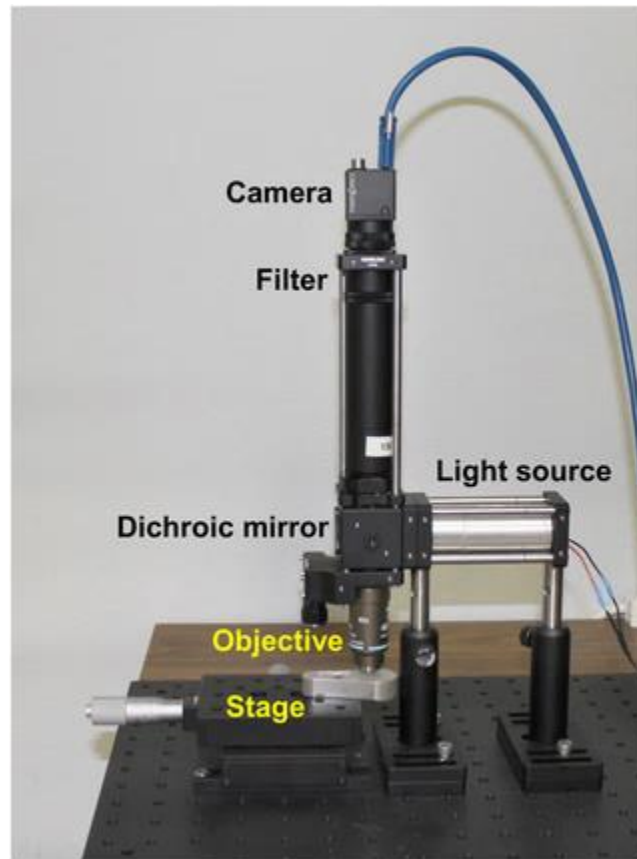
Figure 1. Custom epi-fluorescence microscopy system. Comprises a Flea 3 USB camera, 525/40nm bandpass emission filter, 475nm dichroic filter set, 455nm LED light source, 40x Nikon Plan Achromat air objective and two linear translation stages.

Manual Segmentation for Nuclear to Cytoplasmic Ratio

Images were semi-quantitatively analyzed using ImageJ [25]. Digital images acquired using our custom microscopy system were hand-segmented using ImageJ to isolate the nucleus from the cytoplasm. The boundary around the nucleus was traced using the free-hand tool, measuring the area, and repeating the process for the boundary around the entire cell (see Fig 2).

The number of pixels within each measured area (nuclear, whole cell) was tabulated. The cytoplasmic area was then calculated by subtracting the nuclear area from the whole cell. The nuclear to cytoplasmic ratios were then calculated for each cell. The mean and standard deviation values of these ratios were computed for both normal oral and Cal 27 cells.
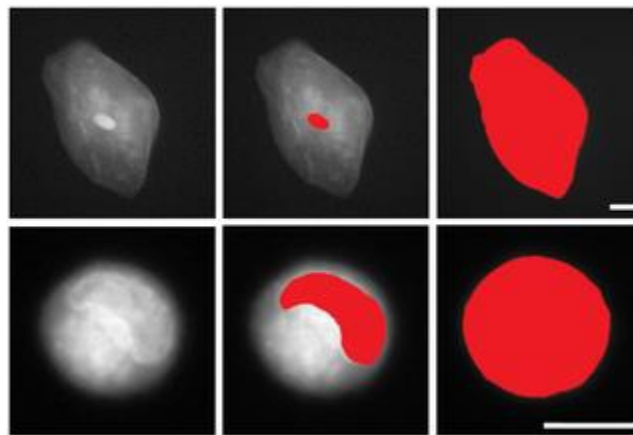
Figure 2. Illustration of manually-segmented oral epithelial cells stained with proflavine. Top row: Normal exfoliated oral epithelial cells. Bottom row: CAL 27 oral squamous carcinoma cells. Scale bars = 10μm.

Image texture features used to analyze the images included the calculated standard deviation of the pixel intensity across the entire image, as well as entropy values. Entropy is an image texture function in the MATLAB toolbox which examines the entire image for pixel intensity variation, as a measurement of heterogeneity in an image. Standard deviation and entropy of one hundred images of each type, normal exfoliated oral squamous epithelial cells and cultured Cal 27 oral squamous carcinoma cells, were computed, averaged, and tabulated. The statistical significance for each group (p values) were computed using a two tailed Student's t test.

3. Results

Comparison of Cytologic Features Seen in Papanicolaou and Proflavine Stained Oral Cells

Proflavine stains both cytosol and nuclei in oral cells, yet the two regions are still distinguishable. As seen in Fig 3, Papanicolaou stained cells are compared with similar cell types stained with proflavine. Nuclear as well as cytoplasmic shape, size, granulation (keratohyalin) and the golgi zone are distinguishable in both the colorimetric and fluorescently stained cell types (Fig 4). Note the small, well-defined nuclei in normal oral cells, which exhibit significantly brighter fluorescence than the surrounding cytoplasm. Cytoplasmic detail, such as keratohyalin granules, is also apparent. Cal 27 oral squamous carcinoma cells, by comparison exhibit very large and somewhat undefined nuclear envelopes and prominent Golgi zones. In both cases, proflavine fluorescence and Papanicolaou staining patterns are similar.
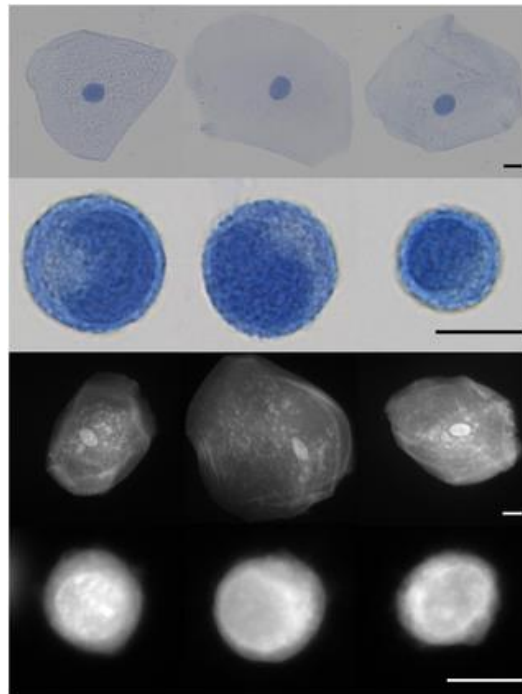
Figure 3. Visual diagnosis comparison of Papanicolaou and proflavine-stained normal oral cells and CAL 27 cell line. First row: Papanicolaou stained normal oral cells. Second row: Papanicolaou stained CAL 27 cells. Third row: Fluorescent images of proflavine stained normal oral cells. Fourth row: Fluorescent images of proflavine stained CAL 27 cells. Scale bars = 10μm.
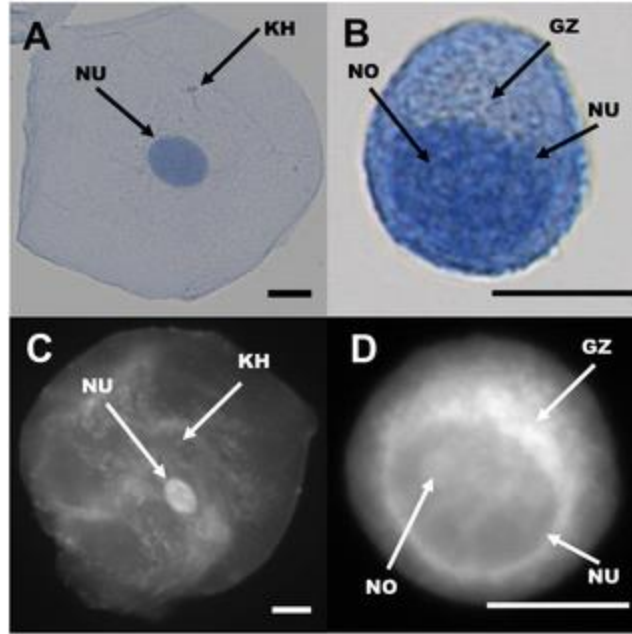
Figure 4. Comparison of cellular features seen in Papanicolaou (top row) and proflavine (bottom row) stained cells. Left column, oral squamous epithelial cells. Right column, Cal 27 squamous carcinoma cells. NU: Nucleus, NO: Nucleolus, KH: Keratohyalin granule, GZ: Golgi zone. Scale bars = 10μm.

Comparison of Cytologic Features Seen in Giemsa and Proflavine Stained Human Leukocytes

As seen in Fig 5, while Giemsa stains both erythrocytes and leukocytes, proflavine preferentially stains the nuclei-containing leukocytes. Proflavine, given its ability to intercalate DNA, prominently highlights nuclear structures within cells. Since human erythrocytes have little DNA content, there is very little proflavine signal present from these cells. While the erythrocytes are not visible with proflavine staining, the monolobar and multilobar structures within leukocytes are clearly distinguishable. Proflavine stained neutrophils exhibit classic multilobar architecture, with detectable granulation in the cytoplasm. Proflavine stained monocytes display a smooth, convoluted nuclear envelope and relatively homogeneous cytoplasm. Proflavine stained lymphocytes are easily distinguished by their characteristically

smaller size, and display a relatively heterogeneous chromatin staining pattern and scant

cytoplasmic labeling.
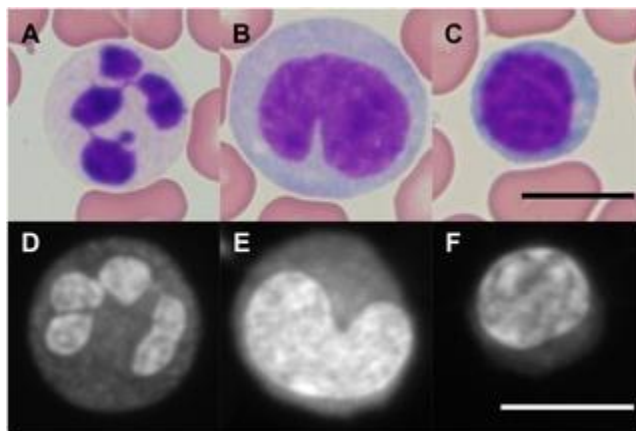
Figure 5. Giemsa (top row) and proflavine (bottom row) stained leukocytes. First row, Giemsa stained neutrophil (A), monocyte (B), lymphocyte (C). Second row, proflavine stained neutrophil (D), monocyte (E), lymphocyte (F). Images were captured at 60X. Fluorescence images were normalized as described in the Methods section. Scale bars = 10μm.

Morphology and Quantitative Image Analysis of Oral Cells

Cytology images were analyzed quantitatively to extract important metrics indicative of

cellular morphology. Both manual image metrics and automatic image texture analysis were

used. Using ImageJ, the ratio between nuclear and cytoplasmic area was computed for

comparison between normal human oral squamous cells and cultured Cal 27 oral squamous

carcinoma cells. Using automated image texture analysis, we also report the use of entropy- a

statistical measure of the randomness of pixel intensity within an image- to characterize images

of proflavine-stained oral cells.

Manual Segmentation for Nuclear to Cytoplasmic Ratio

The nuclei and cytoplasm of 100 normal cells and 100 CAL 27 cells were manually

segmented and measured in ImageJ. Mean and standard deviation values for nuclear to

cytoplasmic ratio were computed as described in the methods section. These results can be seen

in Fig 6. Note that the nuclear to cytoplasmic ratio of normal oral cells was significantly smaller than the ratio of Cal 27 oral squamous carcinoma cells. This is expected when comparing normal, mature exfoliated oral squamous cells to in vitro cultured oral squamous carcinoma cells.
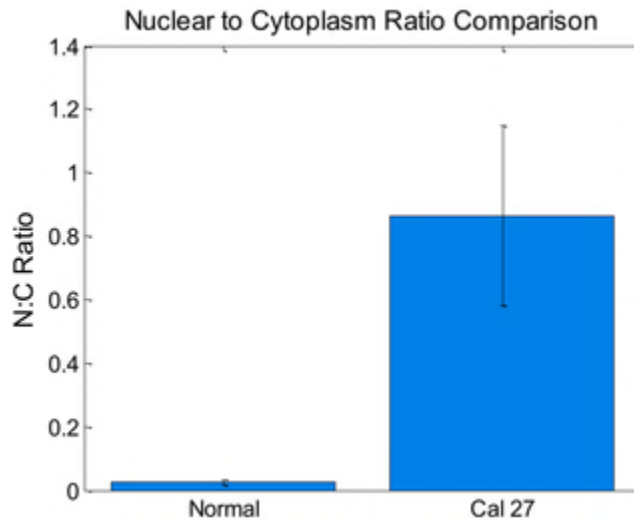
Figure 6. Bar plot comparing nuclear to cytoplasmic ratios for normal and CAL 27 cells. P value << 0.001 with Student T test. Error bars denote standard deviation.

Image Texture Analysis

The same 200 images used to calculate nuclear to cytoplasmic ratios were analyzed using automated image texture analysis. The texture of each image was quantified individually using standard deviation and entropy. The difference in mean standard deviation and mean entropy values for each cell type were statistically significant (Fig 7). The average entropy (measure of pixel intensity randomness) values for the cultured CAL 27 carcinoma cells were significantly larger than the normal exfoliated oral cells. Similarly, the standard deviation of pixel values in the CAL 27 images were significantly larger than the normal exfoliated oral cells. These results imply that the internal texture, or variation in pixel intensity values within the image of each type

of cell, is significantly greater in the Cal 27 cells when compared to the normal oral squamous cells.
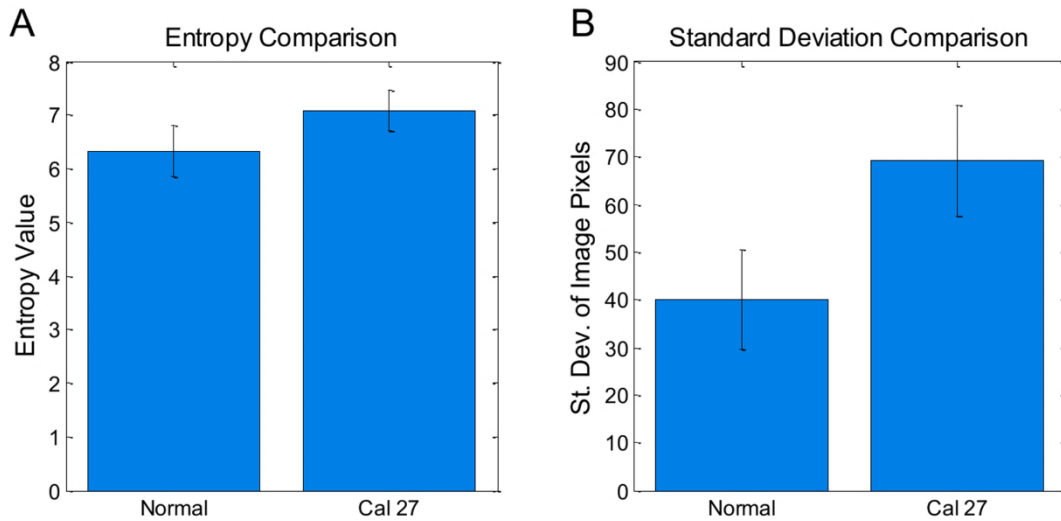
Figure 7. Bar plot comparing features between normal and CAL 27 cells. For both plots, p value << 0.001 with Student t-test. 100 cells per group. Error bars denote standard deviation.

4. Discussion

In this manuscript, we have demonstrated that proflavine can be used to rapidly stain fresh cells for cytologic analysis. Proflavine is an effective fluorescent contrast agent for exfoliated oral squamous cells, highlighting nuclear and cytoplasmic structures, including keratohyalin granules in mature cells. Structural definition in proflavine-stained cells is comparable to Giemsa or Papanicolaou staining. As opposed to the multi-step procedure of Papanicolaou staining, proflavine staining requires only the addition of the dye to the cell medium before mounting on a slide, eschewing the need for fixation. Giemsa is also a conveniently applied cytologic stain for hematology specimens, but lacks the benefit of the high signal to background ratios that fluorescence imaging provides. Compared to traditional pathology stains, proflavine is cost-effective, requires little setup and materials, and does not require lengthy staining time (see Table 1). Additionally, proflavine can rapidly stain freshly

collected leukocytes, clearly showing the multilobar structure of granulocytes in contrast to other cellular components. Finally, fluorescence images of proflavine stained cells can be analyzed quantitatively to highlight statistically significant differences in cell types based on morphologic features.

Table 2. Comparison of proflavine and PAP stained oral cells.

	Proflavine	Giemsa	Diff-Quik	H&E
Cost/Slide (materials only)	Estimated $0.50	Estimated $1.00†	$1.50 [26]	$3.39 [27]
Time/Slide Unit Value*	Estimated 1 min	14 min [28]	10-30 min [26]	1.5 min‡ [28]
*Not including time required to examine a slide to reach a diagnosis.				
†Based on an average yield of 1000 slides/L.				
‡H&E performed with an autostainer.				

Normal oral epithelial cells can be classified as basal, parabasal, intermediate, and superficial. Using our system we have collected mostly intermediate and superficial cells. Normal superficial cells have a large cytoplasm, with small, well defined nuclei, and small granules [5]. Cancer cells, due to their high mitotic activity, tend to have enlarged nuclei with diminished cytoplasm, to the point that the cytoplasm might visibly be a narrow region around the nucleus, or the nuclei aren't clearly visible [5]. Of the 100 normal oral epithelial cells stained with proflavine, all exhibited clearly defined nuclei, while of the 100 cancer cells imaged, slightly more than half displayed clearly defined nuclei. Proflavine stained cells displayed comparable cytologic features to PAP stained cells, such as well-defined membranes, nuclei, granules, and bacteria. Tables 2 and 3 qualitatively compare key image features of proflavine stained cells with conventionally (PAP or Giemsa) stained cells. Twenty randomly selected images from each set were visually inspected and evaluated for contrast between features—

membranes, nuclei, and keratohyalin granules—and the surrounding structures, and each set was

given an overall rating of distinct / strong contrast (++), visible but moderate contrast (+), or

poor contrast / not visible (-), with one feature (the presence of bacteria) classified as N/A for

cultured CAL 27 cells which were intentionally kept free of bacteria (see Table 2).

Table 3. Comparison of proflavine and Giemsa stained leukocytes.

Feature	Neutrophils		Monocytes		Lymphocytes	
	Proflavine	Giemsa	Proflavine	Giemsa	Proflavine	Giemsa
Lobar structure	++	++	++	++	++	++
Membrane	++	++	+	++	+	++
Lobar texture	++	++	++	++	++	++

Clearly defined cell membranes (++) were defined as showing a sharp contrast between

the edge of the membrane and the dark background surrounding the cell, while visible

membranes that had indistinct borders were defined as visible but moderate contrast (+). PAP

stained cells were designated as having clearly defined membranes (++) if they showed a sharp

contrast between the bluish-purple edge of the membrane and the white-beige background

surrounding the cell, while membranes that had a color difference but did not have a clearly

defined boundary were defined as (+). As seen in Table 2, PAP stained cells have clearly defined

cell membranes, and proflavine stained CAL 27 cells also had pronounced definition. Proflavine

stained normal cells were labelled with visible with moderate contrast (+) due to some of the

assessed cell membranes having low membrane to background contrast, or having a small gap in

the perimeter, where the membrane was left unstained and the cytoplasm seems to merge with

the background and surroundings. The nuclei, nucleoli, and bacteria were similarly assessed,

with their outer boundary compared against its surroundings (cytoplasm, nucleus, or cytoplasm,

respectively) for strong contrast (fluorescent or colorimetric). CAL 27 cells have large nuclei that

can be difficult to distinguish due to their size and lack of sharp boundaries in both PAP and

proflavine stained images, whereas their normal counterparts demonstrate high contrast with both methods of staining. Nucleoli, when visible, appeared with high contrast (++). The Golgi zone lacked the sharp boundaries of other features, and was defined as clear (++) when the area was a different intensity or color from the rest of the cytoplasm, visible but unclear (+) when there was a difference in the area surrounding the nucleus but difficult to tell where the Golgi zone ended and the cytoplasm began, and unclear (-) if the Golgi zone was not apparent, with proflavine showing a greater contrast in CAL 27 cells, but not distinguishable in either stain in normal oral cells.

Whole blood from healthy volunteers was also imaged, and classified by an expert pathologist (SGS). Features highlighted by proflavine staining, specifically the shape and number of lobar structures in the nuclei of neutrophils, could be used to classify leukocyte types [29]. Features such as lobar structure and membrane definition were comparable to Giemsa stained whole blood, with the primary difference being that erythrocytes are nearly invisible in proflavine fluorescence images. Randomly selected images from each set were assessed for features such as lobar structure, membrane definition, and lobar texture (see Table 3). Lobar structure and membrane was defined as high contrast (++) when the outer boundary was in sharp contrast with its surroundings, and the shape of the lobes or membrane were easy to identify. Both Giemsa and proflavine stained leukocytes showed clearly defined lobes, and did not require use of the visible but moderate contrast (+) label. Proflavine stained leukocytes had a higher tendency to have diffuse membrane boundaries (-), though they were clearly different from their surroundings. Lobar texture was assessed by looking at contrasting regions within the lobes themselves; areas within the same lobes can be in contrast (fluorescent or colorimetric) with neighboring regions. High contrast lobar texture (++) was defined as distinct patchy contrasting

58

regions within lobes, while the lobe texture was deemed to have moderate contrast (+) if there was little diffuse contrast within. Lobes without internal contrast (-) were commonly due to stain saturation and were rare in both Giemsa and proflavine stained leukocytes. In summary, proflavine stained cells displayed comparable cellular features to PAP and Giemsa stained cells, with less membrane definition overall due to the preferentially nuclei staining nature of proflavine, but no significant loss of features that would limit cytological classification.

Our study included only a select set of examples of quantitative image analysis of proflavine stained cells. We have shown that quantification of morphological features of normal oral, abnormal oral, and leukocytes is achievable using proflavine-staining cytology. Computational classification algorithms have been previously used in conjunction with imaging to provide additional tools for the pathologist [30]. Such algorithms could be implemented in cytological analysis of proflavine-stained leukocytes, using a combination of image texture and automatically-segmented structural features. Quantitative image analysis could be useful as an adjunctive tool when analyzing cytology specimens which are ambiguous. Additionally, computer-aided analysis could allow for diagnosis in the absence of an expertly trained pathologist. Computer-aided diagnostic platforms are currently in use, including image segmentation and analysis systems like the CytoSavant and the CellSearch system (specifically, CellTracks Analyzer) [31, 32]. Additional image analysis platforms and systems have been either implemented, or heavily researched, such as image analysis of ultrasound data [33-35].

As a research tool, proflavine staining could enable quantitative morphologic comparisons between many different cell types, while simplifying current imaging lab procedures. Proflavine fluorescence is compatible with conventional fluorescein isothiocyanate (FITC)-equipped microscopy tools, and could potentially be introduced as a label in flow

cytometry. Other methods of flow cytometry / image cytometry include classification of lymphoblastic leukemia using specific cell surface markers through immunofluorescent labeling [36]. Non-specific dyes such as propidum iodide and FITC have been used in combination to distinguish contours, such as the nuclei, and can approximate the accuracy and sensitivity of "advanced flow cytometers" [37].

Proflavine, as an aminoacridine derivative, is a promising contrast agent for point-of-care cytology due to its rapid uptake, highly simplified staining procedure, and robust and consistent staining of cellular structures. Other aminoacridine derivatives, such as acridine orange- with a peak excitation wavelength of 450 and emission of 650- have also been widely studied as a nucleic acid stain [38]. Acridine orange has also been studied for point-of-care diagnostics, such as malaria, due to its rapid and selective staining and high contrast images of intracellular plamsmodium parasites [39, 40]. Cost-effective point-of-care cytology is currently of high interest to the biomedical research community, especially for applications in rural or developing regions. Cell phone imaging technology has been developed and is still being investigated. For example, an inexpensive white blood cell density counter prototype measured fluorescence in leukocytes stained with Syto16, a fluorescent nucleic acid stain that required a 30 minute incubation period [41]. We propose that proflavine can be used as a fluorescent structural dye across a wide range of unfixed cytology and solid tissue specimens. Using proflavine in combination with current point-of-care diagnostics, including portable microscopy platforms, microendoscopy devices and lab-on-chip technology, could prove beneficial in reducing time, procedure, and cost of screening diseases such as cervical cancer [24, 42-44].

References

[1] S. P. Prieto, A. J. Powless, J. W. Boice, S. G. Sharma and T. J. Muldoon, "Proflavine Hemisulfate as a Fluorescent Contrast Agent for Point-of-Care Cytology," *PloS One,* vol. 10, *(5),* pp. e0125598, 2015.

[2] W. Kühnel, *Color Atlas of Cytology, Histology and Microscopic Anatomy.* Georg Thieme Verlag, 2003.

[3] M. J. Pomeranz and S. S. Stahl, "A correlative study of cytodiagnosis and biopsy," *Oral Surgery, Oral Medicine, Oral Pathology,* vol. 6, *(8),* pp. 1026-1031, 1953.

[4] V. Kumar, A. K. Abbas, N. Fausto and J. C. Aster, *Robbins and Cotran Pathologic Basis of Disease, Professional Edition E-Book.* elsevier health sciences, 2014.

[5] S. R. Kini, *Color Atlas of Differential Diagnosis in Exfoliative and Aspiration Cytopathology.* Lippincott Williams & Wilkins, 2011.

[6] D. M. Shotton, "Fluorescence microscopy revisited Fluorescence Microscopy of Living Cells in Culture, Part B, Quantitative Fluorescence Microscopy–Imaging and spectroscopy (1989). Edited by D. Lansing Taylor and YU-LI Wang. Methods in Cell Biology 30. Academic Press: New York. 503pp.£ 94," Bioessays, vol. 14, (6), pp. 427-429, 1992.

[7] W. T. Mason, Fluorescent and Luminescent Probes for Biological Activity: A Practical Guide to Technology for Quantitative Real-Time Analysis. Academic Press, 1999.

[8] B. Schutte, M. Reynders, F. Bosman and G. Blijham, "Flow cytometric determination of DNA ploidy level in nuclei isolated from paraffin-embedded tissue," Cytometry Part A, vol. 6, (1), pp. 26-30, 1985.

[9] W. E. Corver, G. J. Fleuren and C. J. Cornelisse, "Improved single laser measurement of two cellular antigens and DNA-ploidy by the combined use of propidium iodide and TO-PRO-3 iodide," Cytometry, vol. 28, (4), pp. 329-336, Aug 1, 1997.

[10] N. N. Zhadin and R. R. Alfano, "Correction of the internal absorption effect in fluorescence emission and excitation spectra from absorbing and highly scattering media: theory and experiment," J. Biomed. Opt., vol. 3, (2), pp. 171-187, 1998.

[11] Y. Kubota and R. F. Steiner, "Fluorescence decay and quantum yield characteristics of acridine orange and proflavine bound to DNA," Biophys. Chem., vol. 6, (3), pp. 279-289, 1977.

[12] E. Robbins, "The rate of proflavin passage into single living cells with application to permeability studies," J. Gen. Physiol., vol. 43, pp. 853-866, Mar, 1960.

[13] C. J. Alden and S. Arnott, "Stereochemical model for proflavine intercalation in A-DNA," Nucleic Acids Res., vol. 4, (11), pp. 3855-3862, 1977.

[14] W. D. Sasikala and A. Mukherjee, "Intercalation and de-intercalation pathway of proflavine through the minor and major grooves of DNA: roles of water and entropy," Physical Chemistry Chemical Physics, vol. 15, (17), pp. 6446-6455, 2013.

[15] M. Wainwright, "Acridine—a neglected antibacterial chromophore," J. Antimicrob. Chemother., vol. 47, (1), pp. 1-13, 2001.

[16] C. Browning, R. Gulbransen and L. Thornton, "The antiseptic properties of acriflavine and proflavine, and brilliant green: with special reference to suitability for wound therapy," Br. Med. J., vol. 2, (2951), pp. 70, 1917.

[17] E. S. DeJong, C. Chang, M. K. Gilson and J. P. Marino, "Proflavine acts as a Rev inhibitor by targeting the high-affinity Rev binding site of the Rev responsive element of HIV-1," Biochemistry (N. Y.), vol. 42, (26), pp. 8035-8046, 2003.

[18] K. J. Rosbach, D. Shin, T. J. Muldoon, M. A. Quraishi, L. P. Middleton, K. K. Hunt, F. Meric-Bernstam, T. Yu, R. R. Richards-Kortum and W. Yang, "High-resolution fiber optic microscopy with fluorescent contrast enhancement for the identification of axillary lymph node metastases in breast cancer: a pilot study," Biomedical Optics Express, vol. 1, (3), pp. 911-922, 2010.

[19] L. L. Levy, P. M. Vila, R. W. Park, R. Schwarz, A. D. Polydorides, M. S. Teng, V. V. Gurudutt, E. M. Genden, B. Miles and S. Anandasabapathy, "High-Resolution Optical Imaging of Benign and Malignant Mucosa in the Upper Aerodigestive Tract: An Atlas for Image-Guided Surgery," ISRN Minimally Invasive Surgery, vol. 2012, 2012.

[20] Y. Yang, J. Bugno and S. Hong, "Nanoscale polymeric penetration enhancers in topical drug delivery," Polymer Chemistry, vol. 4, (9), pp. 2651-2657, 2013.

[21] J. D. Kawedia, Y. Zhang, A. L. Myers, R. R. Richards-Kortum, M. A. Kramer, A. M. Gillenwater and K. S. Culotta, "Physical and chemical stability of proflavine contrast agent solutions for early detection of oral cancer," Journal of Oncology Pharmacy Practice, vol. 22, (1), pp. 21-25, 2016.

[22] K. D. McClatchey, "Manual of Basic Techniques for a Health Laboratory," Archives of Pathology & Laboratory Medicine, (128), pp. 495-495, 2004.

[23] S. Gupta, K. Chachra, P. Bhadola and P. Sodhani, "Modified Papanicolaou staining protocol with minimum alcohol use: a cost-cutting measure for resource-limited settings," Cytopathology, vol. 21, (4), pp. 229-233, 2010.

[24] T. J. Muldoon, M. C. Pierce, D. L. Nida, M. D. Williams, A. Gillenwater and R. Richards-Kortum, "Subcellular-resolution molecular imaging within living tissue by fiber microendoscopy," Optics Express, vol. 15, (25), pp. 16413-16423, 2007.

[25] C. A. Schneider, W. S. Rasband and K. W. Eliceiri, "NIH Image to ImageJ: 25 years of image analysis," Nature Methods, vol. 9, (7), pp. 671, 2012.

[26] P. Cregan, A. Yamamoto, A. Lum, T. VanDerHeide, M. MacDonald and L. Pulliam, "Comparison of four methods for rapid detection of Pneumocystis carinii in respiratory specimens," J. Clin. Microbiol., vol. 28, (11), pp. 2432-2436, Nov, 1990.

[27] D. Muirhead, P. Aoun, M. Powell, F. Juncker and J. Mollerup, "Pathology economic model tool: a novel approach to workflow and budget cost analysis in an anatomic pathology laboratory," Arch. Pathol. Lab. Med., vol. 134, (8), pp. 1164-1169, 2010.

[28] L. Laine, D. N. Lewin, W. Naritoku and H. Cohen, "Prospective comparison of H&E, Giemsa, and Genta stains for the diagnosis of Helicobacter pylori," Gastrointest. Endosc., vol. 45, (6), pp. 463-467, 1997.

[29] A. V. Hoffbrand, Postgraduate Haematology. John Wiley & Sons, 2016.

[30] L. M. Buckley, K. Sanders, M. Shih, S. Kallar and C. Hampton, "Obstacles to promotion? Values of women faculty about career success and recognition," Academic Medicine, vol. 75, (3), pp. 283-288, 2000.

[31] S. Riethdorf, H. Fritsche, V. Muller, T. Rau, C. Schindlbeck, B. Rack, W. Janni, C. Coith, K. Beck, F. Janicke, S. Jackson, T. Gornet, M. Cristofanilli and K. Pantel, "Detection of circulating tumor cells in peripheral blood of patients with metastatic breast cancer: a validation study of the CellSearch system," Clin. Cancer Res., vol. 13, (3), pp. 920-928, Feb 1, 2007.

[32] C. E. MacAulay, B. Palcic, D. M. Garner, S. A. Harrison and B. W. Jaggi, "Method and apparatus for automatically detecting malignancy-associated changes,", 1999.

[33] Y. M. Kadah, A. A. Farag, J. M. Zurada, A. M. Badawi and A. Youssef, "Classification algorithms for quantitative tissue characterization of diffuse liver disease from ultrasound images," IEEE Trans. Med. Imaging, vol. 15, (4), pp. 466-478, 1996.

[34] R. Kamalov, M. Guillaud, D. Haskins, A. Harrison, R. Kemp, D. Chiu, M. Follen and C. MacAulay, "A Java application for tissue section image analysis," Comput. Methods Programs Biomed., vol. 77, (2), pp. 99-113, 2005.

[35] M. Guillaud, J. L. Benedet, S. B. Cantor, G. Staerkel, M. Follen and C. MacAulay, "DNA ploidy compared with human papilloma virus testing (Hybrid Capture II) and conventional cervical cytology as a primary screening test for cervical high-grade lesions and cancer in 1555 patients with biopsy confirmation," Cancer, vol. 107, (2), pp. 309-318, 2006.

[36] O. D. Laerum and T. Farsund, "Clinical application of flow cytometry: a review," Cytometry Part A, vol. 2, (1), pp. 1-13, 1981.

[37] P. Pozarowski, E. Holden and Z. Darzynkiewicz, "Laser scanning cytometry," in Cell Imaging TechniquesAnonymous Springer, 2006, pp. 165-192.

[38] S. P. Reddy, P. Ramani and P. Nainani, "Confocal microscopy and exfoliative cytology," J. Oral Maxillofac. Pathol., vol. 17, (2), pp. 217-221, May, 2013.

[39] S. Nandwani, M. Mathur and S. Rawat, "Evaluation of the direct acridine orange staining method and Q.B.C. test for diagnosis of malaria in Delhi, India," J. Commun. Dis., vol. 35, (4), pp. 279-282, Dec, 2003.

[40] Woodley Equipment Company Ltd, "QBC F.A.S.T. Malaria Stain," vol. 2018, (03/28), .

[41] H. Zhu, S. Mavandadi, A. F. Coskun, O. Yaglidere and A. Ozcan, "Optofluidic fluorescent imaging cytometry on a cell phone," Anal. Chem., vol. 83, (17), pp. 6641-6647, 2011.

[42] S. J. Goldie, L. Gaffikin, J. D. Goldhaber-Fiebert, A. Gordillo-Tobar, C. Levin, C. Mahé and T. C. Wright, "Cost-effectiveness of cervical-cancer screening in five developing countries," N. Engl. J. Med., vol. 353, (20), pp. 2158-2168, 2005.

[43] J. V. Jokerst and J. T. McDevitt, "Programmable nano-bio-chips: multifunctional clinical tools for use at the point-of-care," Nanomedicine, vol. 5, (1), pp. 143-155, 2010.

[44] H. Zhu, S. O. Isikman, O. Mudanyali, A. Greenbaum and A. Ozcan, "Optical imaging techniques for point-of-care diagnostics," Lab on a Chip, vol. 13, (1), pp. 51-67, 2013.

Chapter III: **Quantitative analysis of ex vivo colorectal epithelium using an automated feature extraction algorithm for microendoscopy image data [1]**

1. Introduction

Colorectal cancer (CRC) is currently the third leading cause of cancer death in the United States, despite increased screening rates and a concomitant decline in incidence and mortality [2, 3]. CRC commonly arises from adenomatous polyps, some of which may progress into invasive adenocarcinomas over time [4]. This progression is thought to be slow and is dependent on the size and histology of the polyp [5]. Screening for colorectal polyps via conventional white light colonoscopy has had a dramatic effect on reducing the overall morbidity and mortality due to CRC, as visible polyps can be safely removed during this procedure [6]. However, small lesions, sessile (i.e., flat) lesions, or regions of occult dysplasia can be occasionally missed. A broad range of alternative strategies have been recently employed to improve endoscopic screening methods, including autofluorescence endoscopy with real-time image processing, narrow band reflectance imaging, and combined multimodal methods [7-9]. While these approaches have demonstrated improved sensitivity for early detection of neoplasia, false positive rates remain elevated, limiting widespread adoption of these methods for screening purposes [10].

High-resolution endoscopic imaging modalities have been widely explored to improve detection of these focal regions of early dysplasia in gastrointestinal epithelium [11-14]. Laser scanning confocal imaging methods employing novel miniaturized distal scanning mechanisms based on microelectromechanical systems have been demonstrated to yield excellent lateral and axial spatial resolution [15-17]. Clinical trials of a hybrid endoscope/miniaturized laser scanning confocal microscope system have demonstrated utility in diagnosing focal regions of dysplasia in the setting of Barrett's esophagus and during colonoscopy [18]. These systems offer real-time,

histology-level information to be displayed to the clinician at the time of endoscopy, potentially greatly improving biopsy targeting to locations most likely to show evidence of dysplasia [19, 20]. Nonscanning, wide-field fiber bundle microendoscopy methods have also been demonstrated to yield high-resolution image data from the superficial epithelium with promising diagnostic accuracy despite the limited field of view [21], restricted by the biopsy port (∼2mm∼2 mm) through which these devices are deployed *in vivo*. While certain technical challenges that remain before microendoscopy methods may be widely disseminated in clinical applications, the combination of improved wide-field endoscopic methods and high-resolution microendoscopy methods may greatly improve upon currently achieved accuracy [21, 22].

Furthermore, although several clinical trials of a high-resolution fiber bundle microendoscopy device have demonstrated excellent interobserver agreement in interpretation and classification of fiber bundle microendoscopy images of colorectal polyps [21], there is currently no widely accepted, quantitative image analysis criteria that can be used to objectively classify fluorescence image data of colorectal polyps without human intervention. Previously demonstrated interobserver agreement of microendoscopic image interpretation is dependent on highly trained staff and physicians. This need for high levels of training can be limiting to the dissemination of microendoscopic screening devices, and quantifiable image analysis criteria is an option to grant unspecialized practitioners the tools for consistent diagnosis at a reduced burden of training.

Quantitative image analysis applied in other microendoscopy studies include texture features of ovarian cancer confocal microendoscopy, cell density in mouse model sarcomas using wide-field structured illumination, and wavelet decomposition in color colonoscopic video frames [23-25]. These algorithms quantify a range of image features, such as texture (including

spatial-frequency content), cell nuclei image segmentation and counting, and discrete wavelet transform and covariance [23-25]. There are numerous image features that could be extracted for quantification, depending on the data acquired by the imaging modality, but for the quantification of image features in fluorescence microendoscopy of nonspecific staining of bulk tissue, we chose image features that trained clinicians would typically consider in their analysis, namely crypt shape, size, and homogeneity. Pathologists who study *en face* histopathology of colorectal tissue for signs of dysplasia take into account image features such as elongated or branched crypts, clusters of crypts or crypts of abnormal size, irregular contours, and stratification of the nuclei surrounding the crypt. While pathologists commonly use nucleic patterns as a marker for abnormality, due to the length of the colorectal tract, it is of greater relevance during microendoscopic screening to use a fiber bundle with a larger field of view than to acquire images that resolve individual nuclei. Therefore, the algorithm we developed focuses on quantifying the larger structures of epithelial morphology such as crypt area and circularity. Additionally, the extent to which image morphology varies in clinically normal colorectal tissue in patients with different clinical histories, such as diagnosis, chemotherapy, radiation, prior surgeries, or other therapy, has not been described or quantified. There is a significant need for a quantitative benchmark for future detection of occult dysplasia in patients who have a range of diagnoses and/or prior treatment, and a need for generalized image analysis tools for advanced microendoscopy imaging modalities within the gastrointestinal tract.

Any quantitative image analysis algorithm must be able to exclude motion-blurred or other low-quality images; this is of particular concern in the demanding environment of an *in vivo* endoscopy procedure. Approaches such as microarray image processors have demonstrated that the inherent variability in signal-to-background ratios is correlated with image quality [26].

Low signal-to-background intensity ratios can affect the ability of an algorithm to accurately detect image features, and qualitative image exclusion via manual inspection may introduce human bias and additional error. While some microendoscopy images may be significantly distorted, the parameters for excluding low-quality images for machine detection by observation alone may vary in accuracy when compared to a quantitative threshold based on a standardized metric.

The objective of the study presented in this paper is to explore the quantification of microendoscopy images in the clinically normal appearing tissue surrounding grossly visible lesions in recently resected colorectal specimens, in order to extract key differences that may be used to classify benign epithelial tissue from dysplastic tissue in future computer-aided diagnostic algorithms. We present both a quantitative image quality control algorithm to exclude low-quality images, as well as an intensity-adaptive quantitative image feature extraction algorithm (QFEA) to segment and quantify crypt morphology in images of superficial colorectal epithelium acquired via fiber bundle microendoscopy. Both algorithms were first validated using an extensive training library constructed from image data acquired from fresh porcine colorectal epithelium, a tissue histologically similar to human colorectal epithelium. In addition to individual image acquisition, consecutive images were acquired for mosaicking, to demonstrate the ability to improve the inherently small field of view in fiber bundle microendoscopy images, one prominent disadvantage of microendoscopic systems, using image registration of consecutive fields of view [27]. All individual images, and several mosaics, collected from human specimens were then analyzed for quality and subsequently quantified using QFEA. Images were analyzed to segment crypts within the superficial epithelium, and a centroid map was created for identified crypts. From each of these maps, quantitative features were calculated,

focused on crypt-specific properties such as crypt area and circularity. While these metrics were calculated for proflavine fluorescence fiber bundle microendoscopy, this method could be broadly applied over a range of high-resolution microendoscopy imaging modalities.

2. Materials and Methods

2.1. Fiber Bundle Microendoscopy System

The microscopy system used has been described previously [1, 28] and comprises a blue light-emitting diode light source (455 nm, Philips) producing 0.5 mW at the sample, a filter set (Chroma Tech) with a 525/40nm emission bandpass filter, a 460 nm shortpass filter, and a dichroic mirror with a cutoff wavelength of 475 nm, a camera [Flea 3 (USB 3.0), Point Grey Research Inc., California], a 10x objective (NA 0.25, Olympus, Japan), and a customized fiber bundle image guide with a 1 mm active area diameter (FIGH-50-1100N fiber, Myriad Fiber Imaging Tech. Inc.). The fiber bundle image guide has custom SMA connectors on both ends; on the distal end, a modified SMA connector's rounded edges reduce the friction between the fiber bundle and the epithelial tissue for smoother continuous image acquisition, as well as protecting the glass surface from chipping.

2.2. Porcine Tissue

Microendoscopic images of freshly resected colonic porcine tissue were acquired, in collaboration with Siloam Springs Processing (Siloam Springs, Arkansas), a local slaughterhouse. One hundred images were acquired from four healthy animals for training validation of both the quality control and quantitative feature extraction algorithms. These images were acquired from regions ∼5cm in length, with an average of 30 images acquired per region. Porcine colorectal epithelium, histologically similar in structure and scale to human colorectal epithelium, has been previously used as a human analog in myriad imaging studies

[29, 30]. Figure 1 shows a comparison of normal porcine and normal human colorectal tissue using microendoscopic and histopathology images.
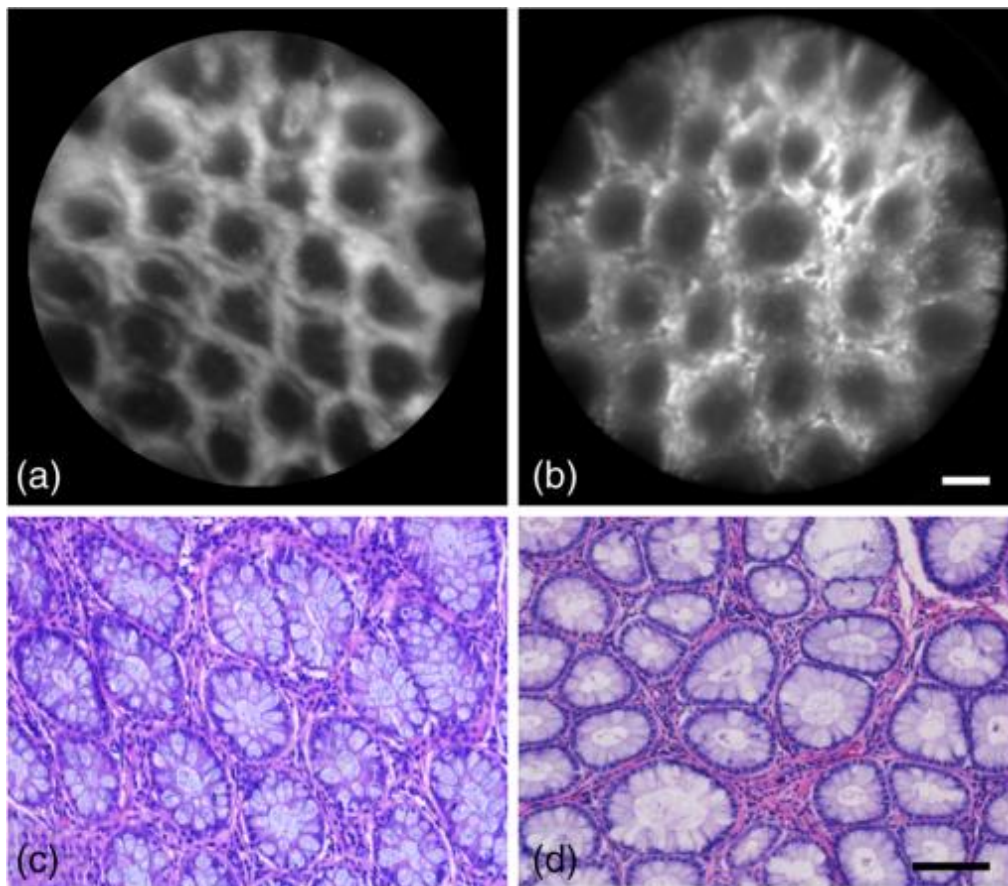
Figure 1. Normal human versus normal porcine colorectal epithelial tissue. (a) and (b) Microendoscopy images; scale bar is 100μm. (c) and (d) Histopathology images; scale bar is 100μm. (a) and (c) Normal human colorectal epithelium. (b) and (d) Normal porcine colorectal epithelium.

2.3. Human Subjects

Microendoscopic images of freshly resected human colorectal tissue were acquired in collaboration with the University of Arkansas for Medical Sciences (UAMS) in Little Rock, Arkansas, following informed consent of each subject per Institutional Review Board standards at both institutions (IRB #13-06-759 University of Arkansas, Fayetteville, IRB #202224 UAMS). A total of 10 subjects were recruited for this study, with two subjects excluded due to lack of

images of clinically normal regions. Thirty-nine microendoscopic images were used to quantify the image segmentation algorithm's crypt detection sensitivity. Twenty-eight of these images were used for quantification (after exclusion due to image quality, as described in Sec. 2.5). For each human specimen, all microendoscopy images were acquired from a region ~2cm in length, with an average of 15 images acquired per region. Participation was limited to both male and female subjects over the age of 18 with known or suspected colorectal dysplasia or cancer, and were scheduled for either endoscopic or surgical resection of abnormal tissue. Informed consent was performed on each subject prior to scheduled surgery.

2.4. Microendoscopy Image Acquisition

Upon receipt of the freshly resected porcine tissue, the colon specimen was longitudinally sectioned and cleaned using cold saline. Microendoscopy images were acquired immediately following topical application of proflavine (0.01% w/v in 1x phosphate buffered saline) with a cotton swab to epithelial surface, with occasional reapplication of dye after several minutes as needed. Individual images were acquired by manually placing the distal end of the fiber bundle in contact with the epithelial surface of the tissue; consecutive images were acquired by slowly dragging the distal end over the epithelial surface for subsequent processing into mosaics. Sequential image stacks were acquired over 10 to 20 s (covering ~1 to 2 cm of epithelium), and all images were acquired in the range of 100 to 150 ms exposure and 0 to 5 dB gain. At the conclusion of the imaging study, porcine tissue was placed in 10% formalin for fixation overnight, prior to paraffin embedding, sectioning, and hematoxylin and eosin staining.

For human subject imaging, the resected colorectal tissue was first longitudinally sectioned and then pinned onto a paraffin block. Additional pins were placed 2 cm apart at regions of interest, and images were acquired along a linear path between the pins. Microendoscopy images were

acquired immediately following topical application of proflavine (0.01% w/v in 1x phosphate buffered saline) with a cotton swab to epithelial surface, with occasional reapplication of dye after several minutes as needed. Individual images were acquired by manually placing the distal end of the fiber bundle in contact with the epithelial surface of the tissue; consecutive images were acquired by slowly dragging the distal end over the epithelial surface for subsequent processing into mosaics. Sequential image stacks were acquired over 10 to 20 s (covering ~1 to 2 cm of epithelium), and all images were acquired in the range of 100 to 150 ms exposure and 0 to 5 dB gain. For each specimen, typically one to two regions were imaged and sectioned for histopathology confirmation. After imaging, the study pathologist (K.L.) sectioned the tissue along the path marked by the pins, which facilitated the correlation of histopathology to microendoscopy (Fig. 2).
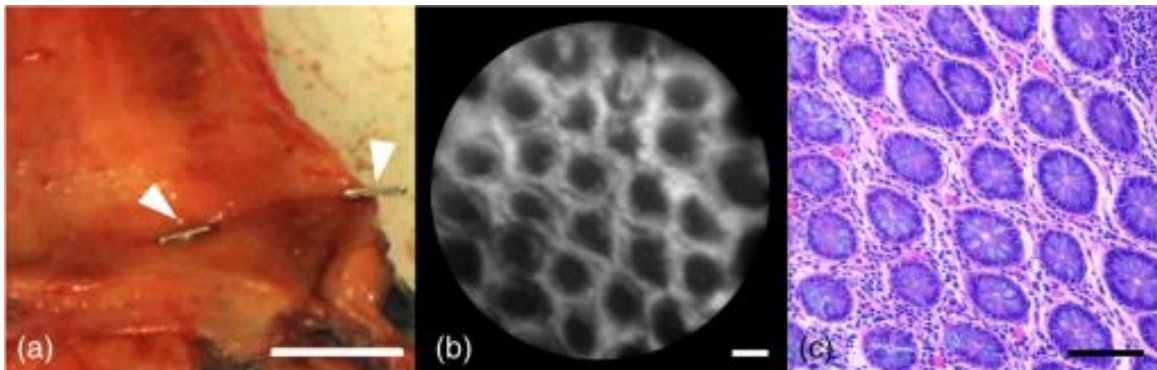

Figure 2. Examples of tissue preparation, microendoscopic image, and histopathology. (a) Freshly resected gross tissue, pinned to paraffin block; white arrows point to pins delineating imaging location. Scale bar is ~2cm. (b) Microendoscopic image of untreated normal colon epithelium. Scale bar is 100μm. (c) Histopathology image of untreated normal colon epithelium. Scale bar is 100μm. Images have enhanced contrast and brightness for publishing.

Two-centimeter sections of transversely sliced tissue were taken from imaging sites, and diagnoses provided by a clinically trained gastrointestinal pathologist (K.L.). Tissue was classified as clinically normal, normal with underlying invasive adenocarcinoma, invasive adenocarcinoma, or tubular adenoma at each of the imaged sites.

2.5. Quantitative Image Quality Control

We developed a quantitative image quality control algorithm to exclude low-quality images prior to image quantification, based on crypt-specific signal-to-background ratio. This signal-to-background is based on the contrast between the signal intensity within each crypt and the surrounding region; the crypt should be darker than the DNA-containing cell nuclei around it. If the ratio between the intensity values in the surrounding region and the intensity values in the crypt was too low, the algorithm lost sensitivity in image segmentation and quantification (Fig. 3). The image segmentation and quantification algorithm was applied to images of both low and high quality (contrast); specifically, the sensitivity and positive predictive value (PPV) of crypt identification was calculated. Images with low contrast were excluded from pilot study quantification of crypt image features.
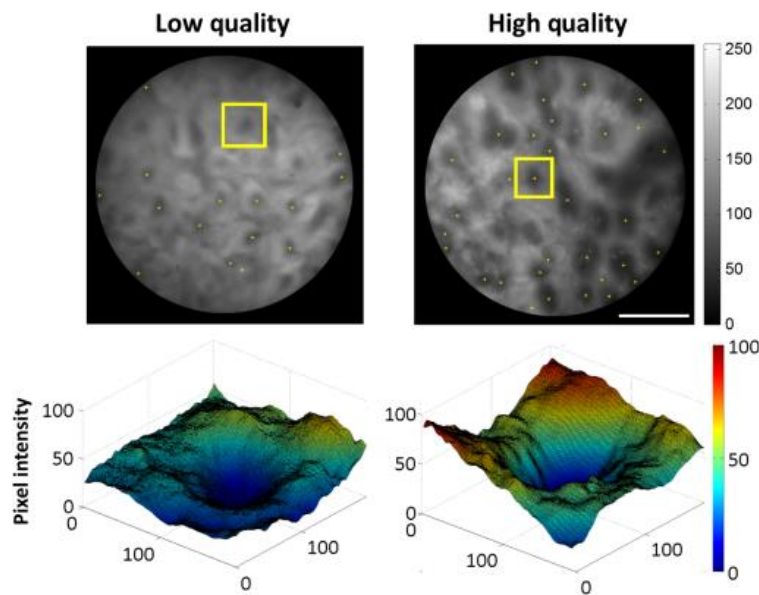
Figure 3. Example of image quality based on signal-to-background contrast. Top row: microendoscopy image of human epithelium, with superimposed yellow stars marking centroids, and yellow box labelling the selected crypt; scale bar is 250µm. Bottom row: surface maps of pixel intensity in region marked by yellow box (top row). Unlabeled axes are in pixels; 100 pixels are approximately 75µm. The respective lowest intensity of each selection was subtracted from the image arrays, so that the lowest pixel value is zero without altering the differences in intensity. The same smoothing function applied to the line profiles for quality ratio (QR) calculation was applied to these image arrays.

Prior to calculating the contrast (signal-to-background) ratio, which we have termed the QR, all images were preprocessed to reduce common intrascene variation, which can result from, e.g., varying amounts of mucosa or variations in staining due to the topography of the tissue. The algorithm first masked the original images to restrict analysis and image segmentation to only the active area of the fiber bundle, and then contrast the enhanced images, whereby intensity values in the image are mapped to new values so that 1% of the image pixels are saturated at the lower and upper contrast limits (in this preprocessing step, 1% was saturated at zero intensity and 1% was saturated at 255), serving to standardize the images by utilizing the full range of the intensity values, before calculating the QR. Images were masked, excluding any values outside a circle 1000 pixels (750μm) in diameter, ensuring only the uniformly illuminated region of the active area is analyzed. A microendoscopy image collected from a uniformly fluorescent agarose phantom (2% w/v agarose, mixed with 0.01% w/v proflavine, in distilled water) displayed in the full range of colors in the colormap demonstrates this process (Fig. 4).
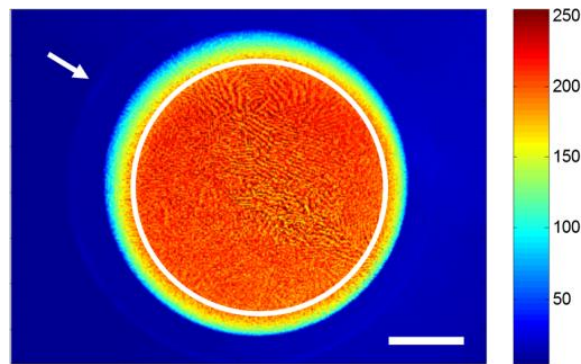
Figure 4. Example of unmasked microendoscopy image. Arrow points to unwanted light from outside the fiber bundle. The circle is 1000 pixels in diameter and represents the image area after masking. Image taken of agarose phantom mixed with 0.01% (w/v) proflavine. Scale bar is 250μm.

To calculate the QR, the image quality control algorithm extracted vertical and horizontal line profiles (90 total) from the image, at intervals of 40 pixels (Fig. 5). This was done to ensure

that line profiles would cross the majority of crypts at least once, accounting for the physical

scale of crypts (ranging 75 to 250μm in diameter) and the scale of the pixels at the image plane

(Fig. 5). Each line profile was smoothed to eliminate small intensity variations due to the fiber

bundle pattern itself. This fiber pattern exhibits a spatial frequency of ~10 pixels; smoothing

eliminates this periodic variation [Figs. 6(a)–6(d)]. Then, local regional minima and maxima

were determined for each line profile, and the ratio between each minimum and its adjacent

maximum was calculated [Fig. 6(e)]. The regional minima and maxima were determined by

comparing regions of eight values (eight-connected neighborhoods) to surrounding values and

outputting a binary map of the values of the local minima or maxima. All ratios within each

image were then averaged to output a single global average QR metric for the

image. Figure 7 shows the flow diagram of steps for preprocessing (image masking and contrast

enhancement) and QR calculation.
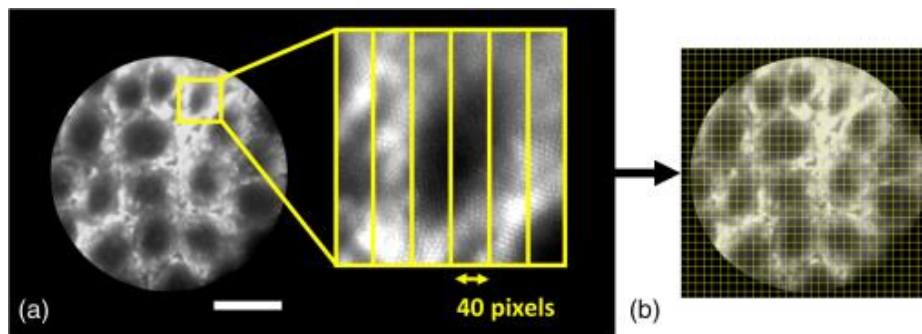
Figure 5. Example of typical crypt sizes and chosen grid line spacing. (a) Microendoscopic image of healthy porcine colorectal tissue. Inset shows a normal crypt with a width of 80 pixels. Vertical yellow lines represent the grid lines, with spacing of 40 pixels (yellow double-headed arrow), that are used to calculate QR in the image quality control algorithm. Scale bar is 250μm. (b) Example of grid structure and spacing used to extract line profiles for QR calculation.
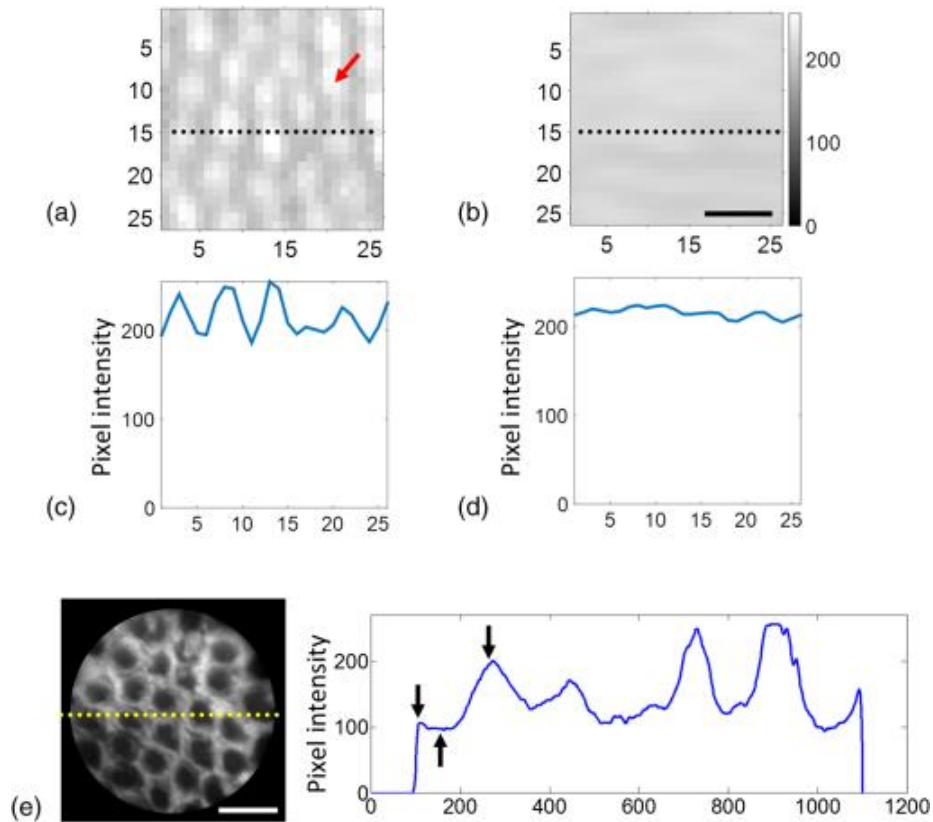
Figure 6. Smoothing and QR calculation. (a) and (b) Microendoscopy images of flat-field illumination showing individual fiber artifacts, before and after smoothing is applied. Axes display distance in pixels; scale bar is 6μm. (a) Prior to smoothing, gaps between individual fibers (red arrow) display a significantly lower intensity than the fiber active area. Periodic variation in contrast is more clearly visible in the line plot in (c). (b) After smoothing, the intensity difference between individual fiber areas and gaps is reduced, visible in the line plot in (d). (e) Microendoscopy image of normal epithelium and resulting line plot of image intensity; scale bar is 250μm. Line plot was smoothed and plotted against distance in pixels. Black arrows point to first set of minimum (trough) and maxima (peaks). All peak-to-trough values in the image are averaged to yield a global QR value.
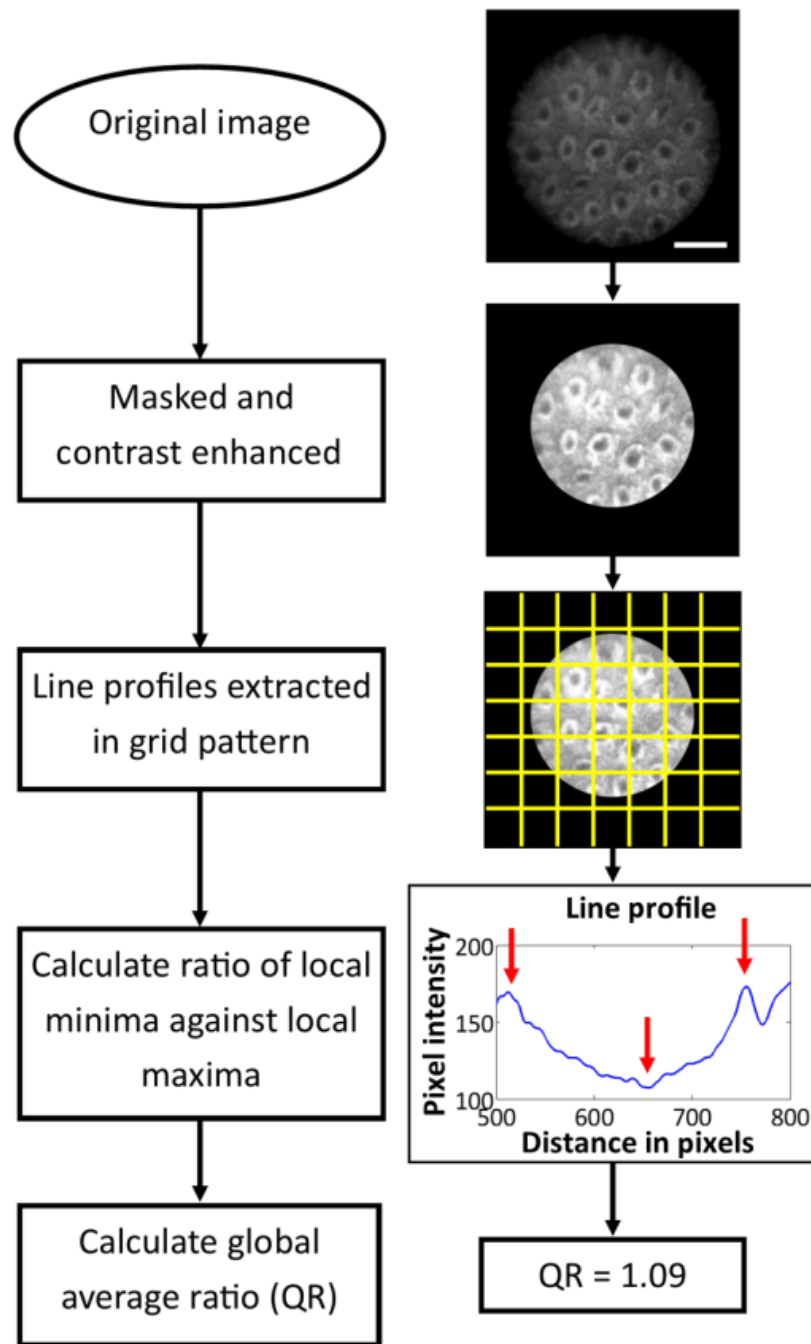
Figure 7. Flow diagram of image preprocessing and quantitative image quality control. The original image was masked and contrast enhanced; then line profiles were extracted every 40 pixels, in a grid-like pattern. Scale bar is 250μm. The local minima and maxima of each line profile was extracted, and the algorithm calculated the ratio between each minima and its adjacent maxima. The global average of the ratios calculated across the image was termed as the image's QR.

In order to demonstrate the effect of QR on image quality and overall automated crypt segmentation, we performed the automated QR calculation on the entire porcine image data set (100 images) and human data set (39 images). For each image, in both data sets, the number of crypts was determined via manual inspection to determine a ground truth value. The average QR was tabulated against crypt detection sensitivity (see Secs. 2.6.1 and 3.1) to compute the optimum image exclusion threshold value. The aggregate average sensitivity was calculated by averaging the sensitivity of all images with a QR greater than, or equal to, the respective QR value on the xx-axis, further described in Sec. 3.2.

2.6. Automated Segmentation of Crypt Features

QFEA (Fig. 8) was developed to automatically identify and segment each crypt present within microendoscopic images, and use this segmented map of crypt location to compute morphologic parameters such as area and circularity (Sec. 2.6.2). The accuracy of the QFEA's image segmentation and crypt identification was greatly influenced by the contrast enhancement applied prior to conversion into a binary image (further explained in Sec. 2.6.1). To increase sensitivity of image segmentation, fivefold cross-validation was performed using the porcine (training) data set in order to compute the average detection sensitivity for different contrast enhancement parameters (Sec. 2.6.2). The selected contrast enhancement contrast limits were then applied to both porcine and human images for calculation of sensitivity and PPV of images with various QR values (results in Sec. 3.2).
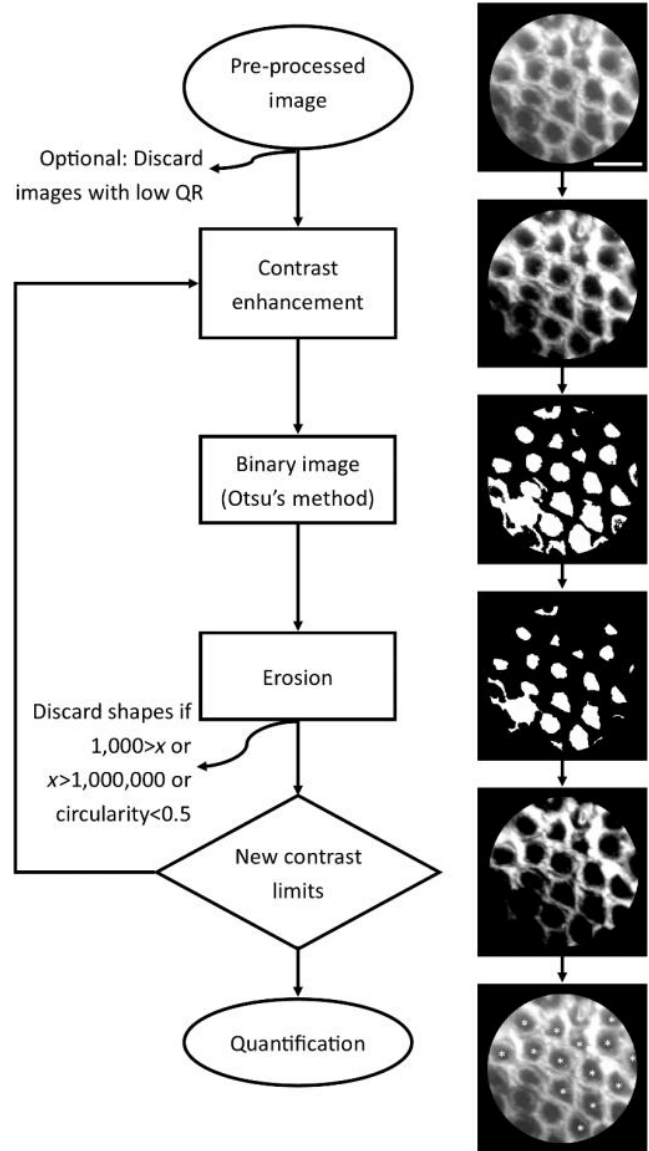
Figure 8. Quantification algorithm flowchart. x is the quantified area of each crypt in pixels. Circularity is defined in Eq. (3). Multiple contrast limits were applied to increase sensitivity. Scale bar is 250μm

2.6.1. Selection of optimal contrast limits for image segmentation, using porcine image test data set

As previously stated, all images were preprocessed to reduce common intrascene variation, by masking and contrast enhancement. Section 2.5 describes the preprocessing contrast enhancement, which used a lower contrast limit value of 0 and upper contrast limit value of 1,

hereafter referred as the [0 1] contrast limits. Due to contrast intensity variations in images, further contrast enhancement is necessary to create a binary image of crypts with acceptable crypt detection sensitivity. As seen in Fig. 9, intensity-adaptive contrast enhancement was used to improve overall crypt detection accuracy. Contrast enhancement, which requires selection of lower and upper contrast limits, scales image intensity values (0 to 255, for our images) between 0 and 1, whereby intensity values in the image are mapped to new values so that 1% of the image pixels are saturated at the lower and upper contrast limits, as described in Sec. 2.5. Figure 9 shows the histograms of an original image and images after contrast enhancement with different contrast limit pairs. Crypt detection is not shown for the original image, and the image with [0 1] contrast limits, because the image segmentation algorithm (QFEA) did not detect any crypts (neither true positive nor false positive) for either of these images. Note that the QFEA detected crypts in the image that was contrast enhanced using the [0.4 0.9] contrast limits, which were missed by the [0.5 0.9] contrast limits. Contrast limits affect the ability of the QFEA to recognize and segment crypts in different regions of the image; therefore, the overall crypt detection sensitivity of the algorithm was increased with the combination of multiple contrast limit pairs.
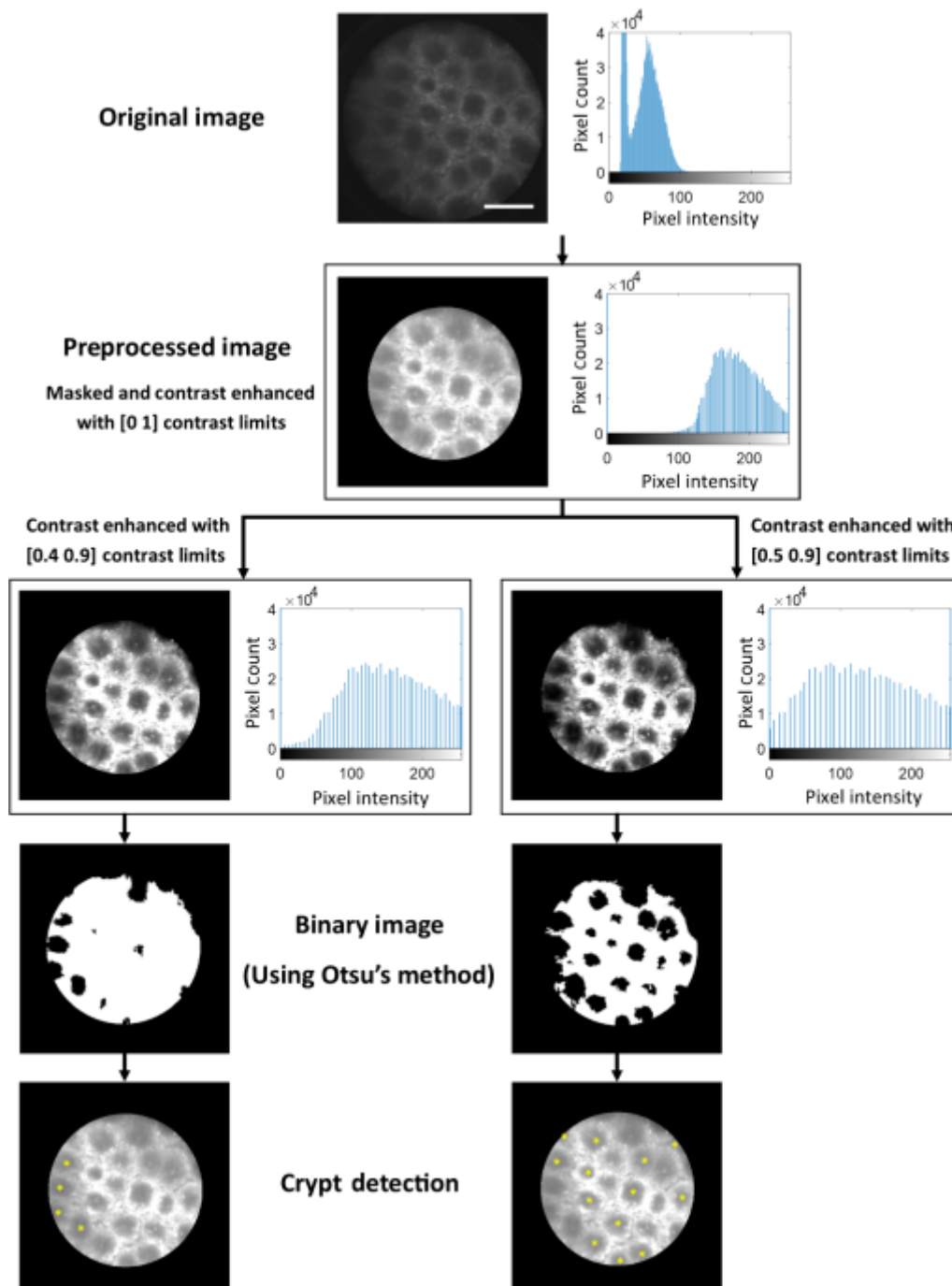
Figure 9. Comparison of image histograms and crypt detection using different contrast limit pairs. Contrast enhancement requires a lower and an upper contrast limit; three contrast limit pairs are shown here [0 1], [0.4 0.9], and [0.5 0.9]. The algorithm did not detect any crypts when using the original image, nor the preprocessed image. Note that the image that was contrast enhanced using the [0.4 0.9] contrast limits detects crypts missed by the [0.5 0.9] contrast limits, thereby increasing the sensitivity of the algorithm with the combination of multiple contrast limit pairs. Scale bar is 250μm.

To determine the optimal combination of contrast limit pairs for image segmentation, we iteratively increased the values of the lower and upper contrast limits by 10% (Fig. 10). There were 36 contrast limit pairs in the range from [0.1 0.2] to [0.8 0.9]. Due to extremely low crypt detection sensitivity in images with [0 1] contrast limits, the lower contrast limit 0 and the upper contrast limit 1 were excluded from testing.

Upper contrast limit

Lower contrast limit	0.2	0.3	0.4	0.5	0.6	0.7	0.8	0.9
0.1	0.1 0.2	0.1 0.3	0.1 0.4	0.1 0.5	0.1 0.6	0.1 0.7	0.1 0.8	0.1 0.9
0.2		0.2 0.3	0.2 0.4	0.2 0.5	0.2 0.6	0.2 0.7	0.2 0.8	0.2 0.9
0.3			0.3 0.4	0.3 0.5	0.3 0.6	0.3 0.7	0.3 0.8	0.3 0.9
0.4				0.4 0.5	0.4 0.6	0.4 0.7	0.4 0.8	0.4 0.9
0.5					0.5 0.6	0.5 0.7	0.5 0.8	0.5 0.9
0.6						0.6 0.7	0.6 0.8	0.6 0.9
0.7							0.7 0.8	0.7 0.9
0.8								0.8 0.9

Figure 10. Schematic of intensity contrast limit combinations tested for crypt segmentation. Contrast enhancement scales image intensity values (0 to 255) between 0 and 1, scale bar is 250 μm. Both upper and lower contrast limits were iteratively increased by 10% to cover a range from [0.1 0.2] to [0.8 0.9]. Gray region depicts unusable contrast limit pairs.

A training data set comprising 100 images, acquired from porcine colorectal mucosa, was used to assess the ideal intensity contrast limit pairs to optimize crypt segmentation sensitivity. All 36 upper / lower contrast limit combinations were applied to each image, and the sensitivity and PPV of each contrast limit pair was calculated using the number of true positive, false positive, and false negative crypts detected, as compared to manual inspection of the image. Fivefold cross-validation was used to define test and training sets; one fifth of the data was set

82

aside as the test set, and the remaining four fifths were used to train the algorithm. The algorithm selected the best contrast limits using the training set, and then those contrast limits were applied to the test set to calculate crypt detection sensitivity. This was repeated four additional times, so that each of the five groups served as a test set, and resulting output displayed the selected contrast limits and the average sensitivity of the five test sets. The fivefold cross-validation algorithm was repeated 10 times, with the random assignment of images yielding slightly varying sensitivity averages. Sensitivities of several combinations of contrast limit pairs were also calculated using the fivefold cross-validation algorithm; selection of these combinations is described in Sec. 3.1. The average sensitivity, and standard deviation, of each selected contrast limit pair and combination was tabulated.

2.6.2. Iterative contrast limits and automated crypt identification, segmentation, and morphology quantification

Using the optimal contrast limit pair combinations (determined using the previously described process), porcine and human preprocessed (masked and contrast-enhanced as previously described) individual images and human image mosaics were quantified with QFEA. The quality control step was not used for the initial analysis, of all porcine and human images, in order to determine the optimal QR exclusion value. The QFEA contained the list of selected contrast limit pairs, and passed an image and first set of contrast limits to a quantification subroutine that returned the coordinates of centroids located, and calculated crypt area and circularity. These steps were repeated iteratively (see loop in Fig. 8) with five different pairs of contrast limits, to increase the sensitivity of QFEA. The last step was to save the quantified data and display the centroids (last step in Fig. 8).

Using the optimal contrast limit pair combinations selected after fivefold cross-validation of the crypt segmentation algorithm, as described in Sec. 2.6.1, each of the porcine (100) and human (39) preprocessed images were converted into a binary image, using a variable threshold determined by Otsu's method [31], choosing a threshold that minimizes the variance of black (value 0) and white (value 1) pixels. The binary image was then eroded, with a disk structuring element of 5 pixels radius. Erosion, in short, changes binary values to 0 unless the structuring element, in this case the disk, overlaps only with binary values of 1 when translated to different positions [32]. Since we are quantifying circularity of relatively circular crypts, our structuring element is necessarily round and of a radius of 5 pixels since our individual fibers are ~5 pixels in diameter.

The resulting binary image was then inverted, with all 1 values converted to 0, and all 0 values converted to 1, and remasked using the field-of-view (FOV) binary image, to ensure that the crypts are the value-1 binary shapes. Holes were then closed, where if a region of value 0 is completely enclosed by value-1 pixel, the region is converted into value-1s as well. The resulting shapes were once more eroded with a disk (5 pixels radius), and the coordinates of centroids of detected shapes were extracted, hereafter referred to as crypts, as well as each crypt's area and circularity. The centroid for each crypt is the coordinates for the center of mass of each shape. In the eroded binary image, each crypt is defined as a group of continuous value-1 pixel, and the centroid is determined as the average of those pixel positions based on the equations

(1)
$$C_x = \sum_{i=1}^{n} X_i,$$

(2)
$$C_y = \sum_{i=1}^{n} Y_i,$$

where C is the centroid coordinate, (x,y) is the position of a value-1 pixel, and n is the number of

value-1 pixels in the crypt [33]. Crypt area was quantified as the actual number of pixels in the

shape (binary value of 1, in this case). The circularity was calculated using

(3) $$Circularity = \frac{4\pi A}{P^2},$$

where A is the area in pixels and P is the perimeter, and a perfect circle has a circularity of 1.

After extracting crypt area, crypt circularity, each crypt was quality controlled to exclude those

larger than 100,000 pixels in area or smaller than 500 pixels in area (areas outside the range of

crypt sizes based on trained observer quantification), or if the circularity was <0.5. This

exclusion eliminated many shapes that were incorrectly labeled as crypts by the iterative contrast

enhancement and erosion steps. Finally, each coordinate was compared against the array of the

previous contrast limit pairs' centroid coordinates (if applicable), and if any two coordinates

were at a distance closer than 50 pixels, they were considered duplicates and the duplicate

centroid data were not stored. The resulting arrays of crypt area, circularity, and centroid

coordinates, as well as the FOV, were returned to the main function.

2.6.3. Image stack preparation and mosaicking

As described in Sec. 2.4, consecutive images were acquired by slowly dragging the distal

end over the epithelial surface for subsequent processing into mosaics. To develop a mosaic

image, images from each location (image stack) were cleared of duplicates and images with

obvious motion blur. The remaining images in the stack were then preprocessed by masking and

contrast enhancement, as described in Sec. 2.5. The image stacks were then stitched together; our

mosaics consisted of four to six consecutive images stitched together for a final FOV ranging 3

to 5 mm in length and ~0.7mm in height. Mosaics were created from individual images using a

modified version of an existing algorithm [31], which requires manual input to select pairs of

matching points on two adjacent images, and then uses bilinear interpolation to assign appropriate intensity values in spaces created by stretching or shrinking the second image to match the selected coordinates. Once image stacks were converted into a mosaic, they were treated the same way as a preprocessed individual image and subject to the image segmentation algorithm (QFEA).

3. Results

Individual mages for this manuscript were acquired from histologically normal regions of human and porcine colorectal tissue, as described in Secs. 2.2 and 2.3. One hundred individual images were acquired from porcine colorectal mucosa as an algorithm training data set and were used in the selection of the best five contrast limit pairs for image segmentation. Thirty-nine images of human epithelial tissue used for automated sensitivity quantification were acquired from clinically normal regions surrounding grossly visible tumors, in excised tissue of eight patients, five diagnosed with invasive colonic adenocarcinoma, two with invasive rectal adenocarcinoma, and one with tubular adenoma. Images of human epithelial tissue used for image mosaicking included both normal and abnormal regions in the same excised tissue of eight patients. All porcine (100) and human (39) images were used for calculating the relationship between average image sensitivity and the QR ratio metric, and determining the optimal QR exclusion threshold value. The images with passing QR were used for quantification of human crypt features in a pilot study, and each individual crypt, as identified by QFEA, was considered a separate data point for quantitative comparison. This comparison is not comprehensive, considering our small sample size, but it shows the ability of QFEA to distinguish variations in crypt size and circularity. A few mosaics were also qualitatively described, as well as subject to the image segmentation and quantification algorithm as proof-of-concept.

3.1. Selection of Optimal Contrast Limits for Image Segmentation, Using Porcine Image Test Data Set

For improved crypt detection sensitivity during image segmentation, optimal contrast limit pair combinations were selected using fivefold cross-validation, as described in Sec. 2.6.1. The average sensitivity at each of the 36 contrast limit pairs (Fig. 10) is shown in Fig. 11(a) as a heatmap, with color corresponding to the average percent sensitivity at each contrast limit pair. As described previously, multiple contrast limit pairs increase the sensitivity of QFEA. Figure 11(b) shows the average of the contrast limits with the highest test sensitivity (labeled in Fig. 11 as "1"), as calculated via fivefold cross validation, as well as the average and standard deviation of various combinations of contrast limit pairs. Figure 11(a) shows "1" as the contrast limit pair with the highest stand-alone sensitivity and "2" as the contrast limit pair with the second highest sensitivity; combining contrast limit pairs with the same lower contrast limit (contrast limits labeled "1" and "2" both have a lower contrast limit of 0.5) does not yield as large of an increase in overall sensitivity of the QFEA as combining the best contrast limit pair from each row/lower contrast limit (contrast limits labeled "1" and "3"). As seen in Fig. 11(b), combining the two contrast limit pairs with the highest sensitivity increases the overall test sensitivity by <15%, but combining two contrast limit pairs with different lower contrast limits [from different rows in Fig. 11(a)] yields an increase in overall sensitivity of over 35%. A combination of five contrast limit pairs, the highest sensitivity from each row (lower contrast limit) from 0.2 to 0.7, yielded the highest overall test sensitivity [Fig. 11(b)] before a plateau in performance. While adding more than five contrast limit pairs might slightly increase the average reported sensitivity of QFEA, there is the risk of overtraining the algorithm to be too specific to the training set.
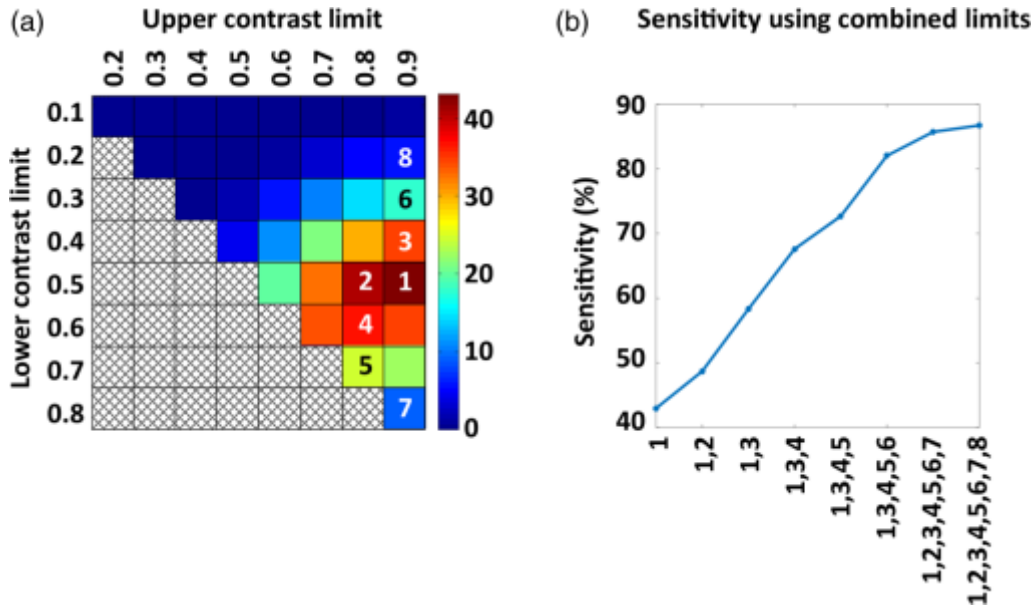
Figure 11. (a) Heatmap of the average percent sensitivity for each contrast limit pair; colorbar is percent sensitivity. As with Fig. 10, the xx-axis displays the upper contrast limit, and the y-axis displays the lower contrast limit. (b) Average test sensitivity, after 10 iterations of fivefold cross-validation, for each contrast limit pair or combination of contrast limit pairs. Maximum standard deviation among all points was <0.61%. Heatmap (a) has numbered the contrast limit pairs selected for average sensitivity calculation, for clear correlation to the x-axis in plot (b).

3.2. Quantitative Quality Ratio and Crypt Detection Sensitivity of the Image Segmentation Algorithm

All porcine (100) and human (39) microendoscopy images were quantified (QFEA) using the five contrast limit pairs selected in Sec. 3.1. The quantitative image quality control algorithm, described previously, yielded a global QR metric (peak-to-trough ratio) per image, and this average ratio was tabulated along with the crypt detection sensitivity of QFEA, for each image. In Fig. 12(a), the sensitivities and PPVs of images with a QR value equal to, or higher than, the specified QR value (x-axis) were averaged for an aggregate average sensitivity at that QR. The peak aggregate sensitivity, before the decline, was at a QR value of 1.07 [Fig. 12(a)]. Therefore, a QR value of 1.07 was selected as the image quality control threshold, excluding for

quantification any images with a QR of <1.07. QR values >1.1 used <10 images for average sensitivity calculation, and are not reliable indicators.
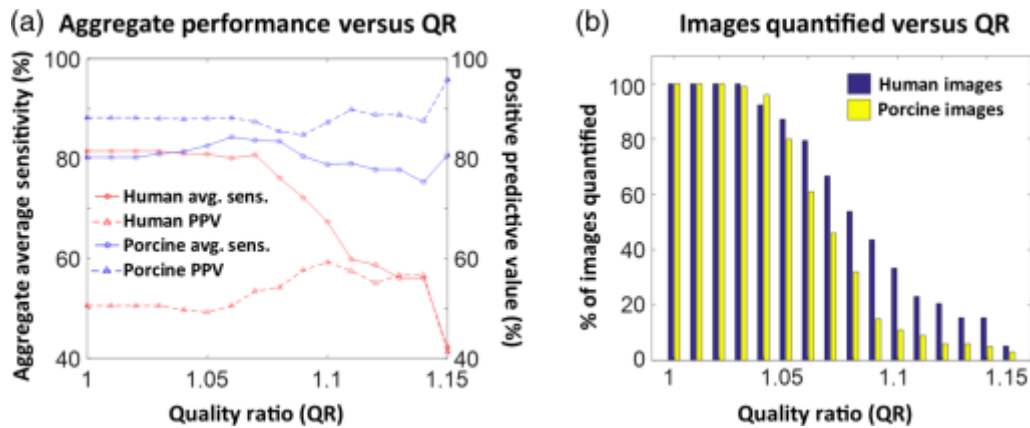

Figure 12. (a) Average sensitivity and PPV of the QFEA crypt detection versus the average QR of images; aggregate performance plotted against QR was calculated using images with QR values equal to or higher to the QR labeled in the x-axis. (b) Number of images with QR values equal to or higher than the labeled QR values.

3.3. Pilot Study of Quantified Crypt Morphology

Quantified crypt data were compared between images of surrounding grossly appearing normal regions in patients grouped as case 1 or case 2; case 1 were patients diagnosed with invasive adenocarcinoma and case 2 were patients diagnosed with tubular adenoma. For individual images, crypt area and circularity were significantly greater for the case 2 group than the case 1 group. The tabulated area and circularity, displayed in Fig. 13 in arbitrary units, were divided by the maximum data value in area and circularity, respectively. A total number of 10 images with 219 cumulative identified crypts were used for case 1, and nine images with 219 cumulative identified crypts for case 2. A two-tailed Student t-test yielded pp values of <0.01 for the area, and <0.005 for the circularity.

89
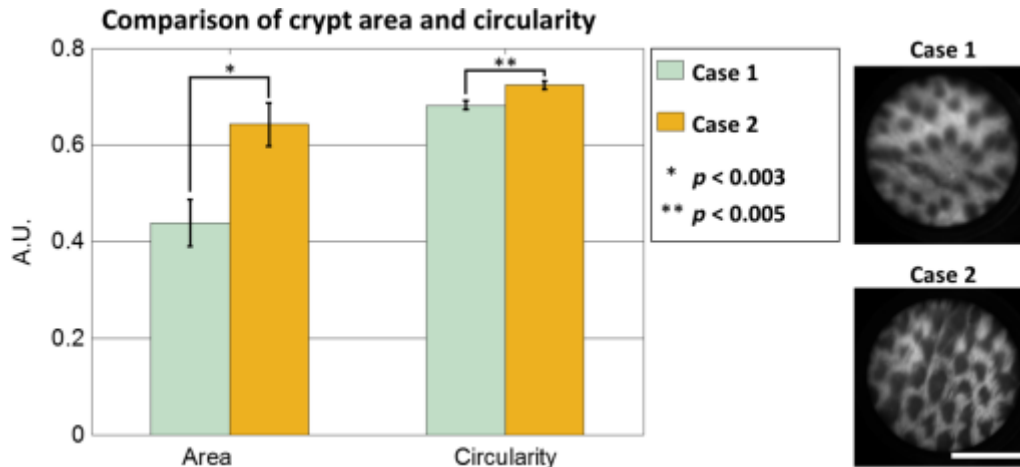
Figure 13. Comparison of image features in individual microendoscopic images of clinically normal tissue in patients grouped as case 1 and case 2. Case 1 had an adjacent region diagnosed as invasive adenocarcinoma and case 2 had an adjacent region diagnosed as tubular adenoma. Error bars denote standard error, and p values were calculated using two-tailed Student t test. Microendoscopy images on the right are examples of quantified images. Scale bar is 0.5 mm.

## 3.4. Qualitative Image Analysis and Automated Crypt Identification of Mosaics

Mosaics were created from consecutive fields of view to demonstrate the ability to improve the inherently small field of view in fiber bundle microendoscopy images, and the image segmentation and quantification algorithm was applied to them to determine if quantification of the mosaics using our algorithm was viable. Figure 14 shows a qualitative comparison of image mosaics acquired from both normal and dysplastic regions of colonic epithelium. The original images were acquired over 10 s, and the new FOV was ∼3.5mm long and 0.7 mm wide for both mosaics. The mosaics comprise five individual consecutive images. Normal tissue [Fig. 14(a)] has regularly spaced crypts, surrounded by a pericryptal sheath, demonstrated here as a bright ring enclosing the luminal compartment (see yellow arrow). Neoplastic tissue [Fig. 14(b)] oftentimes demonstrates irregularly shaped crypts that are haphazardly arranged, and the yellow arrows point to crypts that have uneven ring structures

90

enclosing them. The crypt detection sensitivity, when applied to the mosaics in Fig. 14, was 70% [Fig. 14(b)] or higher [Fig. 14(a)].
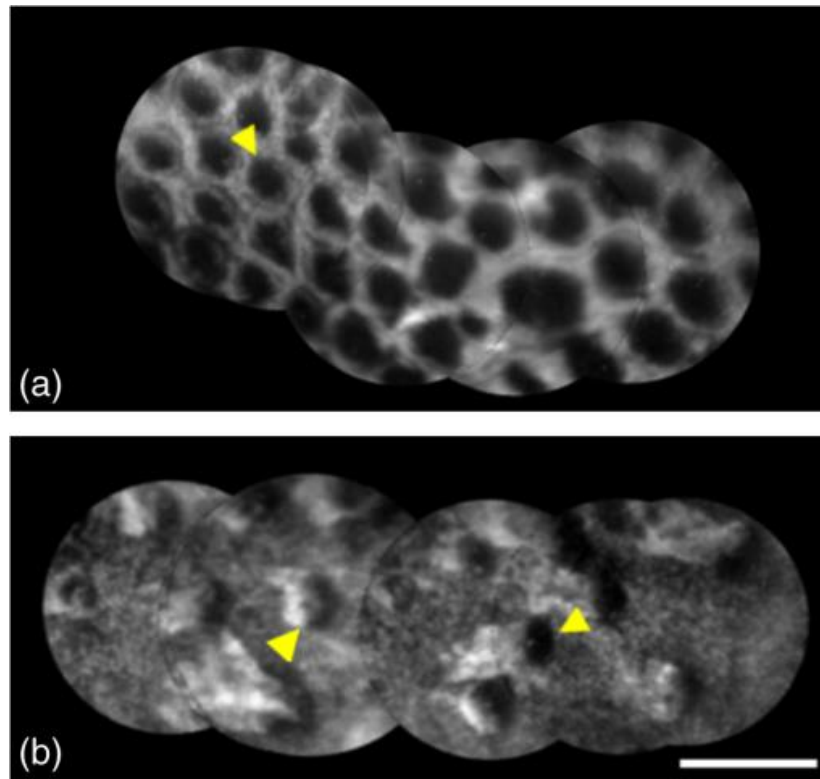
Figure 14. Image mosaics showing (a) normal colon and (b) invasive adenocarcinoma. Yellow arrows point to crypts. Images have enhanced contrast and brightness for publishing. Scale bar is 0.5 mm.

Figure 15 shows an occult hyperplastic polyp in otherwise normal-appearing tissue, ~1mm in diameter, whose relative size and morphology was highlighted by mosaicking. A stack of eight images was mosaicked using the method stated previously, with the yellow arrows [Fig. 15(a)] pointing to the edges of the hyperplastic polyp ~1mm in diameter. The imaged region was ~3mm in length and 0.7 mm in width—the yellow arrows on gross tissue [Fig. 15(b)] point to the edges of the imaged region. The white arrow [Fig. 15(b)] points to the grossly visible tumor, which was ~4cm to the right of the hyperplastic polyp [yellow arrows, Fig. 15(b)].
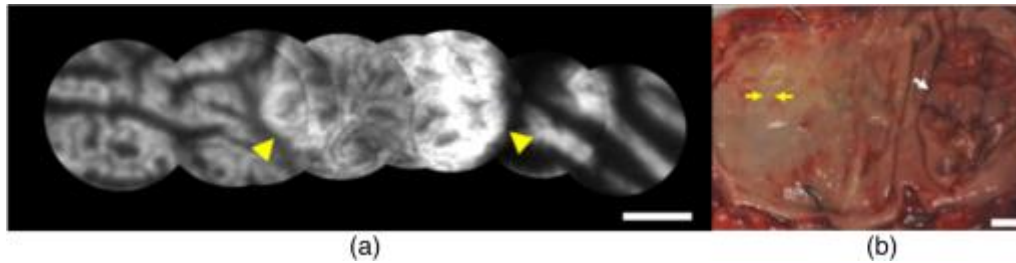
Figure 15. Example of occult dysplasia. (a) Image mosaic showing a hyperplastic polyp. Yellow arrows point to edges of hyperplastic polyp. Scale bar is 0.5 mm. (b) Context image showing gross view of colon epithelium and location of image mosaic at left. Yellow arrows point to mosaic endpoints (~3mm). White arrow points to cancerous region (invasive colonic adenocarcinoma). Scale bar is 10 mm. Images have enhanced contrast and brightness for publishing.

4. Discussion

Fiber bundle microendoscopy images of *ex vivo* colorectal epithelium contain useful quantitative data that may be used to assess the tissue microstructure for evidence of occult dysplasia. In this paper, we have described QFEA, an approach to automated quantification of important features of colorectal epithelial microstructure from microendoscopy image data. One hundred images of normal porcine tissue were used to select, via fivefold cross-validation, the best contrast limit pair combinations for crypt detection sensitivity. In addition, we have also demonstrated a method to automatically calculate, and exclude, images with low signal-to-background ratios (QR) in order to filter and remove images that may yield unreliable quantitative data. In clinical settings, the fiber bundle microendoscopy imaging system used in this study may acquire image data via manual placement of the probe directly into the epithelial surface, or remote placement onto tissue during an endoscopic procedure. In both of these applications, significant image quality variability may occur. The majority of the images demonstrated a crypt detection sensitivity of >80% following analysis via QFEA, indicating potentially reliable calculation of quantitative reporters of tissue microstructure.

A combination of contrast limit pairs was tested with the porcine image data set to determine the best parameters for high crypt detection sensitivity. While the contrast limits were iteratively increased by 10%, it is likely that smaller step increases would have provided increased overall sensitivity. A larger data set would be required to test if smaller iterative increases and contrast limit selection would generalize for microendoscopy images, or if the algorithm would be overtrained. The crypt identification algorithm, using the selected combination of contrast limit pairs, was then applied to both porcine and human images, to determine the aggregate performance when excluding images with low QR (Fig. 12). As seen in Fig. 12(b), the number of images, both porcine and human, with QR values >1.1 drops below 20, decreasing sample size and leading to undersampling bias in the calculated sensitivities at those values. Figure 12(a) reveals that the PPV of human images is drastically lower than that of the porcine image set. We believe this is due to a more carefully controlled imaging procedure with the porcine tissue, since image quality of human tissue is influenced by variations in human preoperative procedures, and sample handling by clinicians and staff. Potential alternatives to improve image quality include alternative contrast agent or optical sectioning techniques such as structured illumination [34].

A pilot comparison of quantified crypt morphology (Sec. 3.3) demonstrated the ability of our quantitative image quality control and image feature extraction algorithm (QFEA) to detect minor differences between two otherwise clinically normal appearing colorectal tissue specimens. While a conclusive statement cannot be made based on image data from eight human patients, it does suggest that an algorithm such as QFEA can quantify crypt features objectively and without significant user input. Similarly, no definite quantitative statements can be made for image mosaics, until a larger data set is acquired. Qualitative inspection of the image mosaics

93

shows them as a viable method for overcoming the FOV size limitations of microendoscopy, while image segmentation of the mosaics shows the potential applicability of QFEA to mosaicked images.

In vivo inspection of gastrointestinal mucosa using high-resolution microendoscopy methods has been previously shown to yield clinically useful data. Recent studies examining manual inspection of microendoscopy images of known diagnoses have demonstrated strong interobserver agreement, indicating that well-trained clinicians should be able to effectively incorporate these methods into clinical practice [21]. Qualitative assessment of these images by a highly trained observer is likely to continue to yield clinically relevant data, but widespread adoption of high-resolution, *in vivo*, microendoscopy methods for improved detection of occult dysplasia remains a challenge. A user-independent method of image analysis could provide additional data to make an informed decision and reduce the burden of training required for the clinician at the point-of-care. The introduction of an image analysis algorithm like QFEA into computer-aided diagnostic methods may yield useful complementary data to make improved clinical decisions. In our pilot study, QFEA demonstrates an ability to detect minor differences between two otherwise clinically normal appearing colorectal tissue specimens, suggesting that discriminative quantitative crypt features can be measured objectively and without significant user input.

Computer-aided diagnostic approaches have been of significant research interest in myriad cancer detection approaches, including imaging. Automated quantitative classification has been applied to breast cancer detection using ultrasound images, digitized mammograms, and histopathology, ovarian cancer detection using matrix-assisted laser desorption/ionization imaging mass spectrometry, and prostate cancer grading using ultrasound images and

histopathology [35-40]. Quantitative classification based on microendoscopy image texture features in Barrett's esophagus and esophageal squamous cell carcinoma, specifically gray-level co-occurrence matrices, has been previously investigated [41-43]. A recent publication on automated selection of high-quality frames in microendoscopic images [44] points to both the need for quality control, as well as the viability of automated extraction of high-quality frames during video-rate acquisition. Ongoing development work with microendoscopic systems may enable spectroscopic data to be used in conjunction with quantitative image features, such as those described in this paper [45]. This quantitative data, coupled with extracted image-based features provided by algorithms such as QFEA, could lead to the adoption of standardized, objective methods of *in vivo* high-resolution microendoscopy image interpretation and analysis.

In conclusion, the methods described here provide insight into the ability of fiber bundle based high-resolution microendoscopy imaging tools to yield clinically relevant data about the tissue microstructure in colorectal epithelium. Effective clinical translation and application of any quantitative image analysis tools applied to this imaging method will need to account for some unavoidable image quality variation, particularly for *in vivo* endoscopic application of the device on living, constantly moving tissue. Quantitative assessment and control of high-resolution image quality is essential to ensuring reliable results in any future objective, computer-aided diagnostic algorithm development.

References

[1] S. P. Prieto, A. J. Powless, K. Lai, J. A. Laryea, J. S. Mizell and T. J. Muldoon, "Qualitative and quantitative comparison of colonic microendoscopy image features to histopathology," in *SPIE BiOS,* 2015, pp. 93280B-93280B-8.

[2] Centers for Disease Control and Prevention (CDC), "Vital signs: Colorectal cancer screening, incidence, and mortality--United States, 2002-2010," *MMWR Morb. Mortal. Wkly. Rep.,* vol. 60, *(26),* pp. 884-889, Jul 8, 2011.

[3] M. J. Pomeranz and S. S. Stahl, "A correlative study of cytodiagnosis and biopsy," Oral Surgery, Oral Medicine, Oral Pathology, vol. 6, (8), pp. 1026-1031, 1953.

[4] L. Bujanda, A. Cosme, I. Gil and J. I. Arenas-Mirave, "Malignant colorectal polyps," World J. Gastroenterol., vol. 16, (25), pp. 3103-3111, Jul 7, 2010.

[5] S. Kudo and H. Kashida, "Flat and depressed lesions of the colorectum," Clinical Gastroenterology and Hepatology, vol. 3, (7), pp. S33-S36, 2005.

[6] M. Fleming, S. Ravula, S. F. Tatishchev and H. L. Wang, "Colorectal carcinoma: Pathologic aspects," Journal of Gastrointestinal Oncology, vol. 3, (3), pp. 153, 2012.

[7] M. Kobayashi, H. Tajiri, E. Seike, M. Shitaya, S. Tounou, M. Mine and K. Oba, "Detection of early gastric cancer by a real-time autofluorescence imaging system," Cancer Lett., vol. 165, (2), pp. 155-159, 2001.

[8] H. Machida, Y. Sano, Y. Hamamoto, M. Muto, T. Kozu, H. Tajiri and S. Yoshida, "Narrow-band imaging in the diagnosis of colorectal mucosal lesions: a pilot study," Endoscopy, vol. 36, (12), pp. 1094-1098, Dec, 2004.

[9] M. A. Kara, F. P. Peters, W. D. Rosmolen, K. K. Krishnadath, F. J. ten Kate, P. Fockens and J. J. Bergman, "High-resolution endoscopy plus chromoendoscopy or narrow-band imaging in Barrett's esophagus: a prospective randomized crossover study," Endoscopy, vol. 37, (10), pp. 929-936, Oct, 2005.

[10] W. L. Curvers, R. Singh, L. M. Song, H. C. Wolfsen, K. Ragunath, K. Wang, M. B. Wallace, P. Fockens and J. J. Bergman, "Endoscopic tri-modal imaging for detection of early neoplasia in Barrett's oesophagus: a multi-centre feasibility study using high-resolution endoscopy, autofluorescence imaging and narrow band imaging incorporated in one endoscopy system," Gut, vol. 57, (2), pp. 167-172, Feb, 2008.

[11] P. Hsiung, J. Hardy, S. Friedland, R. Soetikno, C. B. Du, A. P. Wu, P. Sahbaie, J. M. Crawford, A. W. Lowe and C. H. Contag, "Detection of colonic dysplasia in vivo using a targeted heptapeptide and confocal microendoscopy," Nat. Med., vol. 14, (4), pp. 454-458, 2008.

[12] P. M. Lane, S. Lam, A. McWilliams, M. W. Anderson and C. E. MacAulay, "Confocal fluorescence microendoscopy of bronchial epithelium," J. Biomed. Opt., vol. 14, (2), pp. 024008-024008-10, 2009.

[13] K. B. Dunbar, P. Okolo, E. Montgomery and M. I. Canto, "Confocal laser endomicroscopy in Barrett's esophagus and endoscopically inapparent Barrett's neoplasia: a prospective, randomized, double-blind, controlled, crossover trial," Gastrointest. Endosc., vol. 70, (4), pp. 645-654, 2009.

[14] M. Goetz, A. Hoffman, P. R. Galle, M. F. Neurath and R. Kiesslich, "Confocal laser endoscopy: new approach to the early diagnosis of tumors of the esophagus and stomach," 2006.

[15] H. Shin, M. C. Pierce, D. Lee, H. Ra, O. Solgaard and R. Richards-Kortum, "Fiber-optic confocal microscope using a MEMS scanner and miniature objective lens," Optics Express, vol. 15, (15), pp. 9113-9122, 2007.

[16] W. Piyawattanametha and T. D. Wang, "MEMS-based dual-axes confocal microendoscopy," Selected Topics in Quantum Electronics, IEEE Journal Of, vol. 16, (4), pp. 804-814, 2010.

[17] H. Bao, J. Allen, R. Pattie, R. Vance and M. Gu, "Fast handheld two-photon fluorescence microendoscope with a 475 μm× 475 μm field of view for in vivo imaging," Opt. Lett., vol. 33, (12), pp. 1333-1335, 2008.

[18] G. D. De Palma, "Confocal laser endomicroscopy in the "in vivo" histological diagnosis of the gastrointestinal tract," World J. Gastroenterol., vol. 15, (46), pp. 5770-5775, Dec 14, 2009.

[19] R. Kiesslich, J. Burg, M. Vieth, J. Gnaendiger, M. Enders, P. Delaney, A. Polglase, W. McLaren, D. Janell and S. Thomas, "Confocal laser endoscopy for diagnosing intraepithelial neoplasias and colorectal cancer in vivo," Gastroenterology, vol. 127, (3), pp. 706-713, 2004.

[20] D. P. Hurlstone, S. S. Cross, I. Adam, A. J. Shorthouse, S. Brown, D. S. Sanders and A. J. Lobo, "A prospective clinicopathological and endoscopic evaluation of flat and depressed colorectal lesions in the United Kingdom," Am. J. Gastroenterol., vol. 98, (11), pp. 2543-2549, 2003.

[21] N. D. Parikh, D. Perl, M. H. Lee, B. Shah, Y. Young, S. S. Chang, R. Shukla, A. D. Polydorides, E. Moshier and J. Godbold, "In vivo diagnostic accuracy of high-resolution microendoscopy in differentiating neoplastic from non-neoplastic colorectal polyps: a prospective study," Am. J. Gastroenterol., vol. 109, (1), pp. 68-75, 2014.

[22] L. L. Levy, P. M. Vila, R. W. Park, R. Schwarz, A. D. Polydorides, M. S. Teng, V. V. Gurudutt, E. M. Genden, B. Miles and S. Anandasabapathy, "High-Resolution Optical Imaging of Benign and Malignant Mucosa in the Upper Aerodigestive Tract: An Atlas for Image-Guided Surgery," ISRN Minimally Invasive Surgery, vol. 2012, 2012.

[23] S. Srivastava, J. J. Rodríguez, A. R. Rouse, M. A. Brewer and A. F. Gmitro, "Computer-aided identification of ovarian cancer in confocal microendoscope images," J. Biomed. Opt., vol. 13, (2), pp. 024021-024021-13, 2008.

[24] H. L. Fu, J. L. Mueller, M. P. Javid, J. K. Mito, D. G. Kirsch, N. Ramanujam and J. Q. Brown, "Optimization of a widefield structured illumination microscope for non-destructive assessment and quantification of nuclear features in tumor margins of a primary mouse model of sarcoma," PloS One, vol. 8, (7), pp. e68868, 2013.

[25] S. Karkanis, D. K. Iakovidis, D. E. Maroulis, D. Karras and M. Tzivras, "Computer-aided tumor detection in endoscopic video using color wavelet features," Information Technology in Biomedicine, IEEE Transactions On, vol. 7, (3), pp. 141-152, 2003.

[26] X. Wang, S. Ghosh and S. W. Guo, "Quantitative quality control in microarray image processing and data acquisition," Nucleic Acids Res., vol. 29, (15), pp. E75-5, Aug 1, 2001.

[27] N. Bedard, T. Quang, K. Schmeler, R. Richards-Kortum and T. S. Tkaczyk, "Real-time video mosaicing with a high-resolution microendoscope," Biomed. Opt. Express, vol. 3, (10), pp. 2428-2435, 10/01, 2012.

[28] T. J. Muldoon, M. C. Pierce, D. L. Nida, M. D. Williams, A. Gillenwater and R. Richards-Kortum, "Subcellular-resolution molecular imaging within living tissue by fiber microendoscopy," Optics Express, vol. 15, (25), pp. 16413-16423, 2007.

[29] J. A. Izatt, M. D. Kulkarni, H. Wang, K. Kobayashi and M. V. Sivak Jr, "Optical coherence tomography and microscopy in gastrointestinal tissues," Selected Topics in Quantum Electronics, IEEE Journal Of, vol. 2, (4), pp. 1017-1028, 1996.

[30] Y. Nakai, S. Shinoura, A. Ahluwalia, A. Tarnawski and K. Chang, "Molecular imaging of epidermal growth factor-receptor and survivin in vivo in porcine esophageal and gastric mucosae using probe-based confocal laser-induced endomicroscopy: proof of concept." Journal of Physiology and Pharmacology: An Official Journal of the Polish Physiological Society, vol. 63, (3), 2012.

[31] N. Otsu, "A threshold selection method from gray-level histograms," Automatica, vol. 11, (285-296), pp. 23-27, 1975.

[32] P. Soille, Morphological Image Analysis: Principles and Applications. Springer Science & Business Media, 2013.

[33] M. K. Cheezum, W. F. Walker and W. H. Guilford, "Quantitative comparison of algorithms for tracking single fluorescent particles," Biophys. J., vol. 81, (4), pp. 2378-2388, 2001.

[34] T. Tkaczyk, M. Rahman, V. Mack, K. Sokolov, J. Rogers, R. Richards-Kortum and M. Descour, "High resolution, molecular-specific, reflectance imaging in optically dense tissue phantoms with structured-illumination," Optics Express, vol. 12, (16), pp. 3745-3758, 2004.

[35] H. Cheng, J. Shan, W. Ju, Y. Guo and L. Zhang, "Automated breast cancer detection and classification using ultrasound images: A survey," Pattern Recognit, vol. 43, (1), pp. 299-317, 2010.

[36] Z. Huo, M. L. Giger, C. J. Vyborny, D. E. Wolverton, R. A. Schmidt and K. Doi, "Automated computerized classification of malignant and benign masses on digitized mammograms," Acad. Radiol., vol. 5, (3), pp. 155-168, 1998.

[37] S. Doyle, S. Agner, A. Madabhushi, M. Feldman and J. Tomaszewski, "Automated grading of breast cancer histopathology using spectral clustering with textural and architectural image features," in Biomedical Imaging: From Nano to Macro, 2008. ISBI 2008. 5th IEEE International Symposium On, 2008, pp. 496-499.

[38] J. O. Gustafsson, M. K. Oehler, A. Ruszkiewicz, S. R. McColl and P. Hoffmann, "MALDI Imaging Mass Spectrometry (MALDI-IMS)—Application of Spatial Proteomics for Ovarian Cancer Classification and Diagnosis," International Journal of Molecular Sciences, vol. 12, (1), pp. 773-794, 2011.

[39] W. D. Richard and C. G. Keen, "Automated texture-based segmentation of ultrasound images of the prostate," Comput. Med. Imaging Graphics, vol. 20, (3), pp. 131-140, 1996.

[40] S. Doyle, M. Hwang, K. Shah, A. Madabhushi, M. Feldman and J. Tomas, "Automated grading of prostate cancer using architectural and textural image features," in Biomedical Imaging: From Nano to Macro, 2007. ISBI 2007. 4th IEEE International Symposium On, 2007, pp. 1284-1287.

[41] T. J. Muldoon, N. Thekkek, D. Roblyer, D. Maru, N. Harpaz, J. Potack, S. Anandasabapathy and R. Richards-Kortum, "Evaluation of quantitative image analysis criteria for the high-resolution microendoscopic detection of neoplasia in Barrett's esophagus," J. Biomed. Opt., vol. 15, (2), pp. 026027-026027-7, 2010.

[42] T. J. Muldoon, D. Roblyer, M. D. Williams, V. M. Stepanek, R. Richards–Kortum and A. M. Gillenwater, "Noninvasive imaging of oral neoplasia with a high-resolution fiber-optic microendoscope," Head Neck, vol. 34, (3), pp. 305-312, 2012.

[43] D. Shin, M. Protano, A. D. Polydorides, S. M. Dawsey, M. C. Pierce, M. K. Kim, R. A. Schwarz, T. Quang, N. Parikh and M. S. Bhutani, "Quantitative analysis of high-resolution microendoscopic images for diagnosis of esophageal squamous cell carcinoma," Clinical Gastroenterology and Hepatology, vol. 13, (2), pp. 272-279. e2, 2015.

[44] A. Ishijima, S. Mondrik, R. A. Schwarz, N. Vigneswaran, A. M. Gillenwater and R. Richards-Kortum, "Automated frame selection process for analyzing high resolution microendoscope images," in SPIE Translational Biophotonics, 2014, pp. 91551M-91551M-4.

[45] G. J. Greening, A. J. Powless, J. A. Hutcheson, S. P. Prieto, A. A. Majid and T. J. Muldoon, "Design and validation of a diffuse reflectance and spectroscopic microendoscope with poly (dimethylsiloxane)-based phantoms," in SPIE BiOS, 2015, pp. 93320R-93320R-7.

Chapter IV: **Fluorescein as a topical fluorescent contrast agent for quantitative**

microendoscopic inspection of colorectal epithelium [1]

1. Introduction

Microendoscopy is an emerging method which can provide clinicians with in vivo

information on tissue microstructure that is not readily visible using traditional colonoscopy and

endoscopy. It allows for histology-level detail to be acquired in real-time, with the potential for

in vivo guidance for the clinician, such as in targeted biopsies [2, 3]. Myriad microendoscopic

imaging modalities have been applied to various tissues, including ovarian, esophageal, bladder,

colonic, and oral epithelium [3-8]. We have chosen to investigate colorectal cancer, as it is

currently the second leading cause of cancer deaths in the United States [9]. The precursor of

colorectal malignancy is dysplasia and there is a long lag phase between the onset of dysplasia,

and the development of malignancy [10]. Detecting these regions prior to becoming clinically

evident will further help in preventing colorectal cancer [11]. In addition, patients with

inflammatory bowel disease (IBD), who are frequently screened for dysplastic regions, would

likely also benefit from early detection of suspicious lesions [12]. Several microendoscopy

imaging studies are aimed at improving early detection of glandular epithelial dysplasia, and

providing biopsy guidance and prognostic indicators in clinical settings [3, 13-15].

Currently described microendoscopic methods for in vivo imaging of gastrointestinal

epithelium vary, including integration of the probe into conventional endoscopes [13], fiber

bundle confocal systems for increased depth penetration [2], and portable wide field end-on fiber

bundle approaches such as a previously developed system [5]. End-on fiber bundle systems, such

as the one used in this manuscript, are designed to come into direct contact with the tissue, and

image acquired is either of the tissue directly in contact with the distal end of the probe (for wide

field microendoscopy systems), or of varying depths below the epithelium (depth-sectioning with point-scanning systems). Benefits of end-on fiber bundle systems include eliminating the need for rinsing tissue after stain application to remove excess dye, which is required for alternative imaging modalities such as chromoendoscopy [16]. Eliminating the rinsing step is possible since end-on contact reduces specular reflection or unwanted fluorescence, with the additional benefit of rapid imaging after staining since there is no wait time for sufficient incubation to occur before rinsing. While a wide field approach does not have the depth-sectioning capabilities of a point-scanning system, it does not require a pinhole, laser light source and alignment, nor raster-scanning illumination.

Imaging typically depends on contrast between image regions, be it differences in color or in light intensity that highlight features of interest, and contrast can come from various sources, both endogenous and exogenous. Endogenous sources in endoscopic systems include hemoglobin absorption and inherently fluorescent molecules such as NADH and FAD, two prominent markers of metabolism. Exogenous sources of contrast are more commonly added prior to image acquisition, such as chromoendoscopy or fluorescent microendoscopy. Chromoendoscopy depends on the colorimetric contrast provided by stains such as Lugol's iodine or methylene blue [16]. These dyes are typically absorbed by the tissue in varying degrees depending on properties such as increased or decreased cell cytoplasm or goblet cell presence [16]. After these dyes are applied, they then require multiple rinses before imaging under white light endoscopy [17]. A benefit of exogenous fluorescent dye based microendoscopy is the increased signal to noise ratio, as the fluorescently stained regions are emphasized. Examples include fluorescence microendoscopy using acridine dyes [7] and surface magnifying endoscopy using the fluorescent emission of methylene blue [18]. Fluorescently stained regions will vary

depending on the dye, for example acridine-derived dyes such as proflavine will preferentially stain nucleic structures, whereas methylene blue will be preferentially absorbed by mucosal tissue [5, 16]. Proflavine has been used as a topically delivered, exogenous contrast agent with fluorescent microendoscopy systems due to its DNA intercalating nature. Therefore, proflavine predominantly highlights cellular nuclei in cytology specimens [19], as well as squamous bulk tissue such as oral and esophageal [5, 8]. Proflavine is an amphipathic dye comprised of a three carbon ring structure, and capable of intercalation within the minor groove of the DNA helix [20]. Broad acceptance of proflavine and its use in vivo in human subjects has been limited in the United States as DNA-intercalating dyes are considered potentially hazardous and mutagenic [21, 22]. Fluorescein, on the other hand, has a history of clinical use as an intravenous contrast agent in retinal angiography, as it does not intercalate DNA and tends to diffuse between cells rather than permeating them [23]. In addition, confocal microendoscopy modalities, such as Mauna Kea, have successfully used intravenous (IV) delivery of fluorescein for gastrointestinal imaging [24]. A limitation of fluorescein is its use as a contrast agent in squamous bulk tissue, such as oral epithelium, where nuclei shape and homogeneity is a main indicator of dysplasia [8]. On the other hand, fluorescein has been shown to have a sensitivity of 88% for detection of high-grade intraepithelial neoplasia in Barrett's esophagus, when using IV delivery in conjunction with confocal microendoscopy [25]. When imaging with wide field modalities, such as the microendoscopy system studied in this manuscript, we have shown that topical application of fluorescein is sufficient to highlight crypt structures, while topical delivery via an auxiliary endoscopy probe channel might minimize the amounts of systemic contrast agent [26].

Adequate contrast agents not only provide the clinician with in vivo qualitative insight, but can be used to acquire and analyze digital images. Pathology studies of biopsies or sections

typically depend on H&E slides qualitatively analyzed for pre-neoplastic markers such as nuclei size, shape, distribution, as well as crypt structure [27]. Qualitative analysis of images acquired with fluorescence microendoscopy by trained observers has been shown to be highly sensitive and specific [15]. Intraobserver agreement was high, and provided positive results for subjective review of microendoscopic images [15]. While there is a benefit to subjective and complementary image analysis, introducing a new imaging modality into an intraoperative setting necessitates a certain burden of training, namely additional training for the clinician. Image acquisition can be combined with computer-based analysis and diagnostic algorithms to provide complementary data to guide clinicians in their analysis of the tissue at the site of interest [7, 28, 29]. Automated image analysis provides an objective, replicable output to lessen the burden of training for clinicians. Our previous work has shown that the automated detection sensitivity of crypt structures in images of proflavine-stained colorectal epithelium using a custom algorithm ranges from 71 to 94% [30]. In addition, preliminary quantification of crypt area and circularity suggest that crypt quantification may provide an unbiased metric for aiding clinicians using fluorescence microendoscopy systems [27, 31].

In this study, we have evaluated the ability of topical proflavine and fluorescein to provide contrast in colorectal epithelium using end-on fiber bundle microendoscopy imaging of bulk ex vivo tissue. For qualitative comparison of topical staining, porcine and caprine bulk colorectal tissue was stained with proflavine and fluorescein solutions and imaged. For quantitative comparison, we have calculated the automated average crypt detection sensitivity of our custom algorithm using porcine bulk tissue stained topically with proflavine and fluorescein. In addition, ex vivo human colorectal tissue was imaged to quantitatively compare crypt area and circularity in grossly normal and grossly dysplastic regions. These quantified results provided us

with values in order to compare the viability of both these topical contrast agents for use in conjunction with fluorescence microendoscopy systems. Our results present topical application of fluorescein as a reasonable alternative to proflavine for fluorescence imaging of the colorectal tract.

2. Materials and Methods

2.1 Fiber bundle microendoscopy system and topical contrast agents

The microendoscopy system has been previously described [7, 30], and consists of a 455nm LED (Philips, USA), a filter set (Chroma Tech, USA), monochrome camera (Flea 3, USB 3.0, Point Grey Research Inc., CA), a 10x objective (NA 0.25, Olympus, Japan), and a fiber bundle image guide comprised of 50,000 fibers with 3.5µm center to center spacing (FIGH-50-1100N fiber, Myriad Fiber Imaging Tech, Inc., USA) with customized ends. The distal end has a modified SMA connector with rounded edges, to reduce the risk of tissue tearing as well as protect the fiber from chipping. Proflavine hemisulfate was prepared at a concentration of 0.01% (w/v) in 1x phosphate buffered saline (PBS) [30]. Fluorescein salt solution was prepared at 0.05% (w/v) in 1x PBS. We used fluorescein sodium salt, with a reported solubility of 0.1% (w/v) in water (F6377, Sigma-Aldrich), therefore our study investigated at and below this concentration.

2.2 Image intensity as a measure of topical contrast agent concentration

Previous studies of clinical microendoscopy using topical proflavine have used a standard concentration of 0.01% (w/v); we compared three concentrations of proflavine against fluorescein salt solutions with equal weight-per-volumes. We sectioned 6 adjacent regions of porcine colorectal tissue, and stained each section with one of the following contrast agents and concentrations: 0.01% (w/v) proflavine, 0.05% (w/v) proflavine, 0.1% (w/v) proflavine, 0.01%

(w/v) fluorescein, 0.05% (w/v) fluorescein, 0.1% (w/v) fluorescein, all solutions made with 1x PBS. Ten images were acquired of each section, with identical camera settings; 50ms exposure and 5dB gain. We qualitatively inspected them, as well as quantitatively compared them by measuring the average image intensity. The average image intensity (N = 10 images) of each solution was plotted; error bars denote standard error [Fig. 5]. Statistical values were obtained from post-hoc testing of a one-way ANOVA using Tukey's honestly significant difference (HSD), with p-value <0.05 as the criterion for significant difference.

2.3 Animal tissue procurement

Microendoscopic images of freshly resected caprine colorectal tissue were acquired in collaboration with the University of Arkansas Animal Science Abattoir, which provided tissue from recently slaughtered animals at their facility. 12-inch distal colon specimens were resected within an hour of slaughter, and imaged within an hour of resection. Siloam Spring Processing provided porcine colorectal tissue from recently slaughtered animals at their facility. 12 to 24-inch distal colon specimens were resected within an hour of slaughter, and refrigerated for approximately an hour before imaging, and imaged within an hour of removal from refrigeration. Specimens were obtained from two goats and two pigs for the quantitative study in this manuscript. Colon sections were rinsed with water, longitudinally cut to expose the lumen, and the lumen was rinsed with cold PBS. For each specimen, a single region of approximately 2 inches by 8 inches was sectioned for imaging.

2.4 Human tissue procurement

Microendoscopic images of freshly resected human colorectal tissue were acquired in collaboration with the University of Arkansas for Medical Sciences, from consenting patients under IRB protocol (#204651). Consenting patients, over the age of 18, with benign or

carcinogenic disease, were accepted under this protocol. Colorectal tissue was resected and sent to the pathology lab, where residents rinsed, longitudinally sectioned, and pinned the colorectal tissue to a paraffin block. Three specimens (two cases of benign disease and one invasive adenocarcinoma) were used for the data in this manuscript, with "normal" images acquired from grossly appearing normal mucosa from each of the three specimens, as well as images of neoplastic mucosa regions in the one specimen with invasive adenocarcinoma.

2.5 Microendoscopy image acquisition

The animal colorectal tissue was first longitudinally sectioned and then placed epithelium side up on a 150mm Petri dish. Colon sections of each specimen, porcine and caprine, were divided using a scalpel, with one section stained with proflavine and the adjacent section stained with fluorescein. No specimen received both contrast agents on the same tissue area. Separate sections of the specimen were used for multiphoton microscopy, though this separate section was also divided into adjacent sections for individual staining. Microendoscopy images were acquired immediately following topical application of proflavine (0.01% w/v in 1x PBS) or fluorescein salt solution (0.05% (w/v) in 1x PBS) with a cotton swab to epithelial surface, with occasional re-application of dye as needed. While endoscopic application of the dye would likely be achieved through a spray nozzle port, gently rolling the cotton swab has been previously used for ex vivo application without adverse effect for microendoscopic imaging [7, 8, 15]. Individual images were acquired by manually placing the distal end of the fiber bundle in contact with the epithelial surface of the tissue. Images of tissue stained with proflavine were acquired with 100ms exposure and 5dB gain and images of fluorescein were acquired with 50ms exposure and 5dB gain.

Human colorectal tissue was pinned to a paraffin block, lumen side up, and for each specimen, two regions of normal colon were chosen, as well as two regions of dysplastic colon. Microendoscopy images were acquired immediately following topical application of fluorescein salt solution (0.05% (w/v) in 1x PBS) with a cotton swab, with occasional reapplication of the dye as needed. Individual images were acquired by manually placing the distal end of the fiber bundle in contact with the epithelial surface. Image acquisition lasted approximately 30-40 minutes, with 50ms exposure and 5dB gain settings.

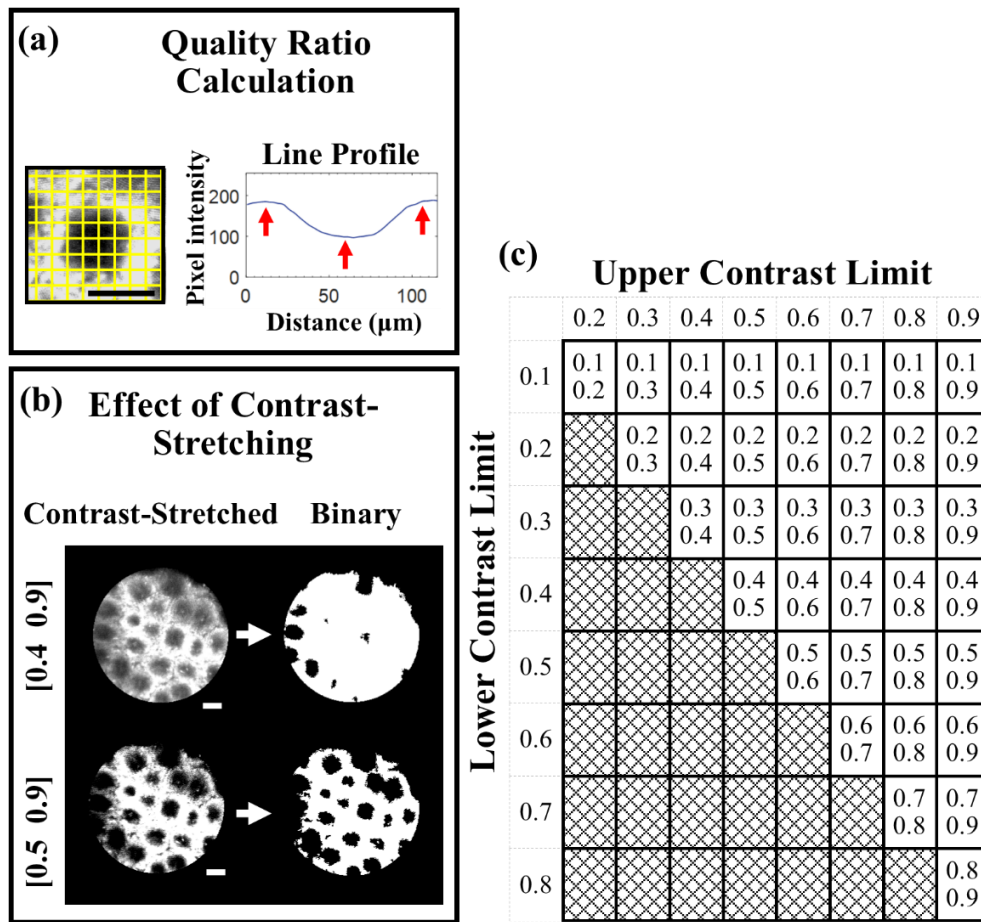## 2.6 Multiphoton image acquisition for qualitative comparison

Two 1cm^2 sections of caprine colorectal tissue were placed on individual glass slides, topically stained with either proflavine (0.01% (w/v)) or fluorescein (0.05% (w/v)) solution, and covered with No.1 coverslips, and immediately imaged using a MaiTai (SpectraPhysics) Ti:Sapphire pulsed laser, coupled to a customized multiphoton microscope system with an emission bandpass filter of 525nm center wavelength and 45nm bandwidth (Thorlabs). Images from tissues stained with these two agents were acquired using 900nm two-photon excitation at 5mW power at the sample, and a 40x (0.8 NA) water immersion objective (Nikon). Images comprised a 261µm by 261µm field-of-view, at 512 by 512 pixels.

2.7 Crypt detection and quantification algorithm and optimization of parameters

We have previously developed a custom image feature quantification algorithm (QFEA) for automated crypt detection and quantification of crypt morphology in microendoscopic images of proflavine-stained colorectal tissue [30]. This algorithm was designed to detect, segment, and quantify area and circularity of crypt shapes in microendoscopic images, and calculated automated crypt detection sensitivity at the crypt level by comparing if the algorithm detected a crypt at the position that the trained observer visually detected a crypt [30]. We have

optimized this algorithm for images of fluorescein-stained colorectal tissue, and compared the crypt detection sensitivity of the algorithm for proflavine versus fluorescein-stained epithelium, as described below. Prior to image quantification motion-blurred images were excluded from quantification, then the signal-to-background ratio was calculated, which we have termed the Quality Ratio (QR). We designed the QR metric to be a crypt-specific signal-to-background ratio [30], as the pixel-by-pixel signal-to-background ratio can vary and be misleading when calculated. The QR metric smooths individual pixel peaks and troughs, in order to calculate the more general signal-to-background ratio of the crypts [7]. Pixel intensity line profiles were extracted from the image in a grid like pattern, and the peak-to-trough ratios of the profiles were averaged to calculate the image's QR [Fig. 1(a)] [30]. Figure 1(a) shows an example of the line profiles crossing through a crypt, with a representative example of a line profile through the crypt shown to the right; these line profiles in actuality cover the entirety of the image. Images were then contrast-enhanced for increased efficacy in image segmentation. The pixel intensities are normalized to a range of 0 to 1, and contrast limit pairs have an upper and lower contrast limit, for example [0.2 0.9]. These contrast limit pairs refer to how 1% of image pixels fall below the lower contrast limit (0.2) and are mapped to a normalized signal value of 0, and 1% fall above the upper contrast limit (0.9) and are mapped to a normalized signal value of 1. Contrast-enhanced images were then binarized with a variable threshold automatically determined by Otsu's method [32], designed to minimize variance of values in the binary image. Figure 1(b) shows the effect of different contrast limit pairs on binary images created for subsequent image segmentation. The optimal contrast limit pairs will vary depending on the initial image intensity and contrast, therefore need to be carefully selected for each topical contrast agent. In order to determine the optimal contrast limit pairs for microendoscopy images of fluorescein-stained

epithelium, 100 images of porcine tissue were subject to a range of contrast limit pairs, to determine which pairs produced the highest automated crypt detection sensitivity values [30]. Automated crypt detection sensitivity was determined by comparing the sensitivity (true positives divided by the sum of true positives and false negatives) of the algorithm to manual crypt identification by a trained observer. Figure 1(c) shows the contrast limit pairs used to optimize the crypt detection sensitivity; contrast limits were increased by 10% and ranged from [0.1 0.2] to [0.8 0.9].

(a) Quality Ratio Calculation

(b) Effect of Contrast-Stretching

(c) Upper Contrast Limit / Lower Contrast Limit

| Lower \ Upper	0.2	0.3	0.4	0.5	0.6	0.7	0.8	0.9
0.1	0.1 / 0.2	0.1 / 0.3	0.1 / 0.4	0.1 / 0.5	0.1 / 0.6	0.1 / 0.7	0.1 / 0.8	0.1 / 0.9
0.2		0.2 / 0.3	0.2 / 0.4	0.2 / 0.5	0.2 / 0.6	0.2 / 0.7	0.2 / 0.8	0.2 / 0.9
0.3			0.3 / 0.4	0.3 / 0.5	0.3 / 0.6	0.3 / 0.7	0.3 / 0.8	0.3 / 0.9
0.4				0.4 / 0.5	0.4 / 0.6	0.4 / 0.7	0.4 / 0.8	0.4 / 0.9
0.5					0.5 / 0.6	0.5 / 0.7	0.5 / 0.8	0.5 / 0.9
0.6						0.6 / 0.7	0.6 / 0.8	0.6 / 0.9
0.7							0.7 / 0.8	0.7 / 0.9
0.8								0.8 / 0.9

Figure 1. (a) Example of grid pattern on close-up of individual crypt (line profiles extracted every 40 pixels), a single pixel intensity line profile plotted as an example, and peaks and trough (red arrows) labelled. (b) Example of effect of changing the contrast limit pairs on conversion into a binary image. (c) Table of contrast limit combinations tested for automated crypt detection sensitivity. Contrast enhancement scales image intensity values (0 to 255) between 0 and 1. Both upper and lower contrast limits were iteratively increased by 10% to cover a range from [0.1 0.2] to [0.8 0.9]. Gray region depicts impractical contrast limit pairs. Scale bars are 100μm.

3. Results

### 3.1 Qualitative image comparison of topical contrast agents

Both topical contrast agents provide similar qualitative crypt structure information in microendoscopic images of superficial colon epithelium. Figure 2 shows a comparison of Figs. 2(a) and 2(b) fluorescein-stained, and Figs. 2(c) and 2(d) proflavine-stained, as well as Figs. 2(a) and 2(c) porcine, and Figs. 2(b) and 2(d) caprine epithelial tissue. Pathology, the gold standard, would use H&E staining to investigate the crypt shape, homogeneity, and nuclei shape and distribution [27]. The selected fiber bundle was designed in favor of a larger field-of-view, which inherently limits the resolution of individual nuclei. Using our system, neither proflavine nor fluorescein staining permit a careful study of nuclei shape and distribution, but they do highlight the shape and homogeneity of crypts. Both contrast agents delineate the inner crypts as dark, mostly homogenous, circular regions, while also providing contrast to the interstitial regions. While proflavine preferentially stains cell nuclei, leading to ring-like image features around the dark crypts (arrows in Figs. 2(c) and 2(d)), fluorescein stains the interstitial spaces more uniformly, while still providing contrast with the crypts (black arrows in Figs. 2(a) and 2(b)). In our experiments, fluorescein had an increased likelihood to pool at the center of the shallower caprine crypts [Fig. 2(e)], and appears as bright dot-like structures in the center of the crypts (yellow arrow in b).
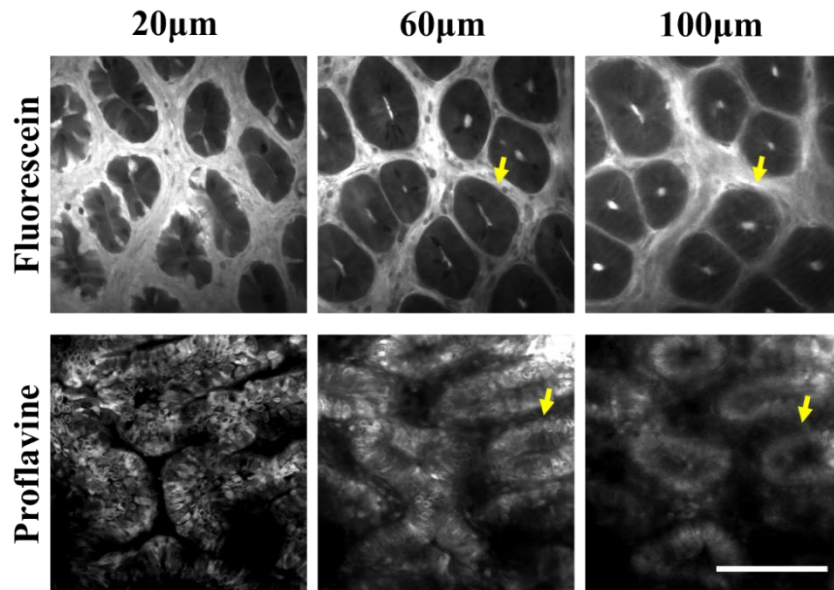
110
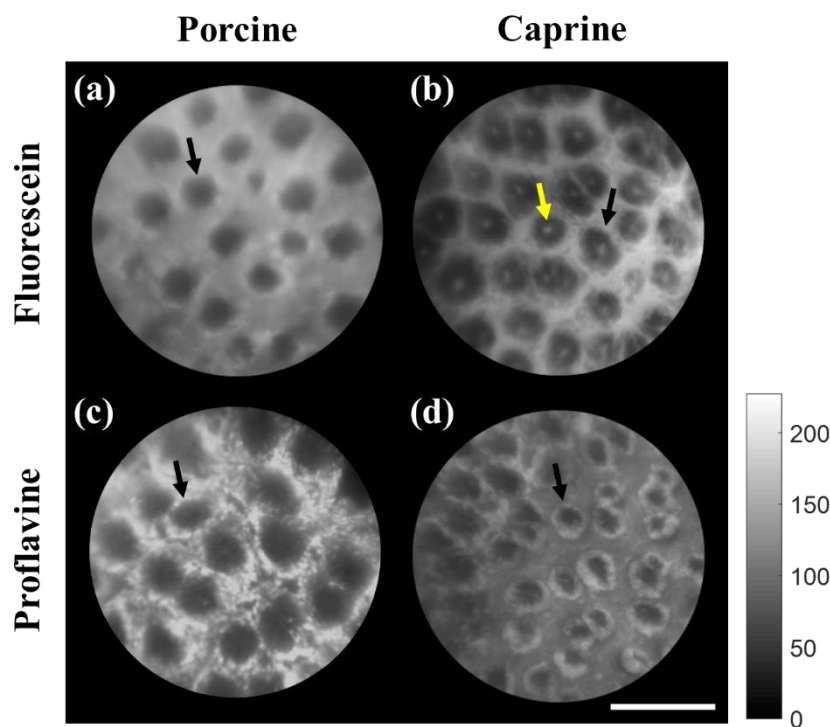
Figure 2. Qualitative comparison between microendoscopic images of bulk colorectal porcine and caprine tissue stained with proflavine and fluorescein. (a) and (b) Tissue stained with fluorescein (0.04% (w/v) in PBS), imaged at 50ms exposure and 5dB gain. (c) and (d) Tissue stained with proflavine (0.01% (w/v in PBS)), imaged at 100ms exposure and 5dB gain. (a) and (c) Porcine tissue; (b) and (d) caprine tissue. All images have been equally contrast enhanced for publishing; colorbar shows intensity values from 0 to 255. Scale bar is 250µm.

When imaged under a 40x 0.8NA objective for a 261µm by 261µm field of view, using multiphoton microscopy, the subtle differences in staining are readily apparent. Fluorescein stained bulk tissue [Fig. 3(a)] shows even staining of general intracellular material, as well as greater pooling in the center of the crypts. As expected, since proflavine intercalates DNA [20], proflavine-stained bulk tissue [Fig. 3(b)] preferentially stains individual nuclei. An example is shown in the inset of Fig. 3(b), of an individual nucleus, where the red arrows point to the nuclear membrane. Figure 4 shows the staining of both contrast agents at up to 100µm below the epithelial surface, which is more than sufficient for an end-on fiber bundle system that gathers data from the epithelial surface. This panel of depth sections additionally serves to exemplify

how topical application of these contrast agents might also be applicable for depth-sectioning

imaging modalities such as confocal microendoscopy.
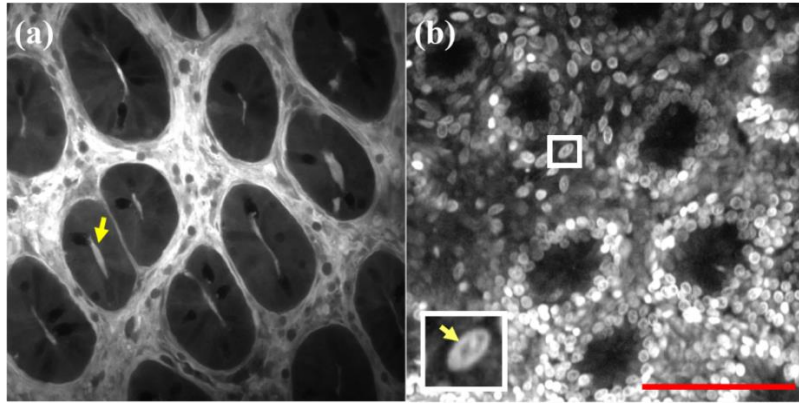
Figure 3. Qualitative comparison between multiphoton images of bulk colorectal caprine tissue stained with (a) fluorescein and (b) proflavine. (a) Tissue stained with fluorescein (0.04% (w/v) in distilled water). Yellow arrow points to fluorescein pooling in the center of the crypt. (b) Tissue stained with proflavine (0.01% (w/v in PBS)); white box inset shows a single stained cell, with yellow arrow pointing to the nuclear membrane. Both images were taken at 100 cumulative frames, 15fps, 20mW at sample, and have been equally enhanced for publication. Red scale bar is 100µm.

Figure 4. Qualitative comparison of multiphoton images of bulk colorectal animal tissue stained with fluorescein and proflavine at 20µm, 60µm, and 100µm below the epithelial surface. Caprine tissue stained with fluorescein (0.04% (w/v) in distilled water). Porcine tissue stained with proflavine (0.05% (w/v) in 1x PBS). All images were taken at 100 cumulative frames, 15fps, 20mW at sample, and have been enhanced for publication. Scale bar is 100µm.

3.2 Image intensity as a measure of topical contrast agent

Qualitative comparison of matching weight-per-volume of proflavine and fluorescein showed that while increasing proflavine concentration increased signal intensity, the signal of the interstitial tissue was not as large in comparison to fluorescein. Quantitative results [Fig. 5] supported this: average image intensity of fluorescein was significantly brighter than proflavine at each individual concentration. There was little qualitative difference between fluorescein at 0.01% (w/v) and proflavine at 0.1% (w/v), which is supported by a quantitative lack of significant difference between the average image intensity of these solutions.
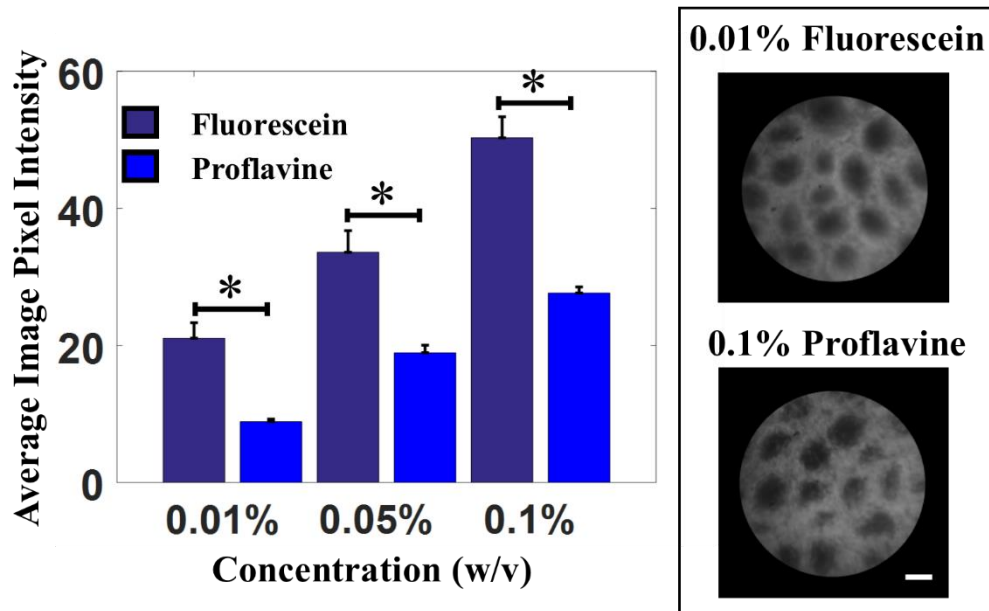
Figure 5. Comparison of different concentrations of topical contrast agents. Three different concentrations of each contrast agent, fluorescein and proflavine, were prepared at 0.01% (w/v), 0.05% (w/v), and 0.1% (w/v) in 1x PBS. Average image intensities (N = 10 images) of porcine colorectal tissue were plotted; error bars denote standard error. Fluorescein was significantly brighter than proflavine at each individual concentration, but fluorescein at 0.01% (w/v) was not significantly different from proflavine at 0.1% (w/v); statistical values were obtained from post-hoc testing of a one-way ANOVA using Tukey's honestly significant difference (HSD), with p-value.

3.3 Optimization of contrast limit pairs for increased crypt detection sensitivity

As previously stated, a range of contrast limit pairs [Fig. 1(c)] were applied to 100 images of fluorescein-stained porcine tissue. The average sensitivity (defined as the number of true positives divided by the sum of true positives and false negatives, as compared to manually selected crypts) of each contrast limit is shown in Fig. 6 as heatmaps for 6(a) proflavine and 6(c) fluorescein stained tissue. The internally numbered boxes were labelled for ease of correlation of contrast pairs chosen to the Figs. 6(b) and 6(d) plots of average sensitivity at various combinations of these chosen and labeled pairs; for example, in Fig. 6(a), value 1 stands for contrast limit pair [0.5 0.9]. As described in our previous work [30], a combination of several contrast limit pairs dramatically improves the average sensitivity of our crypt detection algorithm. Based on the results of Fig. 6(b) we chose a combination of 5 contrast limit pairs for optimal crypt detection sensitivity of images of proflavine-stained tissue, as the sensitivity surpasses 80%. Based on the results of Fig. 6(d), we chose a combination of 3 contrast limit pairs for optimal crypt detection sensitivity of images of fluorescein-stained tissue, as the sensitivity surpasses 90% while reducing risk of overtraining.
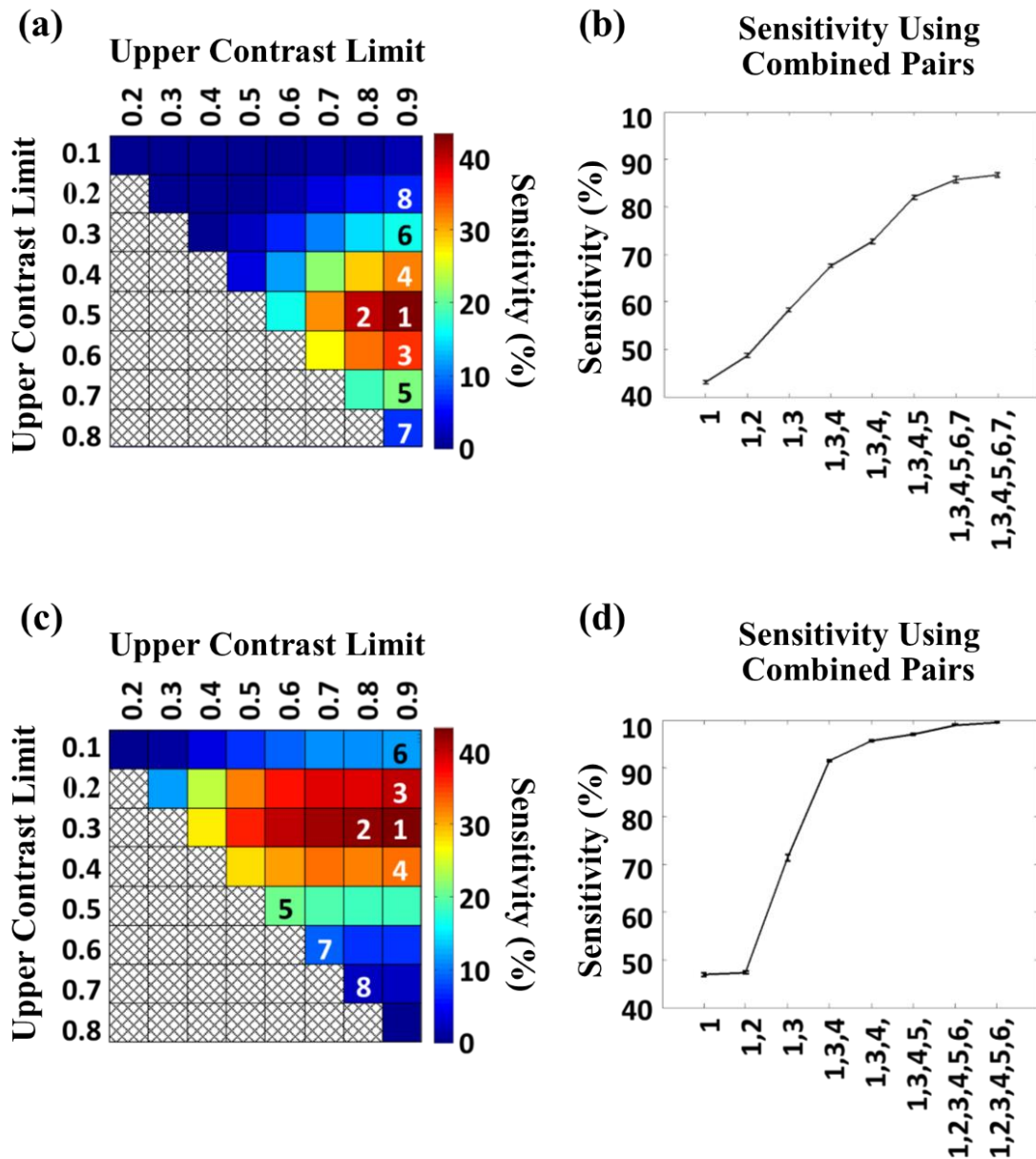
Figure 6. Optimization of crypt detection sensitivity by combination of contrast limit pairs for porcine tissue stained with (a) and (b) proflavine (0.01% (w/v)) and (c) and (d) fluorescein (0.04% (w/v) in PBS). (a) and (c) Heatmaps of the average percent sensitivity for each contrast limit pair; colorbars are average percent sensitivity. As with Fig. 2, the x-axes display the upper contrast limits, and the y-axes display the lower contrast limits. (b) and (d) Average test sensitivity, after 10 iterations of fivefold cross-validation, for each contrast limit pair or combination of contrast limit pairs. Maximum standard deviation of averages among all points was <0.61%. Heatmaps (a) and (c) are internally numbered with the selection of the highest sensitivity values per row, for clear correlation of numbered contrast limit pairs to the x-axis combinations in plots (b) and (d).

3.4 Quantitative image comparison of topical contrast agents

Our crypt quantification algorithm (QFEA) provided similar results for average crypt detection sensitivity in images of proflavine and fluorescein stained porcine tissue. As shown in Fig. 7, the QFEA was able to identify the majority of crypts for both topical contrast agents. One hundred images of proflavine-stained porcine epithelium and 100 images of fluorescein-stained porcine epithelium were quantified (QFEA) using contrast limit pairs selected using Fig. 6. As described in Section 2.7, a global QR value (peak-to-trough ratio) was calculated for each image as a metric of signal to background contrast, and the average QR of all images in a data set were tabulated against the average crypt detection sensitivity of QFEA. In Fig. 8(a), the sensitivities and positive predictive values (PPV) of images with a QR value equal to, or higher than, the specified QR cutoff value (x-axis) were averaged for an aggregate average sensitivity at that QR cutoff. The sensitivity was previously defined as true positives divided by the sum of true positives and false negatives. PPV was defined as true positives divided by the sum of true positives and false positives. The peak aggregate sensitivity for proflavine occurred at a QR cutoff value of 1.08 [Fig. 8(a)]. QR cutoff values higher than 1.1 averaged less than five images for average sensitivity and PPV calculation of proflavine-stained images, and are therefore not reliable indicators due to undersampling. Average sensitivity of fluorescein-stained images continued to increase slightly for QR values higher than 1.1, while PPV had a slight decline after that point (not shown). It is of interest to note that images of proflavine were overall less sensitive to automated crypt detection, but had a markedly greater PPV. Fluorescein had a PPV that barely surpassed 70%, while proflavine had a PPV close to 90%. In contrast, fluorescein demonstrated average sensitivities consistently above 90%, while proflavine sensitivity peaked at almost 85% at a QR cutoff value of 1.06.
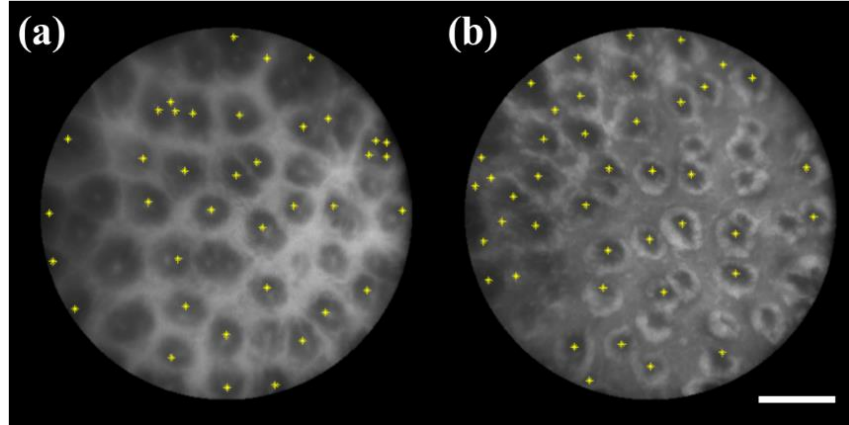
Figure 7. Comparison of automated crypt detection between microendoscopy images of bulk colorectal caprine tissue stained with (a) fluorescein and (b) proflavine. Yellow asterisks mark the centroids determined with the QFEA. (a) Tissue stained with fluorescein (0.04% (w/v) in distilled water). (b) Tissue stained with proflavine (0.01% (w/v in PBS)). Both images have been equally enhanced for publishing. Scale bar is 200µm.
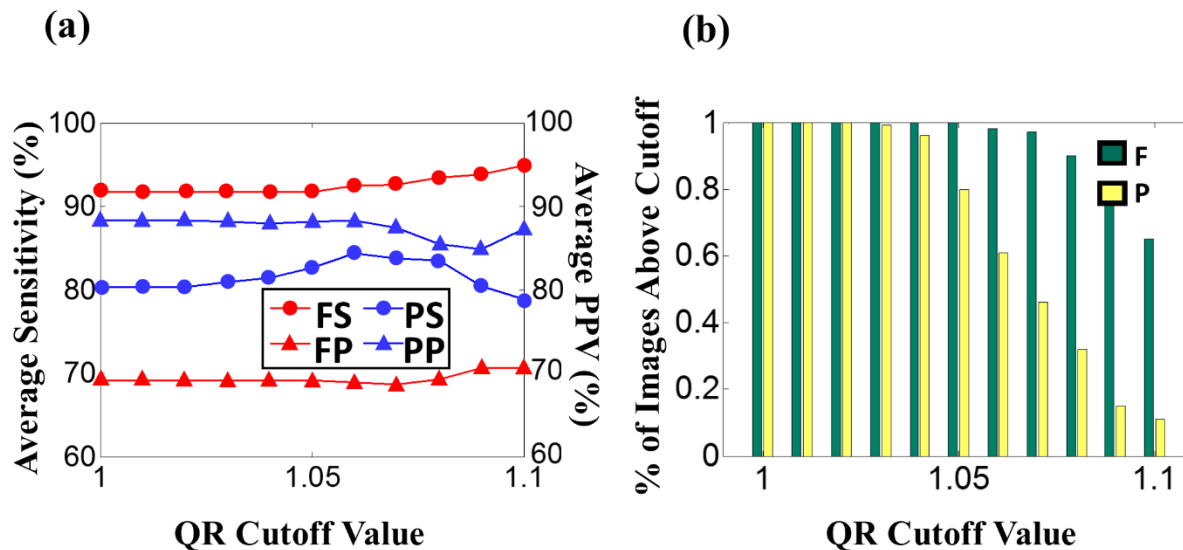
Figure 8. (a) Average sensitivity and positive predictive values (PPV) of the QFEA crypt detection versus the QR cutoff value; aggregate performance plotted against QR was calculated using images with QR values equal to or higher to the QR cutoff value labeled in the x-axis. PS: Proflavine Sensitivity; PP: Proflavine PPV; FS: Fluorescein Sensitivity; FP: Fluorescein PPV. (b) Percentage of images with QR values equal to or higher than the labeled QR cutoff value; one hundred images per group. F: Fluorescein; P: Proflavine.

3.5 Quantification of crypt area and circularity in preliminary clinical trial

Automated quantification of crypt area and circularity, using our quantification algorithm (QFEA), was tabulated for regions with grossly normal, and adenocarcinoma diagnoses. 66 images, corresponding to approximately 25mm^2 of epithelial surface, were acquired from grossly normal regions (no dysplasia, no benign disease), and 76 images (~29mm^2) from adenocarcinoma regions. Figure 9 shows that there was significant difference between normal (N.) and adenocarcinoma (A.) regions, with a p-value of 0.035 for area, but circularity was not significantly different with a p-value of 0.13, using a Student t-test.
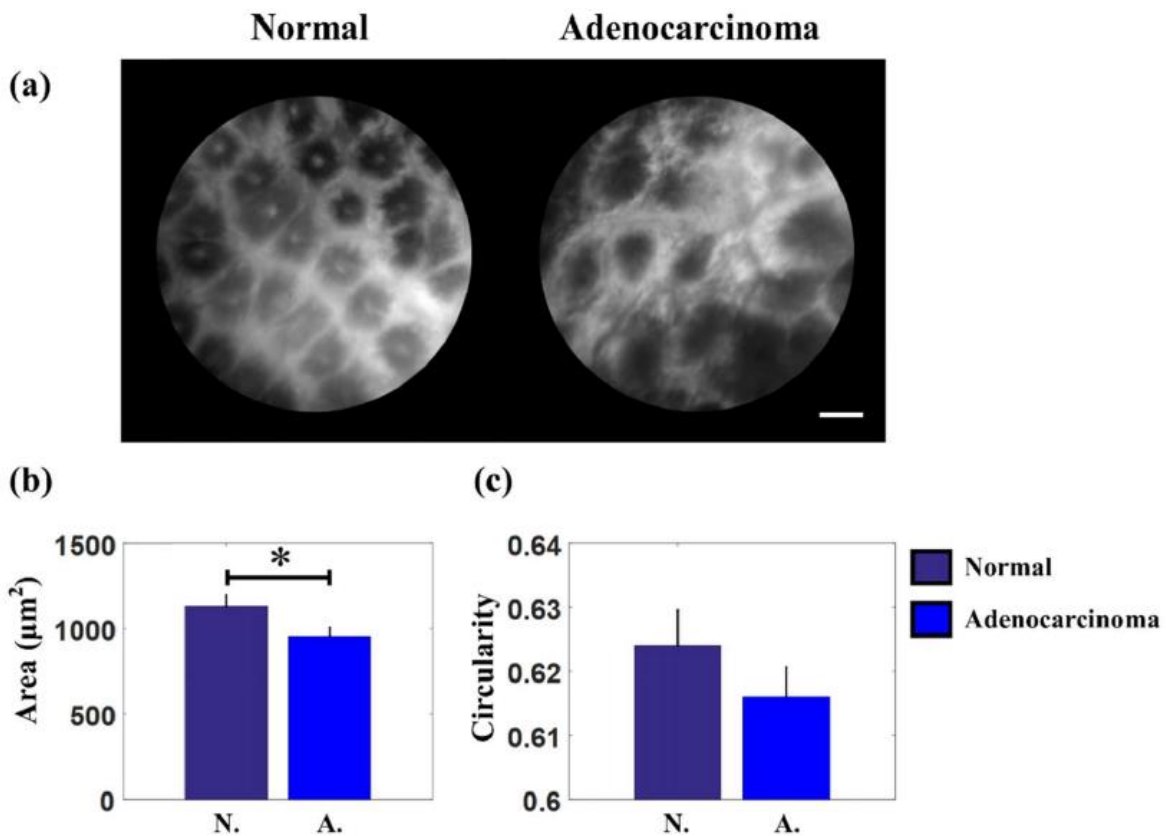
Figure 9. Quantitative comparison of crypt area and circularity. (a) Example of microendoscopic images of normal and adenocarcinoma regions. Scale bar is 100μm. (b) Average crypt area for normal and adenocarcinoma regions (N = 416 crypts, N = 603 crypts, respectively). P-value = 0.035. (c) Average crypt circularity for normal and adenocarcinoma regions (N = 416 crypts, N = 603 crypts, respectively). P-value = 0.13.

4. Discussion

Imaging of gastrointestinal epithelium via end-on fiber microendoscopy has been explored using DNA intercalating dyes, which so far have been used as investigational drugs in the United States [5, 15, 30]. A fluorescence alternative would be dyes already in clinical use, such as sodium fluorescein solution [33]. Our qualitative comparison of microendoscopy images of bulk colorectal tissue stained with fluorescein versus proflavine demonstrated that while the subcellular staining patterns differ [Fig. 3], fluorescein is able to provide similar information of crypt morphology to the previously established proflavine [Fig. 2]. An additional benefit of fluorescein as a contrast agent, in comparison to proflavine, includes reduced exposure time for images. Images of fluorescein-stained tissue were initially acquired at 100ms, for identical integration time of proflavine-stained tissue, but the images were over-saturated and we lowered the integration time until the images were of equal qualitative quality to proflavine. This resulted in fluorescein-acquisition at 50ms and proflavine-acquisition at 100ms. Reducing the required integration time has the benefit of reducing the number of motion-blurred images. Reduced exposure time and reduced motion-blur is an important advantage for manual or in vivo acquisition, allowing for the flexibility of manually holding the probe yet not requiring the clinician to have steady hands. While clamping the probe during image acquisition would have eliminated motion from unstable handheld placement, we chose to retain the potential of motion-blurring in order to mimic in vivo imaging, where patient breathing or movement could contribute to motion-blur. Quantitatively, the results of automated crypt detection demonstrated a sharp increase in crypt detection sensitivity using less combinations of contrast-limit pairs; while proflavine images required a combination of five contrast limit pairs to achieve greater than 80% average sensitivity, fluorescein images required a combination of only three contrast limit pairs

to achieve an average sensitivity greater than 90% [Fig. 6]. A reduced number of contrast limit pairs is computationally time efficient, as well as reducing the risk of overtraining the algorithm. In addition to contrast limit pair combinations, the average sensitivity of the crypt detection algorithm is greater for the fluorescein data set. Even excluding images with low signal-to-background contrast (at a QR cutoff value of 1.06, Fig. 8(a)), the average crypt detection sensitivity of the proflavine data set never reached 90%, whereas the fluorescein data set average sensitivity was consistently greater than 90%. Despite this, the fluorescein data set has a consistently lower positive predictive value (PPV) [Fig. 8(a)]. Heatmaps of the PPV (data not shown) showed similar results to the sensitivity heatmaps, sharing the top two contrast limit pairs as resulting in the highest sensitivity and PPV values. This suggests that quantitative analysis of fluorescein images is more sensitive in the detection of crypts, while not as adept as a diagnostic tool due to a higher number of false positives, thought this requires additional investigation into alternative reasons for this imbalance. Quantitative crypt detection results suggesting a lower PPV are not necessarily a critical limitation for clinical translation of a microendoscopic system. Given the length and size of the colorectal tract, there is minor risk in extracting multiple biopsies and therefore the surgical recommendations is to biopsy two to four regions each 10cm, with additional sampling of suspicious regions [34]. A highly sensitive, if not specific, tool would be useful in improving biopsy targeting of abnormal regions. While microendoscopic systems have achieved high sensitivity and specificity rates [15], they have not yet proven capable of replacing the gold standard of pathological staging of biopsies, therefore microendoscopy remains most useful in complementing existing endoscopy procedures. Our preliminary clinical results show that the automated algorithm measures a significant difference between crypt areas of normal and dysplastic regions, and additional work could increase the

120

accuracy and breadth of quantifiable image features. One drawback of automated quantification, though, is that there is usually an increased regulatory burden when a system uses computer based diagnosis, which is not an attractive prospect for vendors.

Fluorescein is also more relevant as a clinical contrast agent, compared to DNA intercalating dyes, since it is already clinically used for intravenous injection and has demonstrated to pose limited risk to patient health. A drawback that should be considered is that intravenous fluorescein has a risk of anaphylaxis, with death from complications after intravenous injection during angiography procedures estimated at 1 in 220,000 patients [35]. Analysis of intrathecal administration of fluorescein in Europe and the United States showed that when a fluorescein dose of 1mL per 10kg of body weight of 5% (w/v) was used (total 50mg), side effects were minor and transient, with additional complications reported for higher doses (total 100-700mg) [35]. The side-effects of intravenous injection for confocal endomicroscopy have been similarly reported as minor for doses of up to 5mL of 10% (w/v) fluorescein, and while participants in their study experienced no severe reactions, the authors caution that anaphylaxis is rare but should be "anticipated and prepared for as for any drug [24]". It is unclear if a topical application of the stain could possibly have reactions of equal or lesser severity. Alternatively, topical application of fluorescein required only the lower recorded concentrations of fluorescein, and could potentially pose little risk to the patient in small topical doses. Despite some limitations, we have described in this manuscript how topical application of fluorescein holds promise as a potential contrast agent alternative to proflavine for glandular tissue, specifically colon, since the crypt structures visible using proflavine are also visible when imaging with fluorescein. Using a 1mm fiber bundle, images acquired with both proflavine and fluorescein contrast offer similar image features for quantification, such as crypt area and

circularity. There was over 90% crypt detection sensitivity of porcine tissue, as well as statistical

significance in our preliminary clinical study using topical application of fluorescein solution,

between grossly normal and grossly dysplastic regions of colorectal tissue.

References

[1] S. P. Prieto, K. K. Lai, J. A. Laryea, J. S. Mizell, W. C. Mustain and T. J. Muldoon, "Fluorescein as a topical fluorescent contrast agent for quantitative microendoscopic inspection of colorectal epithelium," *Biomedical Optics Express,* vol. 8, *(4),* pp. 2324-2338, 2017.

[2] S. Kitabatake, Y. Niwa, R. Miyahara, A. Ohashi, T. Matsuura, Y. Iguchi, Y. Shimoyama, T. Nagasaka, O. Maeda and T. Ando, "Confocal endomicroscopy for the diagnosis of gastric cancer in vivo," *Endoscopy,* vol. 38, *(11),* pp. 1110-1114, 2006.

[3] W. Piyawattanametha, H. Ra, K. E. Loewke, M. J. Mandella, C. H. Contag, Z. Qiu, T. D. Wang, S. Friedland, J. T. Liu and G. S. Kino, "In vivo near-infrared dual-axis confocal microendoscopy in the human lower gastrointestinal tract," *J. Biomed. Opt.,* vol. 17, *(2),* pp. 021102, 2012.

[4] W. Zhong, J. Celli, I. Rizvi, Z. Mai, B. Spring, S. Yun and T. Hasan, "In vivo high-resolution fluorescence microendoscopy for ovarian cancer detection and treatment monitoring," Br. J. Cancer, vol. 101, (12), pp. 2015, 2009.

[5] T. J. Muldoon, N. Thekkek, D. Roblyer, D. Maru, N. Harpaz, J. Potack, S. Anandasabapathy and R. Richards-Kortum, "Evaluation of quantitative image analysis criteria for the high-resolution microendoscopic detection of neoplasia in Barrett's esophagus," J. Biomed. Opt., vol. 15, (2), pp. 026027-026027-7, 2010.

[6] G. A. Sonn, S. E. Jones, T. V. Tarin, C. B. Du, K. E. Mach, K. C. Jensen and J. C. Liao, "Optical biopsy of human bladder neoplasia with in vivo confocal laser endomicroscopy," J. Urol., vol. 182, (4), pp. 1299-1305, 2009.

[7] S. P. Prieto, A. J. Powless, K. Lai, J. A. Laryea, J. S. Mizell and T. J. Muldoon, "Qualitative and quantitative comparison of colonic microendoscopy image features to histopathology," in SPIE BiOS, 2015, pp. 93280B-93280B-8.

[8] T. J. Muldoon, D. Roblyer, M. D. Williams, V. M. Stepanek, R. Richards–Kortum and A. M. Gillenwater, "Noninvasive imaging of oral neoplasia with a high-resolution fiber-optic microendoscope," Head Neck, vol. 34, (3), pp. 305-312, 2012.

[9] R. L. Siegel, K. D. Miller and A. Jemal, "Cancer statistics, 2015," CA: A Cancer Journal for Clinicians, vol. 65, (1), pp. 5-29, 2015.

[10] B. Hofstad, M. H. Vatn, S. N. Andersen, H. S. Huitfeldt, T. Rognum, S. Larsen and M. Osnes, "Growth of colorectal polyps: redetection and evaluation of unresected polyps for a period of three years," Gut, vol. 39, (3), pp. 449-456, Sep, 1996.

[11] J. K. Triantafillidis, G. Nasioulas and P. A. Kosmidis, "Colorectal cancer and inflammatory bowel disease: epidemiology, risk factors, mechanisms of carcinogenesis and prevention strategies," Anticancer Res., vol. 29, (7), pp. 2727-2737, Jul, 2009.

[12] S. H. Itzkowitz and D. H. Present, "Consensus conference: colorectal cancer screening and surveillance in inflammatory bowel disease," Inflamm. Bowel Dis., vol. 11, (3), pp. 314-321, 2005.

[13] P. Hsiung, J. Hardy, S. Friedland, R. Soetikno, C. B. Du, A. P. Wu, P. Sahbaie, J. M. Crawford, A. W. Lowe and C. H. Contag, "Detection of colonic dysplasia in vivo using a targeted heptapeptide and confocal microendoscopy," Nat. Med., vol. 14, (4), pp. 454-458, 2008.

[14] S. J. Miller, B. P. Joshi, Y. Feng, A. Gaustad, E. R. Fearon and T. D. Wang, "In vivo fluorescence-based endoscopic detection of colon dysplasia in the mouse using a novel peptide probe," PloS One, vol. 6, (3), pp. e17384, 2011.

[15] N. D. Parikh, D. Perl, M. H. Lee, B. Shah, Y. Young, S. S. Chang, R. Shukla, A. D. Polydorides, E. Moshier and J. Godbold, "In vivo diagnostic accuracy of high-resolution microendoscopy in differentiating neoplastic from non-neoplastic colorectal polyps: a prospective study," Am. J. Gastroenterol., vol. 109, (1), pp. 68-75, 2014.

[16] P. Trivedi and B. Braden, "Indications, stains and techniques in chromoendoscopy," QJM: An International Journal of Medicine, vol. 106, (2), pp. 117-131, 2012.

[17] W. Curvers, L. Baak, R. Kiesslich, A. Van Oijen, T. Rabenstein, K. Ragunath, J. F. Rey, P. Scholten, U. Seitz, F. Ten Kate, P. Fockens and J. Bergman, "Chromoendoscopy and narrow-band imaging compared with high-resolution magnification endoscopy in Barrett's esophagus," Gastroenterology, vol. 134, (3), pp. 670-679, Mar, 2008.

[18] R. A. Wall and J. K. Barton, "Fluorescence-based surface magnifying chromoendoscopy and optical coherence tomography endoscope," J. Biomed. Opt., vol. 17, (8), pp. 086003, 2012.

[19] S. P. Prieto, A. J. Powless, J. W. Boice, S. G. Sharma and T. J. Muldoon, "Proflavine Hemisulfate as a Fluorescent Contrast Agent for Point-of-Care Cytology," PloS One, vol. 10, (5), pp. e0125598, 2015.

[20] C. J. Alden and S. Arnott, "Stereochemical model for proflavine intercalation in A-DNA," Nucleic Acids Res., vol. 4, (11), pp. 3855-3862, 1977.

[21] D. M. DeMarini, K. H. Brock, C. L. Doerr and M. M. Moore, "Mutagenicity and clastogenicity of proflavin in L5178Y/TK /−− 3.7. 2. C cells," Mutation Research/Genetic Toxicology, vol. 204, (2), pp. 323-328, 1988.

[22] Y. Iwamoto, L. R. Ferguson, A. Pearson and B. C. Baguley, "Photo-enhancement of the mutagenicity of 9-anilinoacridine derivatives related to the antitumour agent amsacrine," Mutation Research/Fundamental and Molecular Mechanisms of Mutagenesis, vol. 268, (1), pp. 35-41, 1992.

[23] R. P. Feenstra and S. C. Tseng, "Comparison of fluorescein and rose bengal staining," Ophthalmology, vol. 99, (4), pp. 605-617, 1992.

[24] M. B. Wallace, A. Meining, M. Canto, P. Fockens, S. Miehlke, T. Roesch, C. Lightdale, H. Pohl, D. CARR-LOCKE and M. Löhr, "The safety of intravenous fluorescein for confocal laser endomicroscopy in the gastrointestinal tract," Aliment. Pharmacol. Ther., vol. 31, (5), pp. 548-552, 2010.

[25] H. Pohl, T. Rosch, M. Vieth, M. Koch, V. Becker, M. Anders, A. C. Khalifa and A. Meining, "Miniprobe confocal laser microscopy for the detection of invisible neoplasia in patients with Barrett's oesophagus," Gut, vol. 57, (12), pp. 1648-1653, Dec, 2008.

[26] R. Kiesslich and M. F. Neurath, "Endoscopic confocal imaging," Clinical Gastroenterology and Hepatology, vol. 3, (7), pp. S58-S60, 2005.

[27] H. M. Said, Physiology of the Gastrointestinal Tract, Two Volume Set. Academic Press, 2012.

[28] D. Shin, M. Protano, A. D. Polydorides, S. M. Dawsey, M. C. Pierce, M. K. Kim, R. A. Schwarz, T. Quang, N. Parikh and M. S. Bhutani, "Quantitative analysis of high-resolution microendoscopic images for diagnosis of esophageal squamous cell carcinoma," Clinical Gastroenterology and Hepatology, vol. 13, (2), pp. 272-279. e2, 2015.

[29] S. Srivastava, J. J. Rodríguez, A. R. Rouse, M. A. Brewer and A. F. Gmitro, "Computer-aided identification of ovarian cancer in confocal microendoscope images," J. Biomed. Opt., vol. 13, (2), pp. 024021-024021-13, 2008.

[30] S. P. Prieto, K. K. Lai, J. A. Laryea, J. S. Mizell and T. J. Muldoon, "Quantitative analysis of ex vivo colorectal epithelium using an automated feature extraction algorithm for microendoscopy image data," Journal of Medical Imaging, vol. 3, (2), pp. 024502, 2016.

[31] G. L. Tipoe and F. White, "Quantitative assessment of normal and potentially premalignant epithelium at different levels of human colorectal crypts," Histol. Histopathol., vol. 13, (2), pp. 395-404, 1998.

[32] N. Otsu, "A threshold selection method from gray-level histograms," Automatica, vol. 11, (285-296), pp. 23-27, 1975.

[33] R. Alford, H. M. Simpson, J. Duberman, G. C. Hill, M. Ogawa, C. Regino, H. Kobayashi and P. L. Choyke, "Toxicity of organic fluorophores used in molecular imaging: literature review," Molecular Imaging, vol. 8, (6), pp. 7290.2009. 00031, 2009.

[34] J. A. Eaden, J. F. Mayberry, British Society for Gastroenterology and Association of Coloproctology for Great Britain and Ireland, "Guidelines for screening and surveillance of asymptomatic colorectal cancer in patients with inflammatory bowel disease," Gut, vol. 51 Suppl 5, pp. V10-2, Oct, 2002.

[35] L. A. Yannuzzi, K. T. Rohrer, L. J. Tindel, R. S. Sobel, M. A. Costanza, W. Shields and E. Zang, "Fluorescein angiography complication survey," Ophthalmology, vol. 93, (5), pp. 611-617, 1986.

Chapter V: Differences in colonic crypt morphology of spontaneous and colitis-associated murine models via second harmonic generation imaging to quantify colon cancer development [1]

1. Background

Inflammatory bowel disease (IBD) is characterized by chronic inflammation of the gastrointestinal tract and is manifested clinically as either ulcerative colitis (UC) or Crohn's disease [2]. While there is currently no specific histological feature that is used to definitively distinguish between UC and Crohn's disease, an important distinction is the distribution pattern of the inflammation. UC is characterized by severe inflammation beginning at the rectum and continuing throughout the colon; Crohn's disease is characterized by lesions over Peyer's patches, and non-continuous regions of inflammation that span the entire depth of the intestinal wall [3-5].

Patients with UC exhibit an increased risk for colorectal cancer (CRC); approximately 29% of UC patients develop CRC within 10 years of diagnosis, while 2.9% with Crohn's disease develop CRC after 10 years of disease [6-9]. There are different types of lesions that may be detected in a UC patient during colonoscopy: two types associated with intraepithelial neoplasia are a dysplasia-associated lesion/mass (DALM) and an adenoma-like mass (ALM) [10, 11]. Flat or raised lesions without sharp contrast (delineation) against non-dysplastic epithelium are typically classified as DALMs, and are frequently associated with malignancy [11]. ALMs have features similar to sporadic adenomas that are observed in non-IBD patients [12]. Preliminary studies have suggested that standard polypectomy, a complete endoscopic resection of the ALM mass, followed by endoscopic surveillance is highly successful in patients with an ALM and could spare the patient a colectomy, since of the 34 patients in one study only one patient

developed an adenocarcinoma following the initial polypectomy [10-12]. Unfortunately, in 50-80% of DALM cases the lesions are not visible during standard endoscopy [11, 13]. Several modalities of endoscopic imaging have emerged to improve detection of flat or discolored lesions [14]. Among them, multiphoton microendoscopy uses nonlinear optical processes to yield label-free high-resolution image data and rapid 3-dimensional image acquisition up to several hundred microns in depth without the need for tissue resection and subsequent fixation [15]. These systems have recently overcome a number of specific technical challenges, including obtaining uniform scans, low sensitivity, durability and reliability of the scanner, and miniaturization of the distal scan mechanism [16, 17]. Miniaturization of multiphoton laser microscopy systems greatly enhances the clinical translatability of this modality, leading towards *in vivo* imaging applications in gastrointestinal epithelial tissues [18-20]. A form of multiphoton imaging, second harmonic generation (SHG) is a nonlinear optical process whereby non-centrosymmetric crystalline structures (such as collagen) interact with two low energy photons nearly simultaneously, resulting in the generation of a new photon at twice the energy (or half the wavelength of the incident photons). Multiphoton endoscopic systems capable of SHG imaging show great potential in improving clinical decision-making for patients with IBD. In the colon, collagen structures can be used to quantify changes in the three-dimensional crypt microstructure in the setting of IBD and associated dysplastic transformation. A systematic, quantitative model of these optical biomarkers of dysplasia progression could guide clinical translation of SHG imaging approaches for IBD patients.

Our study was designed to further develop this biomarker model via SHG imaging and quantification of morphological changes that occur in the crypt structures of murine models of spontaneous and colitis-associated colorectal tumors. A series of azoxymethane (AOM)

injections is used as a murine model for spontaneous (ALM-like) tumor progression as it induces

polypoid growth in the distal colon, similar to human CRC [21]. AOM injections followed by

subsequent administration of dextran sodium sulfate salt (DSS) is considered to have long-term

effects that produce cancerous flat lesions or dysplasia-associated lesion or mass (DALM-like)

similar to those observed in humans [22]. We also acquired SHG images of epithelial tissue over

discrete timepoints to investigate if temporal changes in crypt microstructure could be detected

and quantified at varying stages of tumor progression. Key SHG image features could serve as

optical biomarkers; a translatable measure towards detection of lesions and distinguishing ALM

and DALM type lesions endoscopically in patients with known IBD.

2. Methods

Murine models and colorectal tissue procurement

Two murine models were used for this study: a spontaneous colorectal carcinoma model

and a colitis-induced colorectal carcinoma model [21]. Thirty-one *A/J* mice (The Jackson

Laboratory, ME, USA) were used in accordance with the University of Arkansas Institutional

Animal Care and Use Committee-approved protocol #18093. Mice were received at 9 weeks of

age and allowed to acclimate for one week in a temperature and light controlled facility; mice

were maintained on an 12 hour day-night cycle, with a bedding mixture of approximately 75%

aspen chip bedding (7090A, Envigo, USA) and 25% paper product bedding (7099, Envigo,

USA). All procedures were conducted in the light phase. Food (Tekland 8640, Envigo, USA) and

water were provided ad libitum (Fig. 1). Mice were anesthetized using 1.5% isoflurane

(IsoThesia, Henry Schein Animal Health, OH, USA) and oxygen (Compressed USP Oxygen,

Airgas, PA, USA) from a precision vaporizer (911103, VetEquip, CA, USA), then placed on a

heating pad (TP700, Stryker Medical, MI, USA) with a nosecone for constant supply of 1.5% isoflurane.

The spontaneous colorectal carcinoma model (referred to as the AOM model), consisted of a series of six weekly subcutaneous injections of AOM (A5486, Sigma-Aldrich, Inc., MO, USA) diluted in sterile saline, at a dose of 10 mg per kg body weight [21]. Control mice underwent a series of six weekly subcutaneous injections of saline (injection site over the shoulders). AOM and Control cohorts acclimated and were injected in parallel. The colitis-induced colorectal carcinoma model (referred to as the AOM-DSS model) consisted of a single AOM injection (at 10 mg/kg body weight, subcutaneous administration), followed by several courses of drinking water supplemented with DSS (36,000-50,000 molecular weight, SKU 0216011080, MP Biomedicals, OH, USA) at a concentration of 1.5% (w/v) (Fig. 1) [21]. AOM-DSS cohorts acclimated and were injected a few months after the AOM and Control cohorts. Subcutaneous AOM injections were administered with 28 gauge syringe needles (BD329410, VWR, PA, USA) in volumes of less than 200 μL. For the AOM-DSS model, beginning on the day of the AOM injection, mice were provided free access to DSS solution for seven days [21]. On Day 8, the mice were provided untreated drinking water *ad libitum* for 14 days, and then the DSS-solution and untreated water cycle was repeated at Day 22 and Day 53 (Fig. 1) [21]. Post treatment, mice were provided food and water *ad libitum* and were weighed and inspected daily until two weeks after concluding AOM/DSS treatment, after which they were inspected daily and weighed weekly. Mice were euthanized at early (20-23 weeks) or late (24-28 weeks) time points, representative of early or late-stage carcinoma progression (Fig. 1). Mice within each cohort were randomly selected for euthanizing at either early or late timepoints. Figure 1

notes the number of mice per cohort: Control n = 9, AOM early n = 6, AOM late n = 3, AOM-DSS early n = 4, AOM-DSS late n = 9.

AOM

AOM-DSS
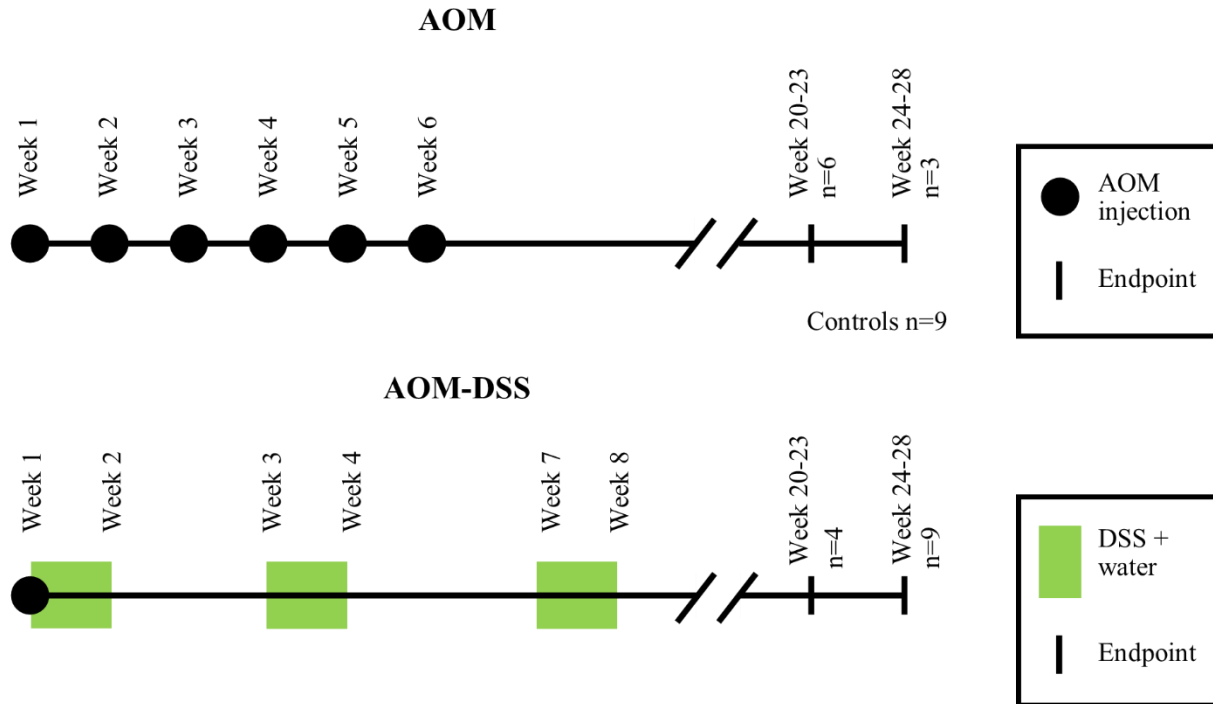
Figure 1. Timeline of murine models. Day 1 is the first azoxymethane injection, for mice at 10 weeks of age. Number of mice euthanized per time point and cohort labelled by n values.

AOM-injected mice develop lesions and small polyps at approximately 20 weeks, with tumors progressing in size over the subsequent weeks; mice began to show signs of rectal bleeding past 28 weeks and were therefore euthanized [21]. Mice were euthanized via anesthetized cervical dislocation. Murine colons were resected within 15 minutes of euthanasia, and a 1 cm section of distal colon was longitudinally sectioned and placed on a coverslip for imaging. An adjacent section of tissue was fixed in formalin and paraffin-embedded for reference H&E staining.

Multiphoton microscopy imaging system

The microscopy system comprises a titanium-sapphire ultrafast femtosecond pulsed laser source (Mai Tai eHP, Spectra-Physics, CA, USA), and galvo-resonant scan head scanners which acquires a fixed 15 frames per second (MPM-SCAN64J, Thorlabs, USA). The laser power was controlled via a quarter-wave plate and a polarizing beam splitter, to reduce the incoming excitation power at the sample to the range of tens to hundreds of milliwatts. The light was then circularly polarized, to reduce orientation bias of SHG in collagen, by use of a half-wave plate and a second polarizing beam splitter. Circular polarization was determined by measuring intensity of orthogonal collagen fibers at multiple regions, and selecting the optimal positioning of the half-wave plate for reduction of intensity variation at different orientations. Following the scanning optics, the illumination laser beam (at 800nm wavelength) passed through the back aperture of a 20x water immersion objective (0.85 NA, Nikon, NY, USA), prior to illuminating the sample, which was placed above the objective on an inverted microscopy stage. Backscattered SHG signal was collected via the objected and traveled through a 635nm long pass dichroic beamsplitter (Di02-R635, Semrock, NY, USA), a 447/60nm filter set (447/60nm 25mm dia. filter, Semrock, NY, USA), a 400nm/40nm filter set (400/40nm 25mm dia. filter, Semrock, NY, USA), and photomultiplier tube (H7422 PASO, Hamamatsu, Japan). The entire optical system resides inside an enclosure to reduce ambient light.

Second harmonic generation image acquisition

Freshly resected tissue was placed epithelium-down on a 24x40 mm No. 1 coverslip, then imaged using our non-linear optical microscopy imaging system described above. Total image acquisition time was approximately 1.5 seconds, with total optical power at the sample limited to prevent photo-damage. Individual images were acquired at 512 x 512 pixels at 14-bit depth,

yielding a 522 μm x 522 μm (~0.27 mm^2) field of view, at approximately 20 μm from the epithelial surface. Image stacks were acquired at consecutive depths from the epithelial surface, in 20 μm steps, from 20 μm to 100 μm below the epithelial surface (Fig. 2).
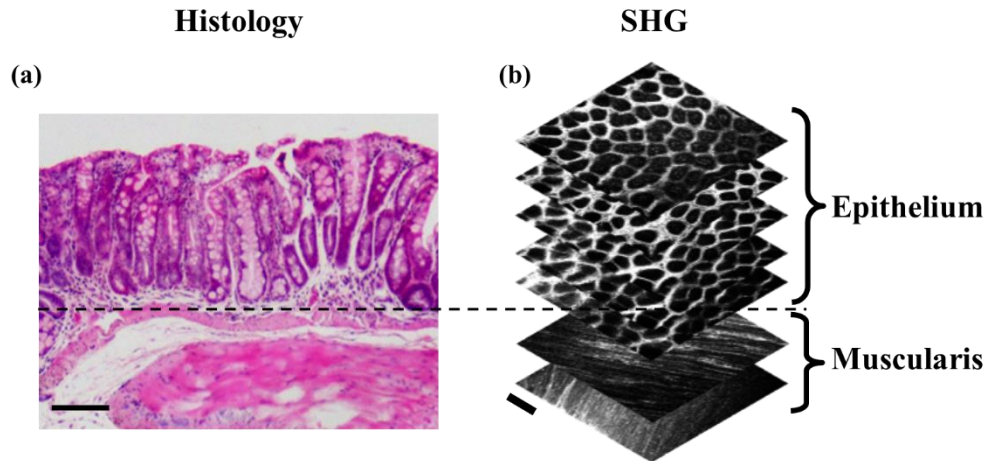
Figure 2. Comparison of histology and SHG images of Control murine colonic epithelium. (a) H&E stained transverse section of Control murine colonic epithelium; scale bar is 100 μm. Example of an SHG stack was shown, with images of depths at 20 μm, 40 μm, 60 μm, 80 μm, and 100 μm (epithelial layer), and 160 μm and 180 μm (muscularis layer), from top to bottom. Scale bar is 100 μm.
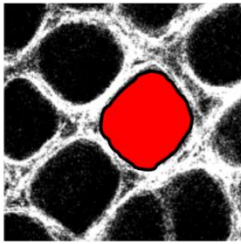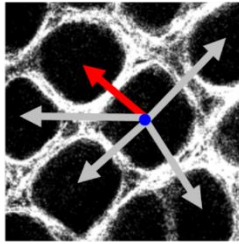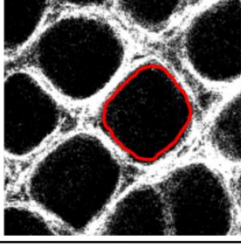
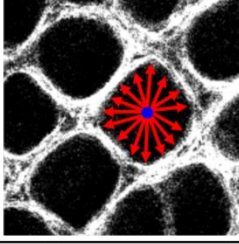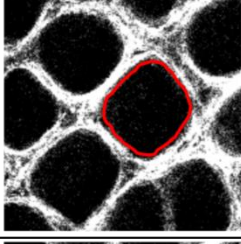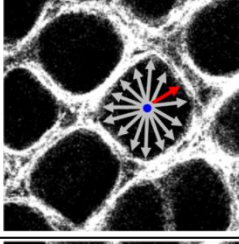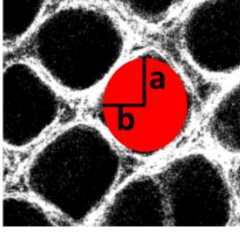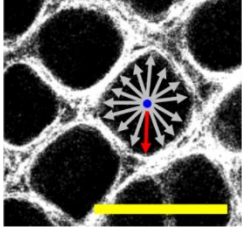**Optimization of automated crypt detection sensitivity**

In previous work, we developed an algorithm for determining optimal parameters for binarizing grayscale images of colon epithelium [23, 24]. The image intensities were re-scaled between 0 and 1, and the thresholds for binarizing were optimized for maximizing the ability of the algorithm to segment crypts can vary depending on the strength of the SHG signal in the tissue (details are included in Supplemental Information). The selected optimal parameters for the SHG image data set was calculated to have a 67% crypt detection sensitivity (CDS), when compared to manual selection of crypt locations.

Quantification of crypt image segmentation

Following the optimization of the threshold combinations for the algorithm's % CDS, the optimized algorithm was applied to the image set and the images were converted into a binary image, where white objects were defined as the detected crypt structures [23, 24]. Figure 3 summarizes the image features that were quantified, as well provides a visual representation of the calculation. Details of the image segmentation algorithm are included in Supplemental Information. Early stages of CRC typically include regions of abnormal morphology, for example, aberrant crypt foci (ACF) which are enlarged or non-tubular (branching) crypts, and/or multiple layers of cells lining a crypt [25, 26]. We chose to measure various crypt morphology image features related to changes viewed during histopathology, including crypt area, circularity, and distribution. The mean and standard deviation (referred to as variance in the results) of each image feature within each image were compared via a nested one-way ANOVA. The standard deviation of the image features within each image was calculated in order to measure the heterogeneity of the crypt structures; for example, tumor-adjacent regions tend to have both abnormally large and abnormally small crypt structures, which could produce a mean in a normal range, but the standard deviation of crypt areas within an image would retain the heterogeneous nature.

The results of the quantification of image features were then compared across cohorts: AOM early time point, AOM late time point, AOM-DSS early time point, AOM-DSS late time point, and Control. Nested one-way ANOVA with Tukey's post-test was used to determine statistically significant differences between the cohorts (JMP Pro 13).

Image Feature/Equation	Visual	Image Feature/Equation	Visual
Area Sum of pixels per crypt		Nearest Neighbor $min\ of\ \sqrt{(x_c - x_a)^2 + (y_c - y_a)^2}$	
Perimeter Sum of boundary pixels		Average Centroid Distance Function $\dfrac{\sum_{b=1}^{n} \sqrt{(x_c - x_b)^2 + (y_c - y_b)^2}}{n}$	
Circularity $\dfrac{4\pi Area}{Perimeter^2}$		Minimum Centroid Distance Function $min\ of\ \sqrt{(x_c - x_b)^2 + (y_c - y_b)^2}$	
Eccentricity $\sqrt{1 - \left(\dfrac{b}{a}\right)^2}$		Maximum Centroid Distance Function $max\ of\ \sqrt{(x_c - x_b)^2 + (y_c - y_b)^2}$	

Figure 3. Summary of quantitative image features. Each image feature is described with an equation and a visual representation of the calculation using an SHG image of normal epithelium; scale bar is 100 μm. For eccentricity, a represents half the length of the major axis, and b represents half the length of the minor axis. For nearest neighbor, (x_c, y_c) represents the centroid coordinate and (x_a, y_a) represent the centroid coordinates of adjacent crypts; the arrows represent the distance to adjacent crypts, the red arrow represents the distance selected as the nearest neighbor. For the centroid distance functions (CDF), (x_c, y_c) represents the centroid coordinate and (x_b, y_b) represent the boundary pixel coordinates. The average CDF was calculated by averaging all the distances to the boundary pixels (red arrows); the minimum CDF was calculated by selecting the distance to the closest boundary pixel (red arrow); the maximum CDF was calculated by selecting the distance to the furthest boundary pixel (red arrow).

Depth section image analysis

Each sample was imaged from 20 μm to 100 μm below the epithelial surface in 20 μm increments (Fig. 2); depth stacks were acquired from each sample at one to three locations on the tissue section. Regions in normal epithelium were selected randomly. Regions in AOM and AOM-DSS epithelium were selected adjacent to tumors; tumors were characterized as epithelial regions with SHG signal but no discernable crypt structures. These depth section images were then analyzed with the algorithm to quantify the previously described image features. The results were then compared across depths, as well as across AOM and AOM-DSS cohorts. Nested two-way ANOVA with Tukey's post-test was used to determine statistically significant differences between the cohorts (JMP Pro 13).

3. Results

Qualitative comparison of second harmonic generation images

Figure 4 shows examples of histology and SHG of both AOM and AOM-DSS murine models. Normal crypt structures tends to be uniform in size and general shape across the field of view, with crypt shape being tubular in transverse view (Fig. 4a) and roughly circular in *en face* view (Fig. 4b, h, i). Collagen distribution appears relatively even throughout the field of view (Fig. 4b, i). Crypt structures directly adjacent to tumor regions, or in regions of early dysplasia, tend to vary in size across a field of view, with one or more crypts being enlarged (Fig. 4c, d, k), and crypts often being oblong and/or having serrated edges in *en face* view (Fig. 4e). SHG images of grossly visible tumors do not show any discernable crypt structures (Fig. 4f, k).
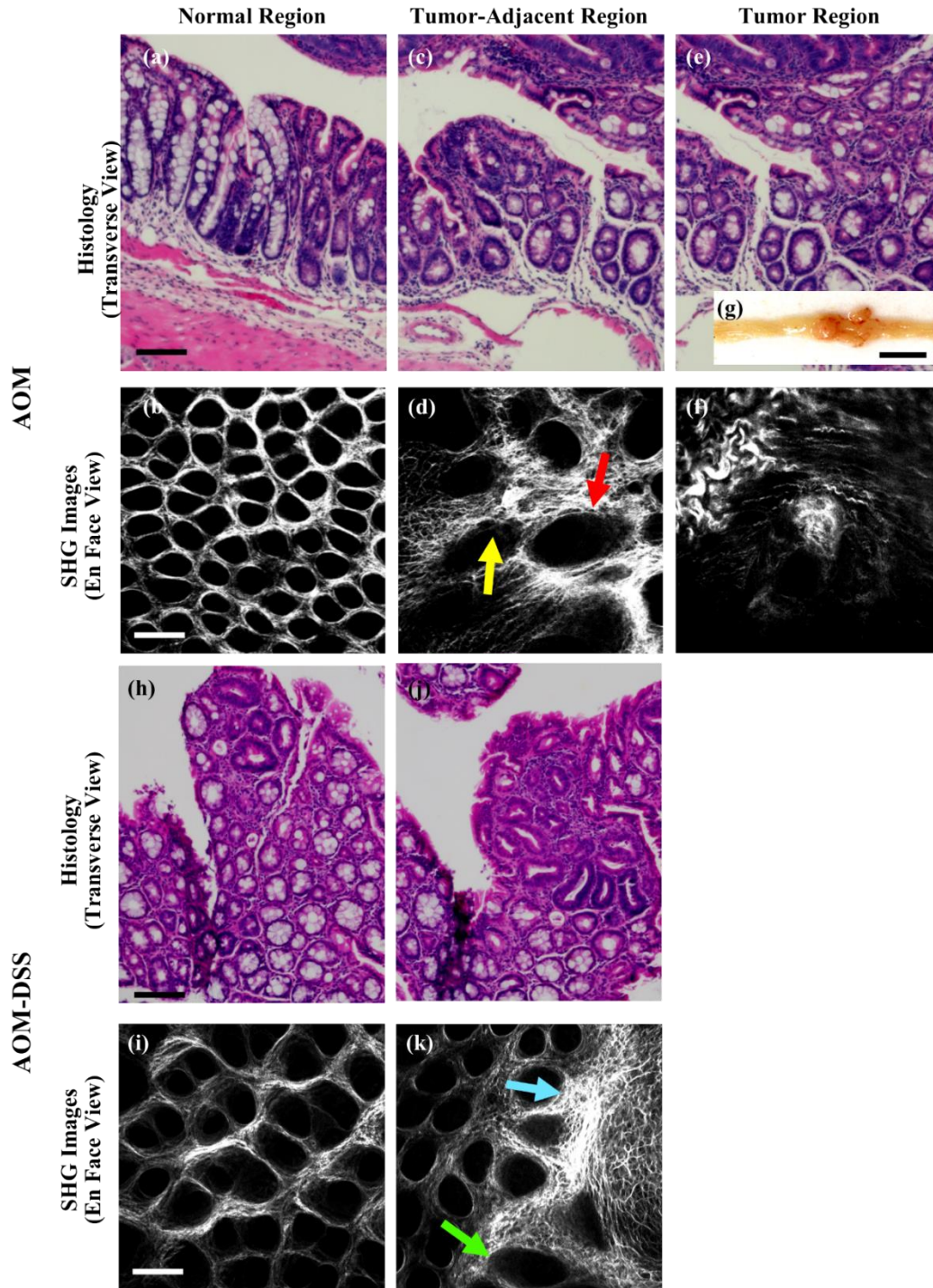
Figure 4. Examples of traditional H&E histology and SHG images of AOM and AOM-DSS murine tissue. (a,b,h,i) normal epithelium, (c,d,j,k) epithelium adjacent to a tumor, and (e,f) tumor region; all scale bars are 100 μm. (g) Image of a longitudinally sectioned AOM murine colon, exposing the epithelium and a grossly visible tumor; scale bar is 0.5 cm. (d) Red arrow points to an abnormally large crypt; yellow arrow points to an example of a serrated edge. (k) green arrow points to an enlarged crypt in the tumor-adjacent region; blue arrow point toward tumor edge. All images were manually contrast enhanced for display.

Increased mean distance between crypts in AOM vs. AOM-DSS cohorts

Nearest neighbor and crypt circularity image features showed significant differences between spontaneous CRC tumor and colitis-associated tumor models. Figure 5 shows statistically significant comparisons of the cohorts for the mean of the nearest neighbor (a), and the standard deviation (variance) of the nearest neighbor (b) and circularity (c). Results for all image features, including non-statistically significant, are included as Supplemental Figures. There was statistical significance when comparing AOM and AOM-DSS cohorts using nearest neighbor quantification (Fig. 5 a, b). Mean nearest neighbor was greater for AOM late and AOM-DSS early cohorts as compared to the Control (Fig. 5 a). AOM late cohort mean nearest neighbor was also greater than the AOM-DSS early cohort (Fig. 5 a). When comparing the variance of nearest neighbor, once again AOM late and AOM-DSS early cohorts had greater values than the Control (Fig. 5 b). The variance of the AOM late group was also significantly greater than the AOM-DSS late group (Fig. 5 b). Measuring the variance of circularity of the cohorts showed a difference between the AOM early cohort and the Control (Fig. 5 c).
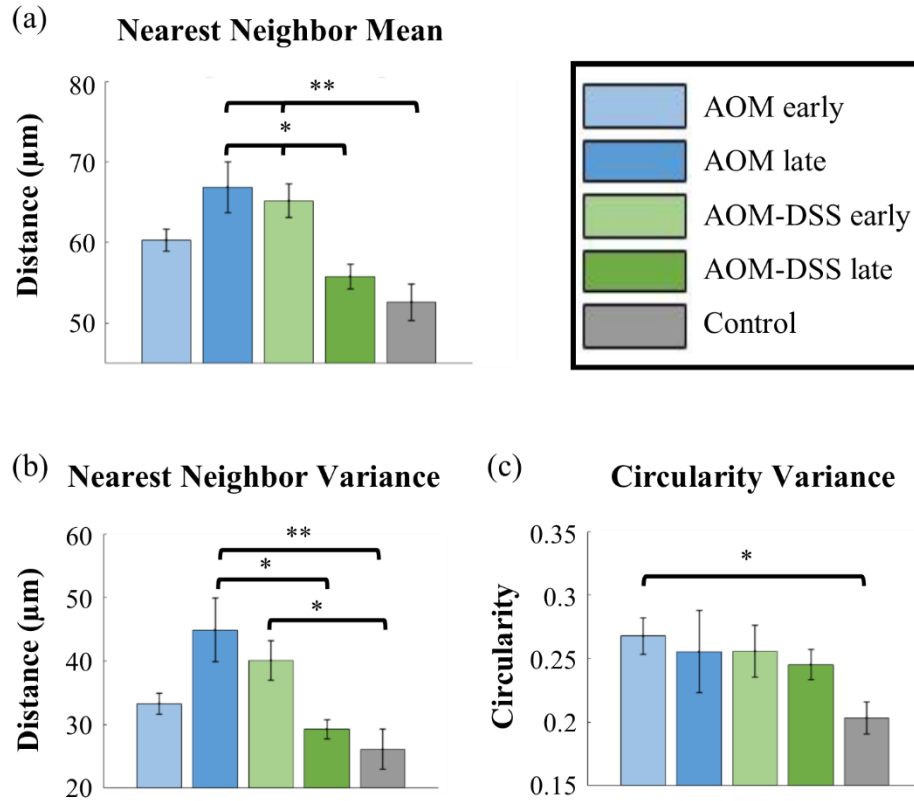
Figure 5. Mean values of nearest neighbor, and of the standard deviation of crypt nearest neighbor and circularity. Cohort n values (images): AOM early n=48, AOM late n=23, AOM-DSS early n=45, AOM-DSS late n=24, Control n=55. Error bars are standard error; significance was calculated via a nested one-way ANOVA with Tukey's HSD post-test. Significance was noted (*) for p values <0.05 and (**) for p values <0.01.

Differences in circularity and mean distance between crypts in tumor-bearing vs. Control cohorts at varying acquisition depths

As previously stated, images were taken at increasing depths: 20, 40, 60, 80, and 100 μm into the epithelial layer. We applied the image feature quantification algorithm to each depth, per treatment cohort. There were 43 image stacks (5 images in a stack, 20-100 μm) in total between all 5 cohorts. Mean and standard deviation of image features was compared across cohorts, at specific depths of acquisition (Fig. 6). As previously described, the mean and standard deviation (variance) within an image of each image feature was compared via a nested one-way ANOVA. Results for all image features with at least one statistically significant difference between two

cohorts are included as Supplemental Figures. There were significant differences between the

Control cohort and AOM cohorts, and Control and AOM-DSS cohorts, for mean nearest

neighbor at depth of specifically 40 μm, as well as standard deviation of circularity at a depth of

specifically 60 μm, when comparing image stacks. No image feature showed significant

differences between the AOM early and AOM late cohorts, nor the AOM early and AOM-DSS

early cohorts (Fig. 6 a-c).
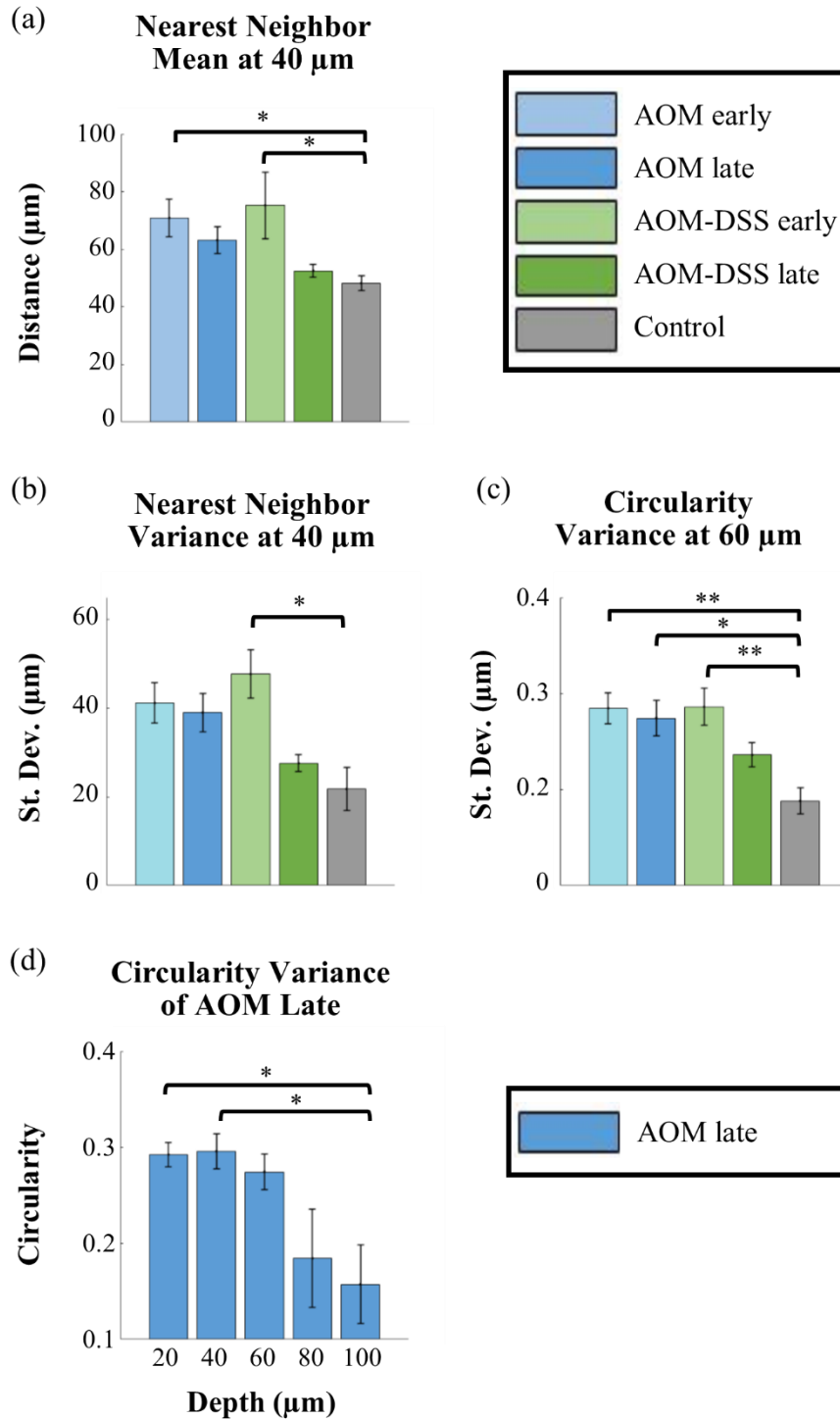
Figure 6. (a, b) Mean and standard deviation of crypt nearest neighbors at 40 μm depth. (c) Standard deviation of crypt circularities at 60 μm depth. (d) Standard deviation of crypt circularity at a range of imaging depths in microns, for AOM late cohort. Cohort n values (stacks): AOM early n=8, AOM late n=9, AOM-DSS early n=5, AOM-DSS late n=12, Control n=9. Significance was calculated via two-way ANOVA with Tukey's post-test. Error bars are standard error. Significance was noted (*) for p values <0.05 and (**) for p values <0.01.

Decreased crypt circularity at increased acquisition depth for AOM late cohort

As previously stated, images were taken at increasing depths: 20, 40, 60, 80, and 100 μm into the epithelial layer. Mean and standard deviation of image features was compared across depth of acquisition within each cohort (Fig. 6 d) via a nested one-way ANOVA. Results for all image features with at least one statistically significant difference between two cohorts are included as Supplemental Figures. There was no significance for mean of image features within cohorts; there was significance within the AOM late cohort for standard deviation of circularity (Fig. 6 d). There were differences between 100 μm and the more superficial 20 and 40 μm, for standard deviation of circularity of the AOM late cohort.

4. Discussion

Various modalities of endoscopic imaging have emerged with the goal of improving early detection of flat or discolored lesions, such as chromoendoscopy, narrow band imaging, and laser microendoscopy [14, 27]. Chromoendoscopy consists of spraying a colorimetric stain, such as indigo carmine, to provide contrast during colonoscopy [28]. Narrow band imaging has been described as label-free chromoendoscopy, as the optical filters only allow imaging small range of wavelengths, which enhance contrast in blood vessels and capillary patterns without the need for a contrast agent [27, 28]. While chromoendoscopy and narrow band imaging have shown promise for improving detection of dysplastic/neoplastic lesions, they are not able to distinguish between the similar structures of ALM and DALM lesions [14]. Laser confocal microendoscopy features high spatial resolution - able to resolve cellular and subcellular structures - providing more detailed imaging features that relate more closely to histopathological features [11]. The Cellvizio® confocal laser microendoscopy system showed potential in differentiating between DALM lesions and adjacent normal colorectal epithelial crypt structure in a preliminary clinical

trial [29]. Inserting the Cellvizio® endoscopic probe into an existing working channel during colonoscopy showed that DALM regions had enlarged crypts, increased irregularly in the distribution of crypts, increased space between crypts, as well as crypt destruction or fusion [29]. In contrast to confocal laser microendoscopy, multiphoton microendoscopy has additional benefits, including the ability to acquire label-free images of structural/morphological information (via SHG imaging) as well as insight into metabolic information (via autofluorescence of intrinsic biomolecules, such as nicotinamide adenine dinucleotide and flavin adenine dinucleotide, among others) up to several hundred microns in depth [30-33].

SHG imaging, as shown in this manuscript, is well-suited for characterization of collagen structures, especially collagen type I which makes up much of extracellular matrix and connective tissues [30, 34]. SHG imaging of colorectal epithelium highlights crypt shape, as the collagen fibers provide structure surrounding the cellular arrangement without the need for any exogenous contrast agent [35]. We have described our analysis of colorectal epithelial microstructure from SHG images of freshly resected murine colons using automated quantification of morphological image features. These results - a comparison of quantified features of crypt morphology (especially nearest neighbor and circularity) - demonstrated the ability of our quantitative image feature algorithms to detect differences between spontaneous (AOM model) and colitis-associated (AOM-DSS model) murine colorectal tissue specimens. Limitations of SHG imaging include the ability to acquire structural but not cellular information, as well as the need for clinician/investigator judgement to recognize some additional parameters during imaging, such as the presence of tumors which are not detected nor measured by the automated quantification algorithm.

Future work in this area will include murine models of familial adenomatous polyposis, and other hereditary models, to more thoroughly investigate the morphological features of the most common types of CRC. A common murine model of familial adenomatous polyposis - featuring a deletion of the *APC* gene - develop spontaneous adenomas in the colon, although these lesions may not fully exhibit the physiological features of the disease as seen in humans [36]. Despite some limitations, the *APC/min* mouse model and other models will be included in future SHG imaging studies in order to expand the scope of the current work, which is limited to spontaneous and colitis-associated tumor development.

The image biomarkers in this study relate to crypt morphology features that are analogous to conventional endoscopic biopsy and histopathology: crypt shape, size and spatial distribution. Statistically significant differences between spontaneous tumor (AOM) and colitis-associated tumor (AOM-DSS) cohorts indicate that different models of tumor progression can potentially be quantified via SHG imaging, possibly distinguishing between early and late tumor progression. However, none of the image features - which are based solely on collagen-derived SHG signal - in this study showed statistical differences within tumor-bearing cohorts, or between early and late time points of AOM cohorts. It is possible that combining SHG data with autofluorescence imaging data could be a promising technique for acquiring intraoperative complementary data in order to improve endoscopic differentiation between ALM and DALM lesions in patients with UC, but this would require additional study.

These results provide a quantitative model of the morphological changes that crypts undergo during dysplastic transformation, and can serve to guide future translational investigation and clinical studies in patients with IBD, with the long-term goal of reducing morbidity associated with prophylactic colectomy.

Conclusion

A number of factors contribute to dysplastic transformation in colon epithelium, and it is important to fully understand disease progression in order to improve techniques and tools for screening, diagnosis, and treatment. While studies of collagen fiber structure using optical imaging in cancers such as cervical have been conducted [18], investigation of collagen structures in murine CRC studies has been understudied [37]. Multiphoton endoscopic imaging has shown to be a feasible technology for clinical translation due to its miniaturization and label-free image acquisition. The introduction of image analysis algorithms into computer-aided diagnostic methods yield complementary data to conventional endoscopic procedures, which could lead to improved clinical decision-making for patients with known IBD. The methods described here provide insight into the ability of SHG imaging to yield relevant data about the crypt microstructure in colorectal epithelium, specifically the potential to distinguish between ALM and DALM murine models using quantification of crypt shape and distribution, informing future design of translational multiphoton imaging systems and protocols.

References

[1] S. P. Prieto, C. L. Reed, H. M. James, K. P. Quinn and T. J. Muldoon, "Differences in colonic crypt morphology of spontaneous and colitis-associated murine models via second harmonic generation imaging to quantify colon cancer development," *Manuscript Submitted for Publication. BMC Cancer,* 2018.

[2] N. A. Molodecky, I. S. Soon, D. M. Rabi, W. A. Ghali, M. Ferris, G. Chernoff, E. I. Benchimol, R. Panaccione, S. Ghosh, H. W. Barkema and G. G. Kaplan, "Increasing incidence and prevalence of the inflammatory bowel diseases with time, based on systematic review," *Gastroenterology,* vol. 142, *(1),* pp. 46-54, Jan, 2012.

[3] D. K. Podolsky, "Inflammatory bowel disease," N. Engl. J. Med., vol. 325, (13), pp. 928-937, 1991.

[4] W. J. Hogan, G. T. Hensley and J. E. Geenen, "Endoscopic evaluation of inflammatory bowel disease," Med. Clin. North Am., vol. 64, (6), pp. 1083-1102, Nov, 1980.

[5] H. Goldman, "Significance and detection of dysplasia in chronic colitis," Cancer: Interdisciplinary International Journal of the American Cancer Society, vol. 78, (11), pp. 2261-2263, 1996.

[6] C. J. Karvellas, R. N. Fedorak, J. Hanson and C. K. Wong, "Increased risk of colorectal cancer in ulcerative colitis patients diagnosed after 40 years of age," Canadian Journal of Gastroenterology and Hepatology, vol. 21, (7), pp. 443-446, 2007.

[7] A. Ekbom, C. Helmick, M. Zack and H. Adami, "Ulcerative colitis and colorectal cancer: a population-based study," N. Engl. J. Med., vol. 323, (18), pp. 1228-1233, 1990.

[8] A. J. Greenstein, D. B. Sachar, H. Smith, H. D. Janowitz and A. H. Aufses Jr, "A comparison of cancer risk in Crohn's disease and ulcerative colitis," Cancer, vol. 48, (12), pp. 2742-2745, 1981.

[9] D. C. Rubin, A. Shaker and M. S. Levin, "Chronic intestinal inflammation: inflammatory bowel disease and colitis-associated colon cancer," Frontiers in Immunology, vol. 3, pp. 107, 2012.

[10] T. Ullman, R. Odze and F. A. Farraye, "Diagnosis and management of dysplasia in patients with ulcerative colitis and Crohn's disease of the colon," Inflamm. Bowel Dis., vol. 15, (4), pp. 630-638, 2008.

[11] H. Neumann, M. Vieth, C. Langner, M. F. Neurath and J. Mudter, "Cancer risk in IBD: how to diagnose and how to manage DALM and ALM," World J. Gastroenterol., vol. 17, (27), pp. 3184-3191, Jul 21, 2011.

[12] R. D. Odze, F. A. Farraye, J. L. Hecht and J. L. Hornick, "Long-term follow-up after polypectomy treatment for adenoma-like dysplastic lesions in ulcerative colitis," Clinical Gastroenterology and Hepatology, vol. 2, (7), pp. 534-541, 2004.

[13] F. Shanahan, W. Weinstein and C. Bernstein, "Are we telling patients the truth about surveillance colonoscopy in ulcerative colitis?" The Lancet, vol. 343, (8889), pp. 71-74, 1994.

[14] R. Kiesslich, M. Goetz, K. Lammersdorf, C. Schneider, J. Burg, M. Stolte, M. Vieth, B. Nafe, P. R. Galle and M. F. Neurath, "Chromoscopy-guided endomicroscopy increases the diagnostic yield of intraepithelial neoplasia in ulcerative colitis," Gastroenterology, vol. 132, (3), pp. 874-882, 2007.

[15] P. Campagnola, "Second harmonic generation imaging microscopy: applications to diseases diagnostics," ACS Publications, 2011.

[16] D. M. Huland, C. M. Brown, S. S. Howard, D. G. Ouzounov, I. Pavlova, K. Wang, D. R. Rivera, W. W. Webb and C. Xu, "In vivo imaging of unstained tissues using long gradient index lens multiphoton endoscopic systems," Biomedical Optics Express, vol. 3, (5), pp. 1077-1085, 2012.

[17] H. Bao, A. Boussioutas, R. Jeremy, S. Russell and M. Gu, "Second harmonic generation imaging via nonlinear endomicroscopy," Optics Express, vol. 18, (2), pp. 1255-1260, 2010.

[18] Y. Zhang, M. L. Akins, K. Murari, J. Xi, M. J. Li, K. Luby-Phelps, M. Mahendroo and X. Li, "A compact fiber-optic SHG scanning endomicroscope and its application to visualize cervical remodeling during pregnancy," Proc. Natl. Acad. Sci. U. S. A., vol. 109, (32), pp. 12878-12883, Aug 7, 2012.

[19] F. Helmchen, M. S. Fee, D. W. Tank and W. Denk, "A miniature head-mounted two-photon microscope: high-resolution brain imaging in freely moving animals," Neuron, vol. 31, (6), pp. 903-912, 2001.

[20] D. R. Rivera, C. M. Brown, D. G. Ouzounov, I. Pavlova, D. Kobat, W. W. Webb and C. Xu, "Compact and flexible raster scanning multiphoton endoscope capable of imaging unstained tissue," Proc. Natl. Acad. Sci. U. S. A., vol. 108, (43), pp. 17598-17603, Oct 25, 2011.

[21] C. Neufert, C. Becker and M. F. Neurath, "An inducible mouse model of colon carcinogenesis for the analysis of sporadic and inflammation-driven tumor progression," Nature Protocols, vol. 2, (8), pp. 1998-2004, 2007.

[22] Y. Araki, K. Mukaisyo, H. Sugihara, Y. Fujiyama and T. Hattori, "Increased apoptosis and decreased proliferation of colonic epithelium in dextran sulfate sodium-induced colitis in mice," Oncol. Rep., vol. 24, (4), pp. 869-874, 2010.

[23] S. P. Prieto, K. K. Lai, J. A. Laryea, J. S. Mizell and T. J. Muldoon, "Quantitative analysis of ex vivo colorectal epithelium using an automated feature extraction algorithm for microendoscopy image data," Journal of Medical Imaging, vol. 3, (2), pp. 024502, 2016.

[24] S. P. Prieto, K. K. Lai, J. A. Laryea, J. S. Mizell, W. C. Mustain and T. J. Muldoon, "Fluorescein as a topical fluorescent contrast agent for quantitative microendoscopic inspection of colorectal epithelium," Biomedical Optics Express, vol. 8, (4), pp. 2324-2338, 2017.

[25] C. Kozlowski, S. Jeet, J. Beyer, S. Guerrero, J. Lesch, X. Wang, J. Devoss and L. Diehl, "An entirely automated method to score DSS-induced colitis in mice by digital image analysis of pathology slides," Dis. Model. Mech., vol. 6, (3), pp. 855-865, May, 2013.

[26] T. Takayama, S. Katsuki, Y. Takahashi, M. Ohi, S. Nojiri, S. Sakamaki, J. Kato, K. Kogawa, H. Miyake and Y. Niitsu, "Aberrant crypt foci of the colon as precursors of adenoma and cancer," N. Engl. J. Med., vol. 339, (18), pp. 1277-1284, 1998.

[27] H. Machida, Y. Sano, Y. Hamamoto, M. Muto, T. Kozu, H. Tajiri and S. Yoshida, "Narrow-band imaging in the diagnosis of colorectal mucosal lesions: a pilot study," Endoscopy, vol. 36, (12), pp. 1094-1098, Dec, 2004.

[28] W. Curvers, L. Baak, R. Kiesslich, A. Van Oijen, T. Rabenstein, K. Ragunath, J. F. Rey, P. Scholten, U. Seitz, F. Ten Kate, P. Fockens and J. Bergman, "Chromoendoscopy and narrow-band imaging compared with high-resolution magnification endoscopy in Barrett's esophagus," Gastroenterology, vol. 134, (3), pp. 670-679, Mar, 2008.

[29] G. D. De Palma, S. Staibano, S. Siciliano, F. Maione, M. Siano, D. Esposito and G. Persico, "In-vivo characterization of DALM in ulcerative colitis with high-resolution probe-based confocal laser endomicroscopy," World J. Gastroenterol., vol. 17, (5), pp. 677-680, Feb 7, 2011.

[30] S. Roth and I. Freund, "Second harmonic generation in collagen," J. Chem. Phys., vol. 70, (4), pp. 1637-1643, 1979.

[31] R. Sepehr, K. Staniszewski, S. Maleki, M. Ranji, E. R. Jacobs and S. Audi, "Optical imaging of tissue mitochondrial redox state in intact rat lungs in two models of pulmonary oxidative stress," J. Biomed. Opt., vol. 17, (4), pp. 046010, 2012.

[32] A. J. Walsh and M. C. Skala, "An automated image processing routine for segmentation of cell cytoplasms in high-resolution autofluorescence images," in Multiphoton Microscopy in the Biomedical Sciences XIV, 2014, pp. 89481M.

[33] S. Zhuo, J. Chen, G. Wu, S. Xie, L. Zheng, X. Jiang and X. Zhu, "Quantitatively linking collagen alteration and epithelial tumor progression by second harmonic generation microscopy," Appl. Phys. Lett., vol. 96, (21), pp. 213704, 2010.

[34] I. Freund, M. Deutsch and A. Sprecher, "Connective tissue polarity. Optical second-harmonic microscopy, crossed-beam summation, and small-angle scattering in rat-tail tendon," Biophys. J., vol. 50, (4), pp. 693-712, Oct, 1986.

[35] S. Zhuo, X. Zhu, J. Chen, S. Xie and G. Wu, "Quantitative biomarkers of colonic dysplasia based on intrinsic second-harmonic generation signal," J. Biomed. Opt., vol. 16, (12), pp. 120501, 2011.

[36] A. R. Moser, H. C. Pitot and W. F. Dove, "A dominant mutation that predisposes to multiple intestinal neoplasia in the mouse," Science, vol. 247, (4940), pp. 322-324, Jan 19, 1990.

[37] S. Wang, J. Chen, Y. Yang, W. Jiang, C. Feng, G. Guan, S. Zhuo and Z. Chen, "Assessment of tumor invasion depth in colorectal carcinoma using multiphoton microscopy," IEEE Photonics Journal, vol. 7, (2), pp. 1-8, 2015.

Chapter VI: Conclusion

       Optical imaging is an active field of investigation for biomedical engineers providing a variety of applications, from low-cost point-of-care systems to highly sensitive multiphoton imaging systems. Oral and colon cancer – epithelial cancers – have unique cellular morphologies that can be analyzed with optical imaging, ranging from histopathological imaging to investigative imaging systems.

1. Proflavine as a contrast agent for oral cell cytology

       Oral cancer, specifically oral squamous cell carcinoma (OSCC), is the sixth most common cancer worldwide and most prevalent in low-resource countries and locations, such as rural Bangladesh, India, and Sri Lanka [1-4]. The prevalence of chewing betel and other carcinogens puts people living in these locations at high-risk of developing OSCC, contributing up to 25% of all new cancer cases in males [4]. There have been a variety of investigations designed to reach these populations, but they rely heavily on volunteers and visual inspection [2, 5, 6]. Oral screening procedures designed to collect and analyze exfoliated cells have been investigated since 1963, but had poor sensitivity and specificity until the development of the cytobrush (designed for cervical smears) in the 1980s [7-10]. The OralCDx is an oral brush and computer-aided laboratory analysis based in the United States, which allows clinicians to collect cells from the entirety of the oral epithelium (including the basal layer) and the brush is sent to the laboratory for processing [11, 12]. The analysis is conducted on H&E stained cells using a specialized image processing system, and a cytopathologist makes the final diagnosis, and the OralCDx has shown over 90% specificity and sensitivity [11, 12]. A similar system could be a viable option for screening of oral lesions in high-risk populations.

We acquired images using proflavine and fluorescence imaging, and discernable morphological structures included clearly defined nuclei, Golgi zones, and visible cellular membranes. The use of proflavine in oral cell cytology and quantification of the image features had not been previously investigated. From a morphological standpoint, OSCC stained with proflavine was distinguishable due to its size, and much larger nuclear-to-cytoplasm ratio. Quantitative analysis of this nuclear-to-cytoplasm ratio showed that nuclear-to-cytoplasm ratio was significantly larger in OSCC cells than normal cells, with OSCC displaying an average ratio of approximately 0.8 and normal cells an average ratio of less than 0.1. Our results showed that proflavine was a suitable alternative for fluorescence imaging of OSCC cells; proflavine highlighted similar morphological features to clinical cytological stains; and quantification of nuclear-to-cytoplasmic ratios showed significantly larger ratios for OSCC [13].

Limitations of many of the OSCC screening studies in low-resource locations has been compliance in travelling to a clinic (e.g. ~50% in the Indian sub-continent), despite the offer of reimbursement for time and travel [6]. In addition, exfoliation of oral cells has shown mixed results, and is often considered most viable when the oral brushes can collect cells deep enough into the epithelial layer to collect cells from the basal layer [14], however this can be painful. Additionally, a limitation for optical imaging is the compromise between resolution of morphological structure and field-of-view; imaging setups can usually either image subcellular level detail or image a large number of cells in a short amount of time, but not both. In order to ensure that OSCC cells are not undercounted due to reduced field-of-view, it would be important for any clinical system to test the number of basal and OSCC cells that can be acquired and imaged through oral exfoliation, in a clinical study.

Proflavine could be considered in future point-of-care optical device design with the incorporation of computer-aided image segmentation in order to measure image features, for example nuclear-to-cytoplasm ratio as we have showed, to create systems for rapid analysis of exfoliated oral cells. A recent study showed that 74% of subjects experienced no or mild discomfort due to the Orcellex cytobrush and produced on average 55,500 cells per slide, including cells from all layers of the epithelium, such as basal (deep), spinosal (middle) and superficial cells [15]. This shows that there is promise for cytobrush oral cell acquisition with minimal pain, high cell count, and high cell diversity. A one-step proflavine staining method could be used to qualitatively inspect cells in these systems via a similar approach to the aforementioned Orcellex, OralCDx, or in studies with additional morphological parameters such as a study by Remmerbach et. al. [16]. They proposed another technique, where the combination of cellular morphology (including nuclear-to-cytoplasm ratio) and DNA-aneuploidy (extra or missing chromosomes) had increased sensitivity specificity compared to the OralCDx [16]. This study used both Papanicolau and Feulgen staining followed by automated segmentation of individual nuclei [16]. Therefore, future studies could consider proflavine as an alternative contrast agent for the analysis of a combination of cellular and nucleic morphology.

Automated quantification and count of OSCC could also aid in a quick read-out, and aid burden of training for volunteers in these high-risk settings. Also, a clear diagnosis based on optical image features might be a stronger motivator for compliance in going to a clinic, compared to the previously described study that flagged suspicious lesions, but required the patient to visit a hospital or clinic for biopsy and diagnosis. Advances in telemedicine also mean that future image acquisition could be reviewed and approved without requiring a secondary

visit, which could reduce the necessary workload for volunteers and reduce time between cancer detection and treatment.

2. Image feature quantification and alternative contrast agent for a translational microendoscopy system

Recurrence rates in colorectal cancer (CRC) are significant; 44% of stage II and III cases in one randomized study required additional surgery due to recurrence [17]. Due to the high risk of recurrence, patients who have undergone CRC-related surgery are placed under increased surveillance for early detection of additional tumors. Optical imaging devices that have studied early morphological changes include chromoendoscopy, narrow band imaging, and microendoscopic systems [18-23]. Fluorescence microendoscopic systems, similar to the one used in our studies, have shown over 90% sensitivity and specificity with trained observers classifying images acquired with a proflavine hemisulfate solution [24]. Automated quantification of images acquired with fluorescence microendoscopy could provide the clinician with additional parameters to make an informed decision. We designed a custom algorithm for crypt detection and image segmentation, and tested it using both proflavine and fluorescein – presented as an alternative contrast agent for microendoscopic systems [25, 26].

Morphological structures that are quantifiable using a fluorescent dye include crypt size and area. Our custom algorithm had an 85% crypt detection sensitivity with proflavine, and over 90% with fluorescein, and showed decreased area in crypt circularity for crypts in regions of adenocarcinoma [26]. While microendoscopic imaging studies have shown promise in qualitative image analysis of colorectal epithelium, quantitative analysis of crypt structure as biomarkers of carcinoma had not been explored for this type of system.

As mentioned previously, optical imaging compromises field-of-view for resolution; microendoscopic images can display clear crypt structures, but the field-of-view is approximately 1mm in diameter. In addition, microendoscopy can only image the surface of the epithelial layer, therefore any changes that occur in the base of the crypts are not acquired by the system. Future work will lie in the direction of an imaging system that combines imaging and another acquisition technique, such as the diffuse reflectance spectroscopy system in development by Greening et. al. that combines microendoscopy with diffuse reflectance for acquisition of hemoglobin and oxygenation biomarkers that are below the imaged surface [27].

The results of our custom algorithm using both proflavine and fluorescein could guide the implementation of automated image analysis quantification in microendoscopic imaging studies, such as the measurement of crypt area and circularity, which showed promise for differentiating normal and carcinoma epithelial regions. Additional parameters that could be tested using automated quantification include crypt count and distribution, and crypt homogeneity by measuring the variance/standard deviation of crypt area, and circularity in a field-of-view, as we applied in our manuscript on SHG imaging [28]. In addition, the use of topical fluorescein should be tested *in vivo* for rapid staining of colorectal tissue, similar to studies that have used intravenous fluorescein to image colorectal epithelium in CRC patients [29, 30].

Efficient image analysis software could be studied for future translation into *in vivo* clinical studies. Rapid quantification could provide clinicians with *in vivo* results for a less subjective determination of changes in crypt structure. Also, topical application of fluorescein could prove to be a more translatable fluorescent option for microendoscopic imaging systems designed for clinical use in complement to current imaging tools, since it is an FDA-approved contrast agent for intravenous use in ophthalmological imaging applications. A rapid imaging

152

system for screening of high-risk patients could aid in early detection of recurrent tumors and therefore improve survival rates of CRC patients.

3. Second harmonic generation imaging of murine epithelium for crypt morphology image feature analysis of spontaneous and colitis-associated colorectal tumors

Patients with ulcerative colitis (UC), a subtype of inflammatory bowel disease, have chronic inflammation of the gastrointestinal tract and have been considered at increased risk for CRC. Approximately 29% of UC patients develop CRC within 10 years of diagnosis [31-34]. The curative standard in UC patients are partial or complete colectomies when malignant lesions develop in the colorectal tract [35, 36]. Studies show that UC patients can develop polyps that are similar to spontaneous polyps developed in patients with no history of inflammatory disease, and can be treated less aggressively than colitis-associated lesions [19, 36]. Therefore, there have been a variety of devices and studies designed to distinguish between an adenoma-like mass (ALM), which can be treated with a less invasive polypectomy, and dysplasia-associated lesion or mass (DALM), which necessitates a more invasive surgery [19, 36]. Examples of such modalities include chromoendoscopy and confocal endomicroscopy systems [19, 30]. Multiphoton imaging systems have additional advantages, including acquisition of functional data acquired from endogenous autofluorescence (e.g. cellular metabolic biomarkers including redox ratios) instead of exogenous contrast agents. These advantages have led to the miniaturization of multiphoton systems, which have been designed to be used endoscopically [37, 38]. Multiphoton imaging allows for not only fluorescence imaging, which provides functional data, but second harmonic generation (SHG) imaging, which can provide information of structural collagen [39]. While collagen structures in various types of cancers, including

cervical and breast, have been investigated using SHG, there has not been extensive study in SHG imaging of CRC [37, 38, 40].

One approach to imaging of spontaneous and colitis-associated lesions is second harmonic imaging (SHG) for analysis of collagen structures in colorectal epithelium. We used A/J mice in two murine tumor models, azoxymethane (AOM) and azoxymethane followed by rounds of dextran sodium sulfate salt (AOM-DSS), in order to acquire preliminary results of the viability of using SHG for analysis of changes in crypt structure. We also acquired images from early and late time points (20-24 weeks and 24-28 weeks post-first-AOM injection, respectively). Our results showed that the nearest neighbor image feature, the distance between each crypt center and its nearest crypt center, was the most promising quantitative metric for distinguishing between cohorts [26]. The average nearest neighbor distances were greater for the AOM late cohort when compared to AOM-DSS early and late cohorts, while the standard deviation of nearest neighbor distances showed an increased heterogeneity in AOM late cohort when compared to AOM-DSS late and Control cohorts. Quantitative analysis of crypt features, specifically nearest neighbor, showed the potential for SHG imaging to be used as a complementary tool in distinguishing between ALM and DALM regions.

A disadvantage of using SHG is that the signal is predominantly forward-scattering, therefore the backscattered signal is dim. The multiphoton imaging system is very sensitive to movement and can take up to three seconds to acquire an image, which, combined with a small field-of-view (522x522 μm), makes it difficult to rapidly scan large sections of the colon. Alternative approaches to scanning of two-photon excitation, such as temporally focused two-photon endomicroscopy, have been studied in order to reduce acquisition time, but they have their own limitations that must be validated and implemented, such as development of custom

154

fibers (e.g. hollow core photonic crystal) that can withstand increased power without damage [41]. If alternatives that reduce acquisition time can be implemented in miniaturized multiphoton systems, multiphoton imaging would be effective when used as an optical biopsy to further inspect grossly suspicious regions during surveillance.

SHG and quantitative analysis of image features, such as nearest neighbor, could serve as a complementary dataset in studies using miniaturized multiphoton systems. The results of our quantification could guide future multiphoton studies of ALM and DALM murine models, such as *in vivo* studies to determine efficacy of combining autofluorescence and SHG acquisition for differentiation of lesions, as well as to more thoroughly understand the morphological changes that occur in crypts in ALM versus DALM tumors.

Combined with additional image features, SHG imaging could eventually aid clinicians in determining lesion type and optimal treatment in UC patients. Automated quantification of SHG image features could potentially contribute toward better-informed clinical decisions during screening and diagnosis of suspicious lesions and polyps during surveillance. Accurate and rapid assessment of lesions would decrease time in surgery, the need for additional surgeries, and prevent unnecessary colectomies.

4. Concluding remarks

Optical imaging modalities designed for imaging of epithelial cancer, specifically oral and colorectal, have been widely studied due to their wide range of applications. Contrast agents are a crucial component of optical imaging design, whether exogenous or endogenous. We analyzed the morphology of oral and colorectal epithelium in order to test alternative contrast agents and the viability of computer-aided quantification in various optical imaging modalities aimed at cancer detection. Cancer diagnosis, surveillance, and treatment can benefit from systems

designed to reduce invasiveness, turn-around time, and interobserver variability, as well as

increase detection at early stages and therefore increase survival rates.

References

[1] R. Mehrotra, "The role of cytology in oral lesions: a review of recent improvements," *Diagn. Cytopathol.,* vol. 40, *(1),* pp. 73-83, 2012.

[2] M. C. Downer, D. R. Moles, S. Palmer and P. M. Speight, "A systematic review of measures of effectiveness in screening for oral cancer and precancer," *Oral Oncol.,* vol. 42, *(6),* pp. 551-560, 2006.

[3] S. V. K. Rao, G. Mejia, K. Roberts-Thomson and R. Logan, "Epidemiology of oral cancer in Asia in the past decade-an update (2000-2012)," *Asian Pacific Journal of Cancer Prevention,* vol. 14, *(10),* pp. 5567-5577, 2013.

[4] S. Warnakulasuriya, "Global epidemiology of oral and oropharyngeal cancer," Oral Oncol., vol. 45, (4-5), pp. 309-316, 2009.

[5] R. Akhter, N. M. M. Hassan, J. Aida, S. Takinami and M. Morita, "Relationship between betel quid additives and established periodontitis among Bangladeshi subjects," J. Clin. Periodontol., vol. 35, (1), pp. 9-15, 2008.

[6] R. S. Wesley, V. R. Kutty, B. Matthew, R. Sankaranarayanan and M. K. Nair, "Economic comparison of two strategies of oral cancer screening," Health Policy Plan., vol. 7, (3), pp. 284-289, 1992.

[7] B. Majer, B. Laky, S. Knasmüller and F. Kassie, "Use of the micronucleus assay with exfoliated epithelial cells as a biomarker for monitoring individuals at elevated risk of genetic damage and in chemoprevention trials," Mutation Research/Reviews in Mutation Research, vol. 489, (2), pp. 147-172, 2001.

[8] O. Kujan, M. Desai, A. Sargent, A. Bailey, A. Turner and P. Sloan, "Potential applications of oral brush cytology with liquid-based technology: results from a cohort of normal oral mucosa," Oral Oncol., vol. 42, (8), pp. 810-818, 2006.

[9] H. C. Sandler, "Veterans Administration cooperative study of oral exfoliative cytology," Acta Cytol., vol. 7, pp. 180-182, May-Jun, 1963.

[10] P. J. Murata, R. A. Johnson and K. E. McNicoll, "Controlled evaluation of implementing the Cytobrush technique to improve Papanicolaou smear quality," Obstet. Gynecol., vol. 75, (4), pp. 690-695, Apr, 1990.

[11] J. J. Sciubba and US Collaborative OralCDx Study Group, "Improving detection of precancerous and cancerous oral lesions: computer-assisted analysis of the oral brush biopsy," J. Am. Dent. Assoc., vol. 130, (10), pp. 1445-1457, 1999.

[12] C. Scheifele, A. Schmidt-Westhausen, T. Dietrich and P. A. Reichart, "The sensitivity and specificity of the OralCDx technique: evaluation of 103 cases," Oral Oncol., vol. 40, (8), pp. 824-828, 2004.

[13] S. P. Prieto, A. J. Powless, J. W. Boice, S. G. Sharma and T. J. Muldoon, "Proflavine Hemisulfate as a Fluorescent Contrast Agent for Point-of-Care Cytology," PloS One, vol. 10, (5), pp. e0125598, 2015.

[14] S. Divani, M. Exarhou, T. Leonidas-Nectarios, D. Georgantzis and H. Skoulakis, "Advantages and difficulties of brush cytology in the identification of early oral cancer," Archive of Oncology, vol. 17, (1-2), pp. 11-12, 2009.

[15] O. Kujan, M. N. Pemberton, M. Schwarz and P. Sloan, "Evaluation of an innovative oral brush for potential applications using liquid based cytology," J. Oral Sci., vol. 60, (1), pp. 45-50, 2018.

[16] T. W. Remmerbach, H. Weidenbach, N. Pomjanski, K. Knops, S. Mathes, A. Hemprich and A. Böcking, "Cytologic and DNA-cytometric early diagnosis of oral cancer," Analytical Cellular Pathology, vol. 22, (4), pp. 211-221, 2001.

[17] R. M. Goldberg, T. R. Fleming, C. M. Tangen, C. G. Moertel, J. S. Macdonald, D. G. Haller and J. A. Laurie, "Surgery for recurrent colon cancer: strategies for identifying resectable recurrence and success rates after resection," Ann. Intern. Med., vol. 129, (1), pp. 27-35, 1998.

[18] R. Kiesslich, M. Goetz, K. Lammersdorf, C. Schneider, J. Burg, M. Stolte, M. Vieth, B. Nafe, P. R. Galle and M. F. Neurath, "Chromoscopy-guided endomicroscopy increases the diagnostic yield of intraepithelial neoplasia in ulcerative colitis," Gastroenterology, vol. 132, (3), pp. 874-882, 2007.

[19] H. Neumann, M. Vieth, C. Langner, M. F. Neurath and J. Mudter, "Cancer risk in IBD: how to diagnose and how to manage DALM and ALM," World J. Gastroenterol., vol. 17, (27), pp. 3184-3191, Jul 21, 2011.

[20] H. Neumann, R. Kiesslich, M. B. Wallace and M. F. Neurath, "Confocal laser endomicroscopy: technical advances and clinical applications," Gastroenterology, vol. 139, (2), pp. 388-92, 392.e1-2, Aug, 2010.

[21] A. Ishijima, S. Mondrik, R. A. Schwarz, N. Vigneswaran, A. M. Gillenwater and R. Richards-Kortum, "Automated frame selection process for analyzing high resolution microendoscope images," in SPIE Translational Biophotonics, 2014, pp. 91551M-91551M-4.

[22] P. M. Lane, S. Lam, A. McWilliams, M. W. Anderson and C. E. MacAulay, "Confocal fluorescence microendoscopy of bronchial epithelium," J. Biomed. Opt., vol. 14, (2), pp. 024008-024008-10, 2009.

[23] P. M. Vila, C. W. Park, M. C. Pierce, G. H. Goldstein, L. Levy, V. V. Gurudutt, A. D. Polydorides, J. H. Godbold, M. S. Teng and E. M. Genden, "Discrimination of benign and neoplastic mucosa with a high-resolution microendoscope (HRME) in head and neck cancer," Annals of Surgical Oncology, vol. 19, (11), pp. 3534-3539, 2012.

[24] N. D. Parikh, D. Perl, M. H. Lee, B. Shah, Y. Young, S. S. Chang, R. Shukla, A. D. Polydorides, E. Moshier and J. Godbold, "In vivo diagnostic accuracy of high-resolution microendoscopy in differentiating neoplastic from non-neoplastic colorectal polyps: a prospective study," Am. J. Gastroenterol., vol. 109, (1), pp. 68-75, 2014.

[25] S. P. Prieto, K. K. Lai, J. A. Laryea, J. S. Mizell and T. J. Muldoon, "Quantitative analysis of ex vivo colorectal epithelium using an automated feature extraction algorithm for microendoscopy image data," Journal of Medical Imaging, vol. 3, (2), pp. 024502, 2016.

[26] S. P. Prieto, K. K. Lai, J. A. Laryea, J. S. Mizell, W. C. Mustain and T. J. Muldoon, "Fluorescein as a topical fluorescent contrast agent for quantitative microendoscopic inspection of colorectal epithelium," Biomedical Optics Express, vol. 8, (4), pp. 2324-2338, 2017.

[27] G. J. Greening, H. M. James, A. J. Powless, J. A. Hutcheson, M. K. Dierks, N. Rajaram and T. J. Muldoon, "Fiber-bundle microendoscopy with sub-diffuse reflectance spectroscopy and intensity mapping for multimodal optical biopsy of stratified epithelium," Biomedical Optics Express, vol. 6, (12), pp. 4934-4950, 2015.

[28] S. P. Prieto, C. L. Reed, H. M. James, K. P. Quinn and T. J. Muldoon, "Differences in colonic crypt morphology of spontaneous and colitis-associated murine models via second harmonic generation imaging to quantify colon cancer development," Manuscript Submitted for Publication. BMC Cancer, 2018.

[29] G. D. De Palma, "Confocal laser endomicroscopy in the "in vivo" histological diagnosis of the gastrointestinal tract," World J. Gastroenterol., vol. 15, (46), pp. 5770-5775, Dec 14, 2009.

[30] G. D. De Palma, S. Staibano, S. Siciliano, F. Maione, M. Siano, D. Esposito and G. Persico, "In-vivo characterization of DALM in ulcerative colitis with high-resolution probe-based confocal laser endomicroscopy," World J. Gastroenterol., vol. 17, (5), pp. 677-680, Feb 7, 2011.

[31] D. C. Rubin, A. Shaker and M. S. Levin, "Chronic intestinal inflammation: inflammatory bowel disease and colitis-associated colon cancer," Frontiers in Immunology, vol. 3, pp. 107, 2012.

[32] A. J. Greenstein, D. B. Sachar, H. Smith, H. D. Janowitz and A. H. Aufses Jr, "A comparison of cancer risk in Crohn's disease and ulcerative colitis," Cancer, vol. 48, (12), pp. 2742-2745, 1981.

[33] A. Ekbom, C. Helmick, M. Zack and H. Adami, "Ulcerative colitis and colorectal cancer: a population-based study," N. Engl. J. Med., vol. 323, (18), pp. 1228-1233, 1990.

[34] C. J. Karvellas, R. N. Fedorak, J. Hanson and C. K. Wong, "Increased risk of colorectal cancer in ulcerative colitis patients diagnosed after 40 years of age," Canadian Journal of Gastroenterology and Hepatology, vol. 21, (7), pp. 443-446, 2007.

[35] P. Munkholm, "The incidence and prevalence of colorectal cancer in inflammatory bowel disease," Aliment. Pharmacol. Ther., vol. 18, (s2), pp. 1-5, 2003.

[36] T. Ullman, R. Odze and F. A. Farraye, "Diagnosis and management of dysplasia in patients with ulcerative colitis and Crohn's disease of the colon," Inflamm. Bowel Dis., vol. 15, (4), pp. 630-638, 2008.

[37] Y. Zhang, M. L. Akins, K. Murari, J. Xi, M. J. Li, K. Luby-Phelps, M. Mahendroo and X. Li, "A compact fiber-optic SHG scanning endomicroscope and its application to visualize cervical remodeling during pregnancy," Proc. Natl. Acad. Sci. U. S. A., vol. 109, (32), pp. 12878-12883, Aug 7, 2012.

[38] D. R. Rivera, C. M. Brown, D. G. Ouzounov, I. Pavlova, D. Kobat, W. W. Webb and C. Xu, "Compact and flexible raster scanning multiphoton endoscope capable of imaging unstained tissue," Proc. Natl. Acad. Sci. U. S. A., vol. 108, (43), pp. 17598-17603, Oct 25, 2011.

[39] P. Campagnola, "Second harmonic generation imaging microscopy: applications to diseases diagnostics," ACS Publications, 2011.

[40] M. Bianchi, J. Adur, S. Ruff, M. Izaguirre, H. Carvalho, C. Cesar and V. Casco, "Analysis of the orientation of collagen fibers as a tool for the early detection of colorectal cancer," in VI Latin American Congress on Biomedical Engineering CLAIB 2014, Paraná, Argentina 29, 30 & 31 October 2014, 2015, pp. 365-368.

[41] H. Choi and P. T. So, "Improving femtosecond laser pulse delivery through a hollow core photonic crystal fiber for temporally focused two-photon endomicroscopy," Scientific Reports, vol. 4, pp. 6626, 2014.

Chapter VII: Appendix

IBC, IRB, IACUC approvals

UNIVERSITY OF ARKANSAS

Office of Research Compliance

April 29, 2014

MEMORANDUM

TO: Dr. Timothy Muldoon

FROM: W. Roy Penney
Institutional Biosafety Committee

RE: IBC Protocol Approval

IBC Protocol #: 14008

Protocol Title: "Imaging of morphologic features in exfoliated oral epithelial cells in saliva"

Approved Project Period: Start Date: August 8, 2013
Expiration Date: August 7, 2016

The Institutional Biosafety Committee (IBC) has approved the modification of Protocol 14008, "Imaging of morphologic features in exfoliated oral epithelial cells in saliva" You may begin your study.

If further modifications are made to the protocol during the study, please submit a written request to the IBC for review and approval before initiating any changes.

The IBC appreciates your assistance and cooperation in complying with University and Federal guidelines for research involving hazardous biological materials.

November 2, 2016

MEMORANDUM

TO:	Amy Powless Sandra Prieto Timothy Muldoon
FROM:	Ro Windwalker IRB Coordinator
RE:	PROJECT CONTINUATION & MODIFICATION
IRB Protocol #:	13-10-183
Protocol Title:	*Evaluation of a Microendoscopic Imaging System in Examination of Resected Tissues*
Review Type:	☒ EXEMPT ☐ EXPEDITED ☐ FULL IRB
Previous Approval Period:	Start Date: 10/18/2013 Expiration Date: 10/17/2016
New Expiration Date:	10/17/2017

Your request to extend and update the referenced protocol has been approved by the IRB. If at the end of this period you wish to continue the project, you must submit a request using the form *Continuing Review for IRB Approved Projects*, prior to the expiration date. Failure to obtain approval for a continuation on or prior to this new expiration date will result in termination of the protocol and you will be required to submit a new protocol to the IRB before continuing the project. Data collected past the protocol expiration date may need to be eliminated from the dataset should you wish to publish. Only data collected under a currently approved protocol can be certified by the IRB for any purpose.

This protocol has been approved for 54 total participants. If you wish to make *any* modifications in the approved protocol, including enrolling more than this number, you must seek approval *prior to* implementing those changes. All modifications should be requested in writing (email is acceptable) and must provide sufficient detail to assess the impact of the change.

If you have questions or need any assistance from the IRB, please contact me at 109 MLKG Building, 5-2208, or irb@uark.edu.

109 MLKG • 1 University of Arkansas • Fayetteville, AR 72701-1201 • (479) 575-2208 • Fax (479) 575-6527 • Email irb@uark.edu
The University of Arkansas is an equal opportunity/affirmative action institution.

161

Office of Research Compliance

To: Timothy Muldoon
FR: Craig Coon
Date: January 23rd, 2017
Subject: IACUC Approval
Expiration Date: June 9th, 2019

The Institutional Animal Care and Use Committee (IACUC) has APPROVED your protocol # **16064:** *Microstructural and metabolic features of colorectal adenocarcinoma*.

In granting its approval, the IACUC has approved only the information provided. Should there be any further changes to the protocol during the research, please notify the IACUC in writing (via the Modification form) prior to initiating the changes. If the study period is expected to extend beyond June 9th, 2019 you must submit a newly drafted protocol prior to that date to avoid any interruption. By policy the IACUC cannot approve a study for more than 3 years at a time.

The following individuals are approved to work on this study: Haley James, Sandra Prieto, David Zaharoff, Timothy Muldoon, Gage Greening, and David Zaharoff.   Please submit personnel additions to this protocol via the modification form prior to their start of work.

The IACUC appreciates your cooperation in complying with University and Federal guidelines involving animal subjects.

CNC/aem

Supplementary Information for Chapter 5 [1]

S1. Optimization of automated crypt detection sensitivity

In previous work, we developed an algorithm for determining optimal contrast-enhancing parameters for binarizing grayscale images of colon epithelium [2, 3]. The acquired second harmonic generation (SHG) images were re-scaled between 0 and 1, and the thresholds for binarizing were optimized for maximizing the ability of the algorithm to segment crypts, which can vary depending on the strength of the SHG signal in the tissue. Figure S1 shows an example of how different thresholds are optimal for different images. A range of thresholds were applied to the images, and the percent crypt detection sensitivity (% CDS) of each group was calculated against the manual selection of crypts by the authors, as done in previous work [2]. An example of the % CDS of various thresholds on SHG images of murine colonic tissue from azoxymethane-injected mice is shown in Fig. S1(e). The thresholds were values between 0 and 1, used to determine binarization based on all intensities greater than the threshold being converted to white and all intensities less than the threshold being converted to black. The thresholds we tested are smaller than 0.01 since the raw image intensities are low for back-scattered SHG signal. The threshold with highest overall % CDS was 0.0035 with 38% CDS.

Figure S1, specifically (a-d), also shows an example of how different thresholds are optimal for different images, thus affecting % CDS when a single threshold is chosen. Previous work showed that applying a range of thresholds to the images increased the % CDS of the algorithm [2, 3]. The detected crypts for each threshold were compared to the detected crypts of the previous threshold, and duplicates were excluded while newly-detected crypts were stored. In order to determine the optimal combination of thresholds, the algorithm applied various combinations of thresholds to the image set and calculated the % CDS of each combination.

Since thresholds between 0.003 and 0.005 showed % CDS higher than 20%, the range of tested combinations included thresholds between 0.0025 and 0.0055, in 0.0005 incremental steps. Thresholds were tested in combination of two, three, four, and five thresholds. The optimal combination of thresholds was determined to be a combination of three thresholds: 0.003, 0.0035, and 0.0045 was calculated to have a 67% CDS. Combinations of four or more thresholds increased % CDS to almost 69%, but also carry the potential for overtraining the algorithm with our data set, therefore the combination of three thresholds was selected. The selected optimal parameters for the SHG image data set was calculated to have a 67% crypt detection sensitivity (CDS), when compared to manual selection of crypt locations.
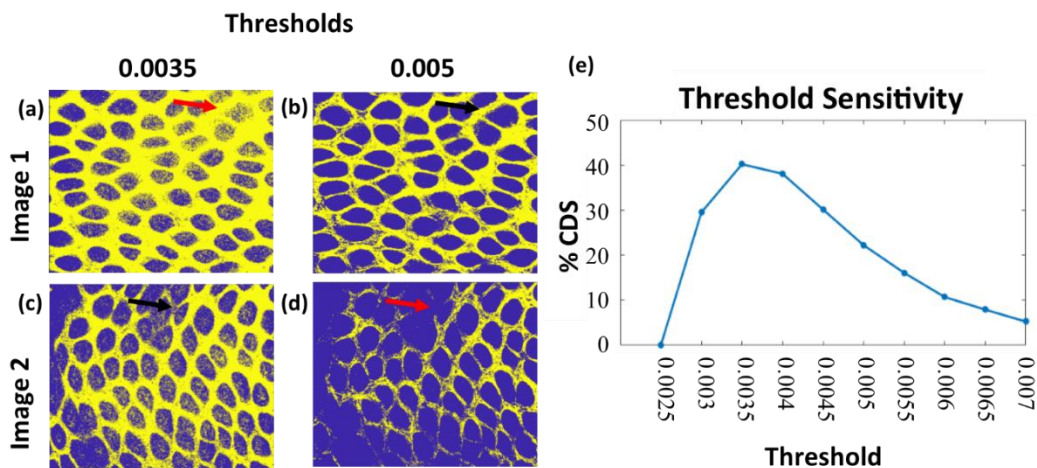
Figure S1. (a-d) Example of two images from Control mice, binarized using different thresholds. Yellow is SHG signal, blue is background. Red arrows point to crypts with uncertain definition at a given threshold; black arrows point to matching crypts that have clear definition at a different threshold. (e) Plot of percent crypt detection sensitivity (% CDS) of the algorithm at different threshold values.

S2. Selection of quantifiable image features

Crypt and cellular morphology are image features used by pathologists when determining a diagnosis for both spontaneous and colitis-associated tumors. Image features include enlarged or non-tubular crypt shapes, and/or crypts with more than a single layer of cells surrounding it.

Based on the crypt morphology changes that occur during tumor development, we tested various image morphology parameters for viability as indicators of colon cancer, specifically crypt shape, size, and distribution. We tested various image features in order to provide additional information for investigations using multiphoton endoscopic systems, but we acknowledge that there are limitations to SHG imaging and crypt morphology when analyzed independent of additional factors. For example, Figure S2 shows SHG images of Control tissue, as well as of AOM-DSS early and AOM-DSS late cohorts. Our crypt detection algorithm is designed to detect and analyze crypts, but tumors, such as the ones labelled with yellow arrows, are not recognized during automated analysis. There is still the need for the judgement of a clinician/investigator during the imaging process.

We describe SHG as a complementary optical imaging process to autofluorescence multiphoton imaging. There have been a number of studies on cancer imaging using autofluorescence imaging using endoscopic multiphoton systems [4]. An example of the combined effect of SHG and autofluorescence imaging of a Control tissue sample is shown in Figure S2. Autofluorescence imaging can acquire cellular and subcellular detail, while SHG imaging acquires detail of collagen structures. Autofluorescence in Fig. S2 was acquired using a multiphoton microscopy system (described on page 7 of the main manuscript) which uses a titanium-sapphire ultrafast femtosecond pulsed laser source (Mai Tai eHP, Spectra-Physics, CA, USA) which was set to 750nm excitation, and the signal was collected using a 466/40 bandpass filter (Semrock, NY, USA) and photomultiplier tube (H7422 PASO, Hamamatsu, Japan). We believe that the combination of SHG and autofluorescence imaging in endoscopic multiphoton studies of colorectal cancer could elucidate additional morphological changes and markers of neoplasia and cancer.
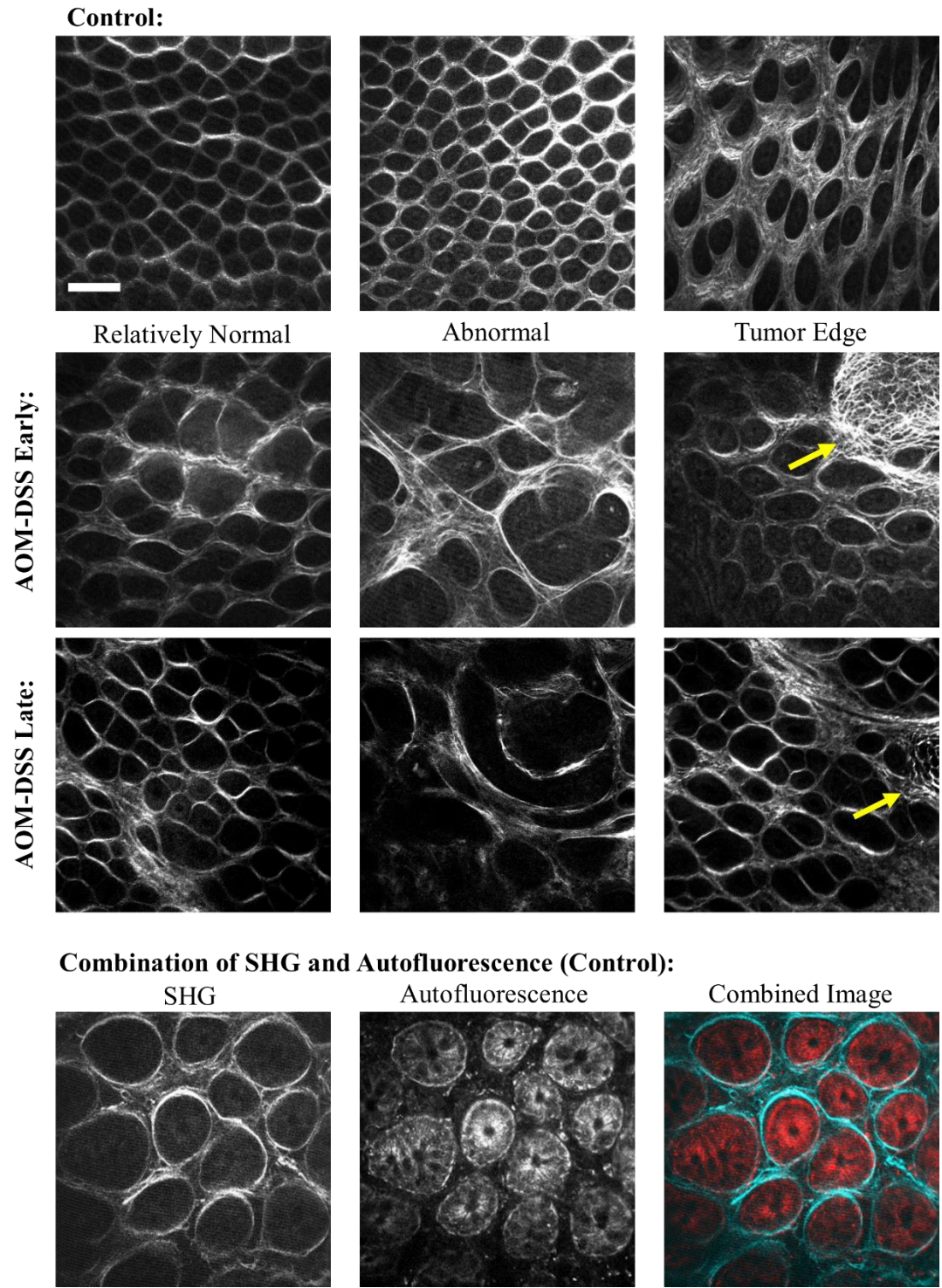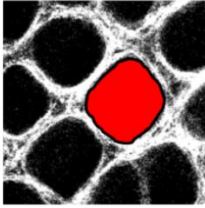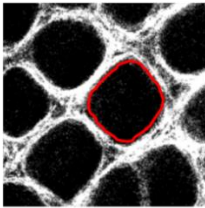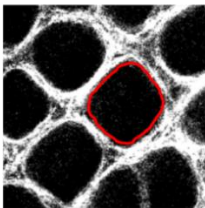
Figure S2. Example SHG images of Control, AOM-DSS early, and AOM-DSS late tissue; yellow arrows point to tumor edge. Also, example of the combination of SHG and autofluorescence imaging, using Control epithelium. Scale bar is 100 μm.

S3. Image segmentation and quantification of crypt structures

After the selection of the optimal thresholds, the images were binarized, and the objects in the binary image were then eroded and dilated (5 pixel diameter disk) to discard objects too small to be crypts as well as reduce rough edges stemming from image noise.
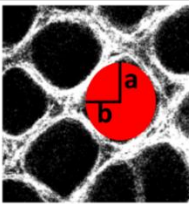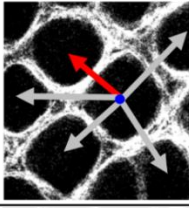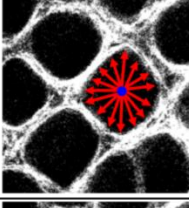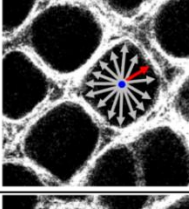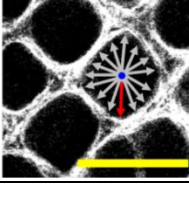
The segmented objects, or detected crypt structures, were then analyzed for quantification of the following image features: crypt area, circularity, eccentricity, perimeter, distance to the nearest neighbor (distance from each centroid to the closest centroid), and average of a centroid distance function (distance from the centroid to each boundary pixel). Previous work details specifics of automated crypt area and circularity quantification [2, 3]. For automated crypt area, circularity, and perimeter quantification (Fig. S3), the automated quantification of area (A) and perimeter (P), and therefore by default circularity variables, were converted into microns.

Figure S3. Summary of quantitative image features. Each image feature is described with an equation and a visual representation of the calculation using an SHG image of normal epithelium; scale bar is 100 μm.

Additional image features included: eccentricity, where a is half the length of the major axis and b is half the length of the minor axis, and distance to the nearest neighbor, which was calculated by measuring the Euclidean distance between the centroid of a crypt to the centroid of every other crypt in the image, and selecting the minima, where the (x_c, y_c) are the coordinates of the centroid and (x_a, y_{aa}) represents the coordinates of all other centroids (Fig. S4). The average centroid distance function was calculated by measuring the Euclidean distance between the centroid of a crypt to each of the boundary pixels, and taking an average of the distances per crypt, where (x_c, y_c) are the coordinates of the centroid and (x_b, y_b) are the coordinates of a boundary pixel, and n is the number of boundary pixels in the object (Fig. S4).

Image Feature/Equation	Visual
Eccentricity $$\sqrt{1 - \left(\frac{b}{a}\right)^2}$$	
Nearest Neighbor $$min\ of\ \sqrt{(x_c - x_a)^2 + (y_c - y_a)^2}$$	
Average Centroid Distance Function $$\frac{\sum_{b=1}^{n} \sqrt{(x_c - x_b)^2 + (y_c - y_b)^2}}{n}$$	
Minimum Centroid Distance Function $$min\ of\ \sqrt{(x_c - x_b)^2 + (y_c - y_b)^2}$$	
Maximum Centroid Distance Function $$max\ of\ \sqrt{(x_c - x_b)^2 + (y_c - y_b)^2}$$	

Figure S4. Summary of quantitative image features. Each image feature is described with an equation and a visual representation of the calculation using an SHG image of normal epithelium; scale bar is 100 μm.

S4. Additional results of image segmentation and quantification of crypt structures

A full set of the results of the one-way ANOVA comparison, including those not shown in the manuscript and those which are not statistically significant, are shown below. In general, for both individual images acquired at a fixed depth (20 μm) and image depth stacks, the mean and standard deviation of each image feature (Fig. S3 and S4) within each image were quantified using an adaptation of a previously developed algorithm [2, 3]. The standard deviation of the image features within each image was calculated in order to measure the heterogeneity of the crypt structures; for example, tumor-adjacent regions tend to have both abnormally large and abnormally small crypt structures. A global average across these values would yield a mean value similar to that derived from normal tissue, but the standard deviation of crypt areas within an image would report this variance in a more representative manner.

The results of image feature quantification were then compared across cohorts: AOM early time point, AOM late time point, AOM-DSS early time point, AOM-DSS late time point, and Control. Nested one-way ANOVA with Tukey's post-test was used to determine statistically significant differences between the cohorts (JMP Pro 13). For all images, total image acquisition time was approximately 1.5 seconds, with total optical power at the sample limited to prevent photo-damage. Individual images were acquired at 512 x 512 pixels at 14-bit depth, yielding a 522 μm x 522 μm (~0.27 mm2) field of view, at approximately 20 μm from the epithelial surface. Image depth stacks were acquired at consecutive depths from the epithelial surface, in 20 μm steps, from 20 μm to 100 μm below the epithelial surface.
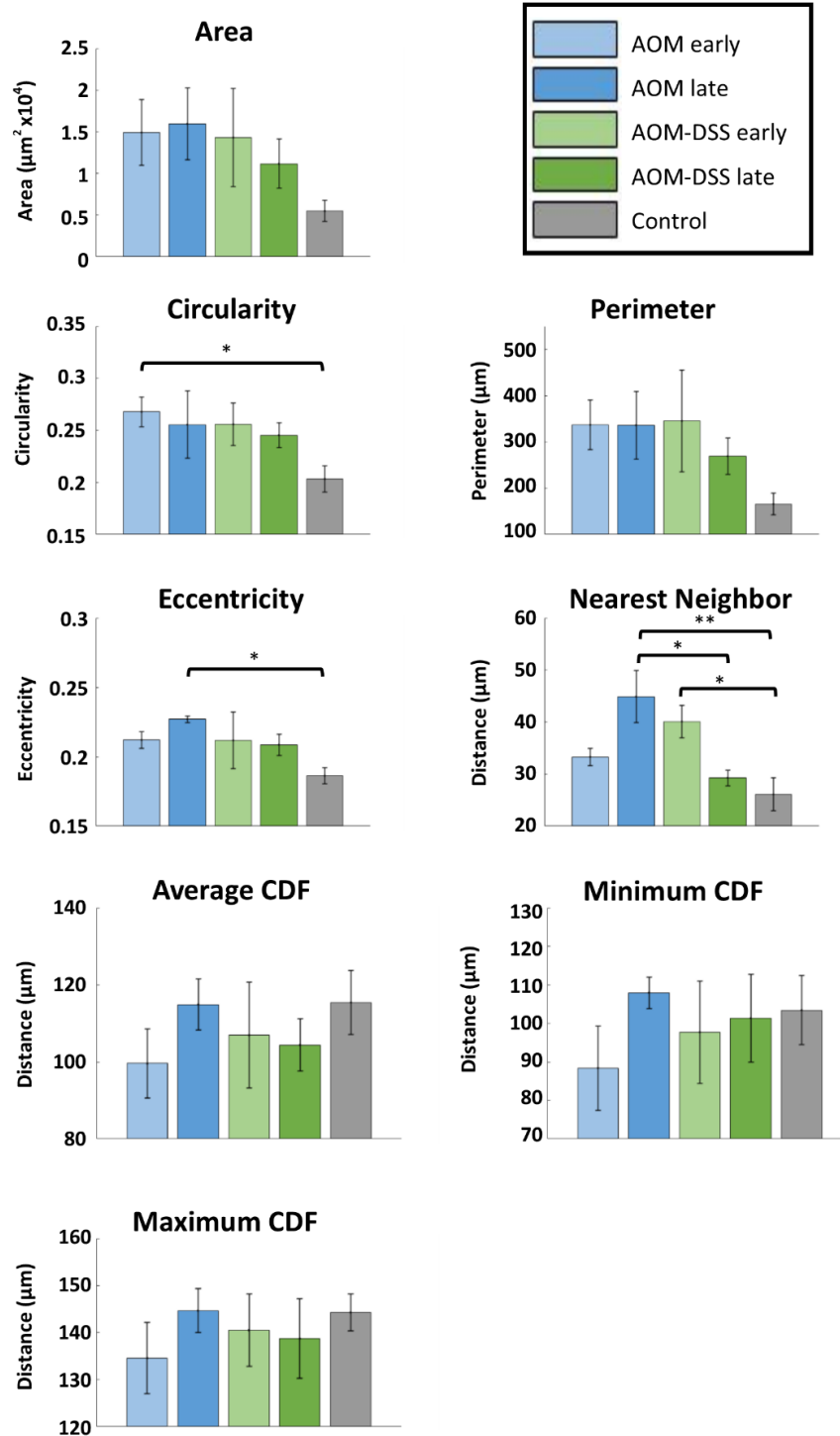
S5. Fixed image depth results (20 μm)

The comparison of the means (Fig. S5) and standard deviations (Fig. S6) for each of the image features discussed previously (Fig. S3 and S4) are shown: crypt area, nearest neighbor,

170

circularity, perimeter, crypt count, eccentricity, average centroid distance function, minimum centroid distance function, and maximum centroid distance function. For mean (Fig. S5), the two image features with statistical significance between cohorts were nearest neighbor and crypt count. For standard deviation (Fig. S6), the image features with statistical significance were nearest neighbor, circularity, and eccentricity. They all showed a difference between the Control cohort and one or more of the tumor-bearing cohorts, but this is not outside of what has been shown with confocal laser microendoscopy systems such as the Cellvizio® (which differentiated between colorectal lesions and adjacent normal colorectal epithelial crypt structure in a preliminary clinical trial) [5].

The differences of interest are in the distinction in mean (Fig. S5) of nearest neighbor between the AOM late and AOM-DSS early cohorts, as well as the AOM late and the AOM-DSS late cohorts. For standard deviation (Fig. S6), the difference of interest is also for nearest neighbor, between AOM late and AOM-DSS late cohorts. These results suggest that morphological biomarkers in SHG images of colorectal epithelium could be used to distinguish between spontaneous tumor development (AOM model) and colitis-associated tumor development (AOM-DSS model). While the alternative image features did not show statistical significance in our study, this does not conclusively rule them out as incapable of providing additional information about the morphological differences between cohorts. Further study into these or similar features could prove useful in development of clinical imaging systems and guides for interpreting the acquired images.
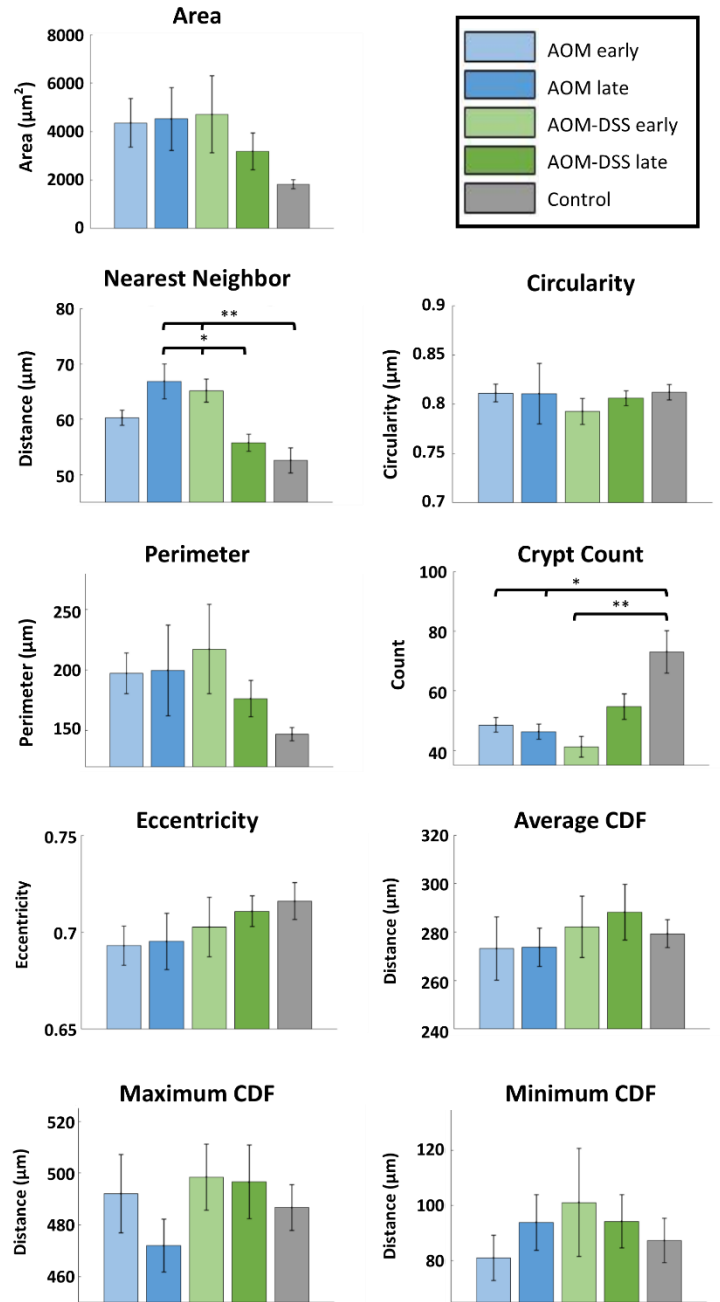
Figure S5. Mean values of various image features: crypt count, crypt area, crypt circularity, crypt eccentricity, nearest neighbor, average centroid distance function (CDF). Cohort n values (images): AOM early n=48, AOM late n=23, AOM-DSS early n=45, AOM-DSS late n=24, Control n=55. Error bars are standard error; significance was calculated via a nested one-way ANOVA with Tukey's HSD post-test. Significance was noted (*) for p values <0.05 and (**) for p values <0.01.

Figure S6. Standard deviation values of various image features: crypt count, crypt area, crypt circularity, crypt eccentricity, nearest neighbor, average centroid distance function (CDF). Cohort n values (images): AOM early n=48, AOM late n=23, AOM-DSS early n=45, AOM-DSS late n=24, Control n=55. CDF = centroid distance function. Error bars are standard error; significance was calculated via a nested one-way ANOVA with Tukey's HSD post-test. Significance was noted (*) for p values <0.05 and (**) for p values <0.01
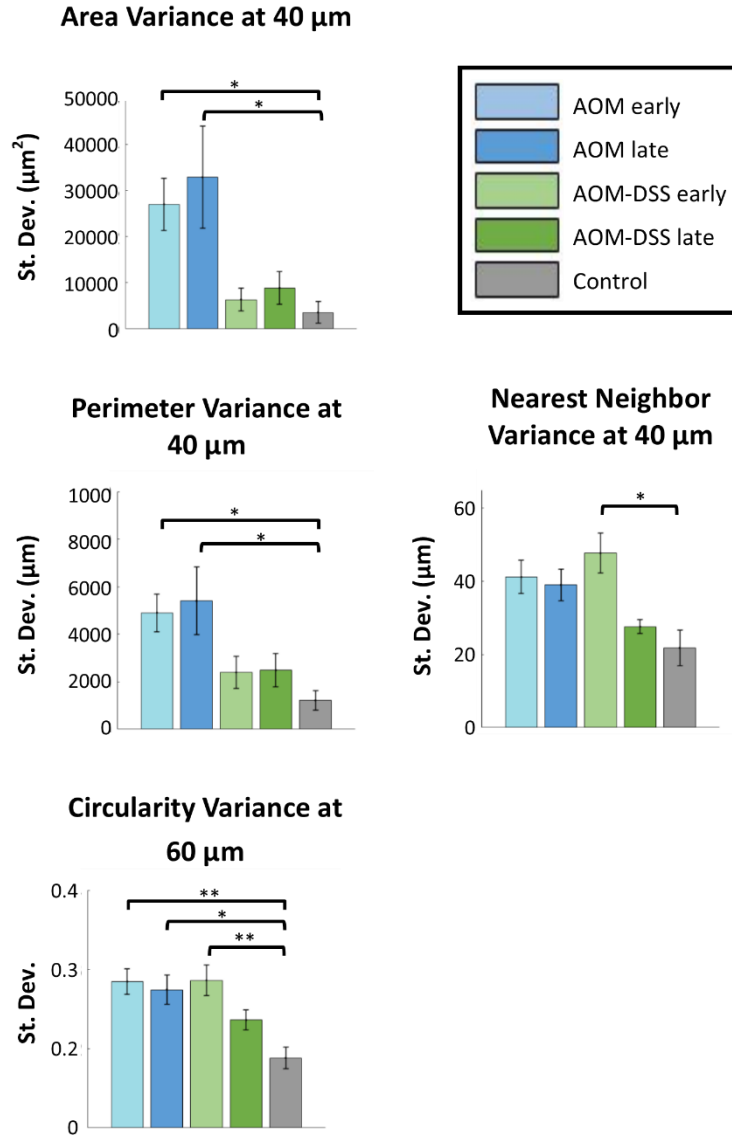
S6. Image depth stack results

The comparison of the means and standard deviations for each of the image features discussed previously (Fig. S3 and S4) were calculated across a fixed depth (20 to 100 μm) and compared across cohorts. The image stacks were also compared within cohorts (fixed groups) across varying acquisition depth for the means and standard deviation of each of the image features. Due to the extensive number of comparisons, as well as due to the majority not showing statistical significance, only the image features with at least one statistically significant difference between two cohorts are shown below. For comparison of means across cohorts (Fig. S7), the image feature with statistical significance between cohorts was nearest neighbor at 40 μm. To compare standard deviation values across cohorts (Fig. S8), the image features with statistical significance were area, perimeter, and nearest neighbor at 40 μm, and circularity at 60 μm. To compare mean values across acquisition depths there are no figures, as no image feature showed statistical significance between cohorts. For comparison of standard deviations across acquisition depths (Fig. S9), the image features with statistical significance were circularity within the AOM late cohort, and circularity and eccentricity within the Control cohort.

Several of the image features, including nearest neighbor, area, perimeter, circularity, and eccentricity showed a difference between the Control cohort and one or more of the tumor-bearing cohorts. While these results corroborate that there are morphological differences between regions of dysplasia and healthy epithelium, they do not show clear usefulness in distinguishing between spontaneous tumor development (AOM model) and colitis-associated tumor development (AOM-DSS model). Though this does not prove them incapable of providing additional information about the morphological differences between cohorts, further study into

174

depth section and/or volumetric analysis of crypt morphology is needed to better understand any

differences between spontaneous and colitis-associated tumor development.
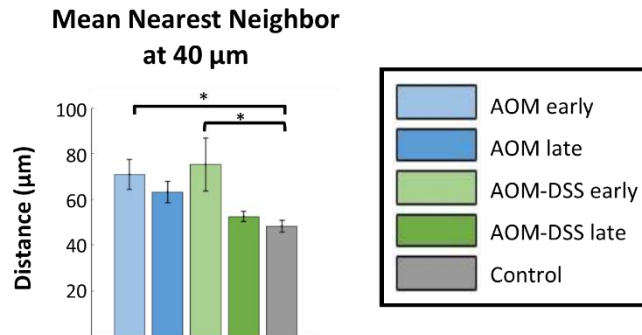
Figure S7. Mean values of crypt nearest neighbor at 40 μm of acquisition depth across cohorts. Cohort n values (stacks): AOM early n=8, AOM late n=9, AOM-DSS early n=5, AOM-DSS late n=12, Control n=9. Significance was calculated via two-way ANOVA with Tukey's post-test. Error bars are standard error Significance was noted (*) for p values <0.05 and (**) for p values <0.01.

Area Variance at 40 μm

Perimeter Variance at 40 μm

Nearest Neighbor Variance at 40 μm

Circularity Variance at 60 μm

Figure S8. Standard deviation values of area, perimeter, and nearest neighbor at 40 μm of acquisition depth across cohorts, and of circularity at 60 μm of acquisition depth across cohorts. Cohort n values (stacks): AOM early n=8, AOM late n=9, AOM-DSS early n=5, AOM-DSS late n=12, Control n=9. Significance was calculated via two-way ANOVA with Tukey's post-test. Error bars are standard error Significance was noted (*) for p values <0.05 and (**) for p values <0.01.

176
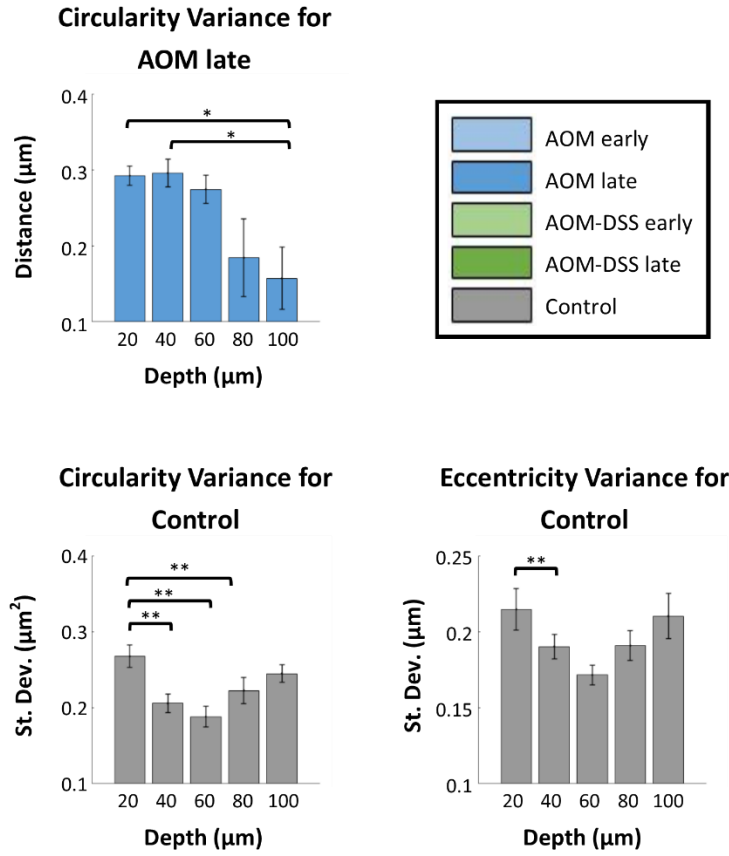
Figure S9. Standard deviation values of crypt circularity of AOM late cohort across acquisition depths, and of crypt circularity and eccentricity of Control cohort across acquisition depth. Cohort n values (stacks): AOM late n=9, Control n=9. Significance was calculated via two-way ANOVA with Tukey's post-test. Error bars are standard error Significance was noted (*) for p values <0.05 and (**) for p values <0.01.

References

[1] S. P. Prieto, C. L. Reed, H. M. James, K. P. Quinn and T. J. Muldoon, "Differences in colonic crypt morphology of spontaneous and colitis-associated murine models via second harmonic generation imaging to quantify colon cancer development," *Manuscript Submitted for Publication. BMC Cancer,* 2018.

[2] S. P. Prieto, K. K. Lai, J. A. Laryea, J. S. Mizell and T. J. Muldoon, "Quantitative analysis of ex vivo colorectal epithelium using an automated feature extraction algorithm for microendoscopy image data," *Journal of Medical Imaging,* vol. 3, *(2),* pp. 024502, 2016.

[3] S. P. Prieto, K. K. Lai, J. A. Laryea, J. S. Mizell, W. C. Mustain and T. J. Muldoon, "Fluorescein as a topical fluorescent contrast agent for quantitative microendoscopic inspection of colorectal epithelium," *Biomedical Optics Express,* vol. 8, *(4),* pp. 2324-2338, 2017.

[4] D. R. Rivera, C. M. Brown, D. G. Ouzounov, I. Pavlova, D. Kobat, W. W. Webb and C. Xu, "Compact and flexible raster scanning multiphoton endoscope capable of imaging unstained tissue," *Proc. Natl. Acad. Sci. U. S. A.,* vol. 108, *(43),* pp. 17598-17603, Oct 25, 2011.

[5] G. D. De Palma, S. Staibano, S. Siciliano, F. Maione, M. Siano, D. Esposito and G. Persico, "In-vivo characterization of DALM in ulcerative colitis with high-resolution probe-based confocal laser endomicroscopy," *World J. Gastroenterol.,* vol. 17, *(5),* pp. 677-680, Feb 7, 2011.